

**Thermal transport at the nanoscale: from Fourier  
diffusion to phonon hydrodynamics**

by

Samuel Cole Huberman

Submitted to the Department of Mechanical Engineering  
in partial fulfillment of the requirements for the degree of

Doctor of Philosophy

at the

MASSACHUSETTS INSTITUTE OF TECHNOLOGY

September 2018

© Massachusetts Institute of Technology 2018. All rights reserved.

Author .....  
Department of Mechanical Engineering  
August 10, 2018

Certified by .....  
Gang Chen  
Carl Richard Soderberg Professor of Power Engineering  
Thesis Supervisor

Accepted by .....  
Rohan Abeyaratne  
Quentin Berg Professor of Mechanics  
Chairman, Department Committee on Graduate Theses



# Thermal transport at the nanoscale: from Fourier diffusion to phonon hydrodynamics

by

Samuel Cole Huberman

Submitted to the Department of Mechanical Engineering  
on August 10, 2018, in partial fulfillment of the  
requirements for the degree of  
Doctor of Philosophy

## Abstract

From the global pursuit of clean and efficient sources of energy to the challenges presented by the high power densities in the semiconductor industry to the problem of decoherence in quantum systems, thermal processes are ubiquitous across all scales of space and time. Work done in the last decade has led to a number of experimental and theoretical developments that have enabled scientists and engineers to construct an accurate picture of thermal transport at small length and time scales. In this work, we employ and contribute to this modern toolset by testing and pushing the limits of our understanding. First, we experimentally examine the effects of domain walls and crystal structure in ferroelectric thin films on thermal transport. We move on to study the effect of crystal structure and defects in oxide thin films, in which we demonstrate a reversible process that can tune thermal conductivity across one order of magnitude. Secondly, we experimentally and theoretically examine deviations from the diffusive regime of thermal transport in SiGe alloys, thereby extending current theory and experiment to the study of size effects in thermal transport to opaque materials. Finally, we go beyond the single mode approximation to the Boltzmann transport equation and develop a formalism to study size effects and hydrodynamic phenomena by solving the full scattering matrix version of the linearized Boltzmann transport equation. Using this formalism as a guide, we report the experimental observation of second sound in graphite.

Thesis Supervisor: Gang Chen  
Title: Carl Richard Soderberg Professor of Power Engineering



## Acknowledgments

I thank my advisor, Gang Chen, for his support and guidance. I thank my committee members, Keith Nelson and Seth Lloyd, for taking the time to share their knowledge and stories. I thank my colleagues Vazrik Chiloyan, Lingping Zeng, Ryan Duncan, Alex Maznev, Shuai Ning and Qiyang Lu. It was a real pleasure working with you. I thank Caroline Ross and Bilge Yildiz for the opportunity to study the thermal properties of some interesting materials. I thank the members of the Nanoengineering group for always taking the time to help answer my questions.

Finally, I thank my Caro and my Bertie. This work would have gone unfinished without you.

It's always seemed a little preposterous that Hamlet, for all his paralyzing doubt about everything, never once doubts the reality of the ghost. Never.

*Infinite Jest, David Foster Wallace*

# Contents

<b>1</b>	<b>Introduction</b>	<b>21</b>
1.1	Organization of Thesis . . . . .	23
<b>2</b>	<b>Theoretical Foundations and Experimental Techniques</b>	<b>27</b>
2.1	Theory . . . . .	27
2.1.1	From the phonon Hamiltonian to the phonon Boltzmann Transport Equation . . . . .	28
2.1.2	Extension to real crystals . . . . .	37
2.1.3	Application of BTE to nanoscale thermal transport . . . . .	41
2.1.4	Some remarks concerning the origin of thermal resistance . . . . .	43
2.1.5	Numerical techniques for solving the BTE . . . . .	49
2.2	Experimental Techniques . . . . .	51
2.2.1	Time-domain thermoreflectance . . . . .	51
2.2.2	Transient thermal grating . . . . .	54
<b>3</b>	<b>Tuning thermal conductivity</b>	<b>59</b>
3.1	Introduction . . . . .	59
3.2	BFO . . . . .	60
3.2.1	Thermal conductivity characterization . . . . .	62
3.2.2	Summary . . . . .	70
3.3	SCO . . . . .	71
3.3.1	Sample information . . . . .	72
3.3.2	Thermal conductivity characterization . . . . .	75

3.3.3	Summary . . . . .	84
3.4	Future work . . . . .	84
<b>4</b>	<b>Size effects in SiGe alloys</b>	<b>87</b>
4.1	Introduction . . . . .	87
4.2	Theory . . . . .	89
4.2.1	First Principle Calculations . . . . .	89
4.2.2	Solving the Boltzmann Transport Equation . . . . .	91
4.3	Experiment . . . . .	102
4.3.1	Sample specifications . . . . .	102
4.3.2	Results . . . . .	102
4.4	Discussion and Outlook . . . . .	102
4.5	Conclusion . . . . .	106
<b>5</b>	<b>The Full Scattering Matrix BTE and Phonon Hydrodynamics</b>	<b>107</b>
5.1	Introduction . . . . .	107
5.2	Theory . . . . .	109
5.3	Numerical studies . . . . .	111
5.3.1	Steady state TG . . . . .	111
5.3.2	Hydrodynamic regime . . . . .	114
5.4	Experiments . . . . .	126
5.4.1	Graphite . . . . .	126
5.4.2	Conclusion . . . . .	130
<b>6</b>	<b>Conclusions and outlook</b>	<b>133</b>
<b>A</b>		<b>137</b>
A.1	TDTR reference data . . . . .	137
<b>B</b>		<b>139</b>
B.1	SiGe study supplementary material . . . . .	139

**C** **143**

C.1 Hydrodynamic study supplementary material . . . . .	143
---	-----



# List of Figures

1-1	Diagram of the organization of this thesis. . . . .	24
2-1	Evolution of the probability distribution of the momentum variables $p$ for a 1D anharmonic chain. The $\frac{1}{t} \ll \epsilon$ is an example of a stationary distribution. . . . .	30
2-2	Phonon dispersion for silicon obtained using force constants from DFT calculations. Frequency in THz. . . . .	39
2-3	An example of a 3-phonon scattering process in graphene (or any 2D material with the same lattice as graphene) that is considered to be a Normal process in the 2-atom BZ but an Umklapp process in the 4-atom BZ. . . . .	46
2-4	Debye dispersion with two branches. Arrows denote modes involved in a Normal process that reverses momentum. . . . .	47
2-5	Debye dispersion with three phonon modes where each arrow corresponds to a single mode. . . . .	48
2-6	Example of the random walk taken by a particle in VRMC as part of a simulation of phonon transport in silicon at room temperature. . . .	49
2-7	Mean square displacement as a function of time obtained from a VRMC simulation of a volumetric point heat source in bulk silicon at 300 K. . . . .	51
2-8	Diagram of the TDTR setup used in this work to perform the thermal conductivity measurements. Courtesy Kimberlee Collins. . . . .	52
2-9	Example (a) phase and (b) amplitude TDTR traces and fits of an aluminum-sapphire sample. . . . .	54

2-10 A diagram of the reflection mode TTG geometry. The pump and probe beams are passed through the diffraction grating (referred to here as the phase mask), the which sets the period length of the heating profile. The $\pm 1$ orders of the pump and probe are then imaged on the sample surface using the $4f$ lens system. An ND filter attenuates the reference beam of the probe, while an optic (the heterodyne phase control) is placed in the signal beam of the probe to control the relative phase between the reference and the signal. The diffracted signal and the reflected reference are collected at the detector. Reproduced from [1] with permission from the American Physical Society. . . . .	55
2-11 Example phase and amplitude grating traces taken from a $\text{Si}_{93.4}\text{Ge}_{6.6}$ sample. . . . .	58
3-1 Crystal structures for the (a) R-BFO and (b) T-BFO phases. . . . .	62
3-2 (a) Amplitude and (b) phase sensitivity for the TDTR BFO measurements. Here, $\text{BFO}_k$ corresponds to the BFO thermal conductivity, $G_1$ corresponds to the interface conductance between aluminum and BFO, $Cv_2$ corresponds volumetric heat capacity of BFO, $G_2$ corresponds to the interface conductance between BFO and STO and $\text{STO}_k$ corresponds to the STO substrate thermal conductivity. . . . .	63
3-3 Example error landscapes for (a) R-BFO and (b) T-BFO. The contours correspond to iso-error curves defined by taking the logarithm of the residual error between the fit and the experimental data. . . . .	64
3-4 Raw TDTR data (circle markers) and best fits (lines) to (a) phase and (b) amplitude representations for R-BFO (blue) and T-BFO (orange). . . . .	64
3-5 Vertical PFM phase images of (a) T-5, (b) T-100, (c) R-5, and (d) R-100. Reproduced from [2] with permission from the American Physical Society. . . . .	66
3-6 Schematic of the in-situ TDTR measurement. Reproduced from [2] with permission from the American Physical Society. . . . .	67

3-7	Example P-E loop for R and T-like BFO. Reproduced from [2] with permission from the American Physical Society. . . . .	68
3-8	Raw TDTR data taken during the in-situ measurement on (a) R-BFO and (b) T-BFO. . . . .	69
3-9	Possible ferroelectric domain configurations in BFO thin films. Adapted from [2] with permission from the American Physical Society. . . . .	69
3-10	(a) Schematic showing the ionic liquid gating of SrCoO <sub>2.5</sub> . (b) Schematic showing the overpotential distribution in the BM-SCO thin film sample before the hydrogenation reaction and the resulting proton concentration gradient. The overpotential decreases with increasing distance away from the contact due the ohmic loss from the resistance of SCO thin film. The dashed lines matches the position in the overpotential gradient with the positions in the optical picture of the sample. Hydrogenation caused a color change of SCO from brownish to light greyish. . . . .	73
3-11	(a) Atomic legend for the (b) H-SCO, (c) BM-SCO and (d) P-SCO crystal stuctures. . . . .	74
3-12	X-ray diffraction showing the BM-SCO (008) diffraction peak, hydrogenated SrCoO <sub>2.5</sub> (H-SCO) (008) peak after -4 V ionic liquid gating, and the oxygenated perovskite SrCoO <sub>3</sub> (P-SCO) after +3 V gating. The shoulder peak in H-SCO at higher $2\theta$ position is due to the non-switched BM-SCO regions of the sample under the silver electrode used.	75
3-13	Raw TDTR data (circle markers) and best fits (lines) to (a) phase and (b) amplitude representations for H-SCO (orange), BM-SCO (blue) and P-SCO (green). The H-SCO and P-SCO were obtained by gating BM-SCO through ionic liquid gating. . . . .	76

3-14 Sensitivity analysis for the SCO thin film TDTR measurements where $\text{SCO}_k$ corresponds to the SCO thermal conductivity, $G_1$ corresponds to the interface conductance between aluminum and SCO, $G_2$ corresponds to the interface conductance between SCO and YSZ and $\text{YSZ}_k$ corresponds to the YSZ substrate thermal conductivity. Subplots correspond to: (a) amplitude sensitivity at 6 MHz, (b) amplitude sensitivity at 12 MHz, (c) phase sensitivity at 6 MHz and (d) phase sensitivity at 12 MHz. . . . .	77
3-15 Error landscapes for the SCO thin film TDTR measurements. Subplots correspond to (a) BM-SCO, (b) H-SCO, (c) P-SCO and (d) a sapphire reference sample. . . . .	78
3-16 (a) Room temperature thermal conductivity of $\text{SrCoO}_x$ plotted as a function of applied electrical bias (anodic) at 300°C by using YSZ as a solid gating electrolyte. (b) XRD results on $\text{SrCoO}_x$ upon applying the electrochemical potentials shown in (a). The gradual transition from a mixture of BM-SCO and P-SCO phases to single P-SCO phase was observed. . . . .	81
3-17 The effect of $\text{H}^+$ concentration on the thermal transport property of SCO. (a) Co L <sub>2,3</sub> -edge XAS spectra fitted with linear combinations of spectra measured at spot 1 and 2. The symbols are measured data while the lines are the fitting. (b) Thermal conductivity (in red symbols) of ionic gel hydrogenated SCO measured along the $\text{H}^+$ concentration gradient. In the same plot, the relative $\text{H}^+$ concentrations deduced from the spectra fitting results in (a) were plotted in square symbols, referenced to the spectrum measured at spot 2. . . . .	83
4-1 $\text{Si}_{93.4}\text{Ge}_{6.6}$ MFP accumulation of thermal conductivity and heat capacity at 300 K. Reproduced from [1] with permission from the American Physical Society. . . . .	91

4-2	Kernels of the effective conductivity in Eq. 4.20. (a) The numerator kernel $f$ that shows the size effects and appears beside the differential conductivity and (b) the denominator kernel $g$ that shows the size effects and appears beside the spectral heat capacity. Reproduced from [1] with permission from the American Physical Society. . . . .	99
4-3	Effective thermal conductivity for $\text{Si}_{93.4}\text{Ge}_{6.6}$ in the one-dimensional limit and the surface heating limit. The effective thermal conductivity using the gray suppression function for one-dimensional TTG (Eq. 4.24) is also shown [3]. Reproduced from [1] with permission from the American Physical Society. . . . .	100
4-4	Temperature profiles obtained from Monte Carlo simulations compared with the corresponding variational predictions for $\text{Si}_{93.4}\text{Ge}_{6.6}$ at 300 K with a (a) grating period of 100 nm and optical penetration depth of 10 nm and a (b) grating period of 10 $\mu\text{m}$ and optical penetration depth of 1 $\mu\text{m}$ . The Monte Carlo trace for case (b) contains noise because of the computational cost of simulating longer decays for a large number of effective particles. Reproduced from [1] with permission from the American Physical Society. . . . .	101
4-5	(a) Raw experimental data for 6.6 $\mu\text{m}$ (top) and 1.8 $\mu\text{m}$ (bottom) grating periods with the fit obtained from Eq. 4.7. (b) Green circles correspond to measured TTG data for a range of grating periods, from 13.5 to 1 $\mu\text{m}$ . The black line is the prediction from the variational solution with DFT properties as input, while the orange line (yellow line, purple line) corresponds to the variational prediction for $\text{Si}_{97}\text{Ge}_3$ ( $\text{Si}_{80}\text{Ge}_{20}$ , Si). Reproduced from [1] with permission from the American Physical Society. . . . .	103

4-6 Comparison between the predictions from the variational approach to using the MFP accumulation function or the gray suppression function for one-dimensional TTG (Eq. 4.24) [3] to estimate the effective thermal conductivity at $1.00 \mu\text{m}$ grating period. Reproduced from [1] with permission from the American Physical Society. . . . .	105
5-1 Effective thermal conductivity of graphene at room temperature as a function of the grating period for the steady state thermal grating geometry. . . . .	113
5-2 Schematic of the hydrodynamic window for a crystalline solid. . . . .	116
5-3 Schematic depiction of (a) diffusive and (b) hydrodynamic transport of gas particles. . . . .	118
5-4 (a) Time-domain and (b) frequency-domain representation of the temperature response for isotopically-pure graphite at 100 K in the 1D-TTG geometry. . . . .	121
5-5 Hydrodynamic dispersion relations via grating period versus frequency ( $\omega$ ) plots for graphene (a) at 50 K with no isotopes, (b) at 50 K with isotopes, (c) at 100 K with isotopes and (d) at 300 K with isotopes. The intensity of corresponds to the ratio of the amplitude of $\delta T(\omega, q)$ to the amplitude of $\delta T(0, q)$ . . . . .	123
5-6 The hydrodynamic window of isotopic graphene. . . . .	124
5-7 Hydrodynamic dispersion relations via grating period versus frequency ( $\omega$ ) plots for graphite (a) at 50 K with no isotopes, (b) at 50 K with isotopes, (c) at 100 K with no isotopes and (d) at 100 K with isotopes. .	125
5-8 The hydrodynamic window of isotopic graphite. . . . .	126
5-9 (a) Out-of-plane XRD and (b) in-plane XRD on HOPG. . . . .	127
5-10 Theoretical predictions of the (a) absolute and (b) normalized effective thermal conductivity alongside TTG measurements of graphite at room temperature. . . . .	128

5-11 (a) Theoretical prediction of the temperature decay in graphite at 80 K as function of grating period in the 1D-TTG geometry. (b) Experimental TTG traces on HOPG at $\sim$ 85 K as a function of grating period. . . . .	129
5-12 (a) Theoretical prediction of the temperature decay in graphite as function of temperature in the 1D-TTG geometry for a $10.0 \mu\text{m}$ grating period. (b) Experimental TTG traces on HOPG for a $10.0 \mu\text{m}$ grating period at $\sim$ 85 K, at $\sim$ 104 K, at $\sim$ 124 K and at $\sim$ 144 K. . . . .	130
6-1 The unexplored region. . . . .	134
B-1 Effect of uncertainty in the optical penetration depth (1, 1.5 and $2 \mu\text{m}$ ) on the measurement of effective thermal conductivity with TTG. The error is larger for larger grating periods, as the transport transitions into the $q/\beta \ll 1$ regime. . . . .	139
B-2 Monte Carlo simulation of reflection TTG geometry for Si with grating period of $10 \mu\text{m}$ and optical penetration depth of $10 \text{ nm}$ . This example demonstrates the limitations of a modified Fourier treatment, independent of the variational framework. No theory based upon a Fourier model will capture this behavior because a time-dependent thermal conductivity is required to do so and the interpretation of such a quantity can only be phenomenologically understood. However, the variational approach can provide a quantitative measure of the extent of this failure. or instance, one could substitute the variational temperature decay back into the BTE (Eq. 15 in the main text) and calculate the difference between the left and right hand side of the equation as a proxy for the error. Another possible avenue is to test the performance of the ballistic solution for the geometry as the trial solution. . . . .	140

B-3 Raman spectra for Si and $\text{Si}_{93.4}\text{Ge}_{6.6}$ . A dominant peak is found at 520 $\text{cm}^{-1}$ for Si and at 513 $\text{cm}^{-1}$ for $\text{Si}_{93.4}\text{Ge}_{6.6}$ . As noted in the main text, the DFT-based virtual crystal approximation predicts a single peak at 488 $\text{cm}^{-1}$ for $\text{Si}_{93.4}\text{Ge}_{6.6}$ , but not is capable of capturing the peaks near 400 $\text{cm}^{-1}$ .	141
B-4 DFT comparison between averaging force constants, using the $(\text{Si},\text{Ge}).\text{pz-bhs.UPF}$ set of pseudopotentials (denoted by FC), and averaging pseudopotentials (denoted by PP) through the <code>virtual.x</code> program, using the $(\text{Si},\text{Ge}).\text{pz-n-nc.UPF}$ set of pseudopotentials. TC denotes the thermal conductivity accumulation function and HC denotes the heat capacity accumulation function.	142
C-1 Effect of probe power in low temperature graphite TTG measurements.	143
C-2 Effect of pump power in low temperature graphite TTG measurements.	144
C-3 Comparison between the detector response and a representative low temperature graphite TTG measurements.	144

# List of Tables

3.1	BFO samples . . . . .	62
3.2	Effect of film thickness on the thermal conductivity of BFO. . . . .	65
3.3	Effect of substrate on the thermal conductivity of BFO. . . . .	65
3.4	In-situ thermal conductivity of BFO as a function of applied electric field. . . . .	68
3.5	Thermal conductivity of H-SCO, BM-SCO and P-SCO. . . . .	79
3.6	WO <sub>3</sub> TDTR measurements . . . . .	85
A.1	Thermal properties at 300 K of materials that are used as inputs into the thermal model of the TDTR measurements. . . . .	137



# Chapter 1

## Introduction

Prometheus stole fire from the gods and the rest is history, so the myth goes. The storytellers certainly chose an appropriate symbol of knowledge and its pursuit, because somewhat paradoxically, the theory of heat has continued to challenge scientists. A quote attributed to Rudolf Peierls captures this reality: “It seems there is no problem in modern physics for which there are on record as many false starts, and as many theories which overlook some essential feature, as in the problem of the thermal conductivity of [electrically] non-conducting crystals.” And yet given its inseparable connection with every physical process, one would not be so foolish to believe that all of the important questions concerning heat have converged on answers. Remarkably, it is only within the last decade that tools with the power to rigorously challenge these textbook answers have become available.

The earliest studies of heat conduction begin with the phenomenological equation, known as Fourier’s Law

$$Q = -k\nabla T \tag{1.1}$$

where  $Q$  is the heat flux,  $T$  is the temperature and the constant of proportionality,  $k$ , is the thermal conductivity. As with other simple equations, much of the physics lies beneath. Fourier’s law is the steady state consequence of the heat diffusion equation

$$\frac{\partial T}{\partial t} = \alpha \nabla^2 T \quad (1.2)$$

where  $\alpha$  is the thermal diffusivity. While not known at the time of its original recording, this equation encodes the macroscopic observables that are statistically related to the Brownian motion of microscopic thermal energy carriers.

The modern reductionist approach led scientists to study the properties of these microscopic thermal energy carriers. This thrust involved the adoption of a quantum mechanical framework to describe the energy carriers as particles for metals where electrons carry charge and heat and quasiparticles for insulators where phonons carry heat.

As the picture at the microscale and macroscale became independently clearer, the unification remained challenging. A step was taken by Peierls, who applied the Boltzmann Transport Equation (BTE) to describe the transport of single particle phonon distribution functions [4]. This framework takes as input the phonon properties and outputs the bulk thermal conductivity, in essence, linking the microscopic and macroscopic pictures. Under some approximations, the BTE was shown to be capable of recovering the scaling of thermal conductivity as a function of temperature [5, 6].

With the successful demonstration of the phonon BTE's ability to recover Fourier's law, a natural next question was could the BTE be used to study deviations from the diffusive regime? Casimir provided one such answer for the case of two blackbody phonon emitters connected by a long narrow cylinder, in essence, an idealization of a nanowire connected between two heat baths of different temperatures. In neglecting intrinsic phonon-phonon scattering, Casimir found that the phonon mean free path was proportional to the radius of the cylinder [7].

Progress can be viewed as attempts to extend Casimir's result to other geometries, such as the cross-plane, where the temperature gradient is parallel to the finite film length, or thin-film, where the temperature gradient is perpendicular to the finite film length, geometries [8]. The inclusion of intrinsic phonon-phonon scattering in the BTE framework was first treated using the gray approximation, where a single

representative phonon mode is considered [8, 9], and then subsequently extended to use the Debye approximation, where a single linear branch of the phonon dispersion is considered [10, 11], and more recently, the relaxation time approximation, where the full dispersion is considered [12, 13].

In parallel, the computational tools for modeling the materials progressed from relying on empirical interatomic potentials and molecular dynamics [14, 15] to using force constants obtained from approximate solutions to the Schrodinger equation (i.e.: Density functional theory), thereby enabling the prediction of the bulk thermal conductivity of simple crystals like silicon without relying on fitting parameters [16, 17].

On the experimental side, optical pump-probe techniques such as the time-domain thermoreflectance (TDTR) technique [18] and the transient thermal grating (TTG) technique [19] have been used to thermally characterize bulk and thin film systems. When such experimental techniques are coupled with nanofabrication techniques [20] or the developments of the high energy coherent light sources [21], the controlled creation of nanometer length scales, and thereby nanometer sources of heat, can be achieved. Electrically-driven thermal characterization techniques, such as the  $3\omega$  technique [22], have been extended to study nanostructures such as nanowires [23] and carbon nanotubes [24].

This combination of theoretical, computational and experimental development has led scientists to revisit old questions. In particular, the possibility of observing a phonon hydrodynamic regime at higher temperatures than what was previously known has received intense attention [25, 26]. While there are theoretical predictions of phonon hydrodynamics in materials like graphene and graphite, no experimental confirmation at the time of this writing exists.

## 1.1 Organization of Thesis

The objective of this thesis is to contribute to this modern task of improving the methodology that is used to study thermal transport. This is accomplished using a

combination of theory and experiment, in the investigation of three distinct transport regimes: the diffusive, the nondiffusive and the hydrodynamic regimes.

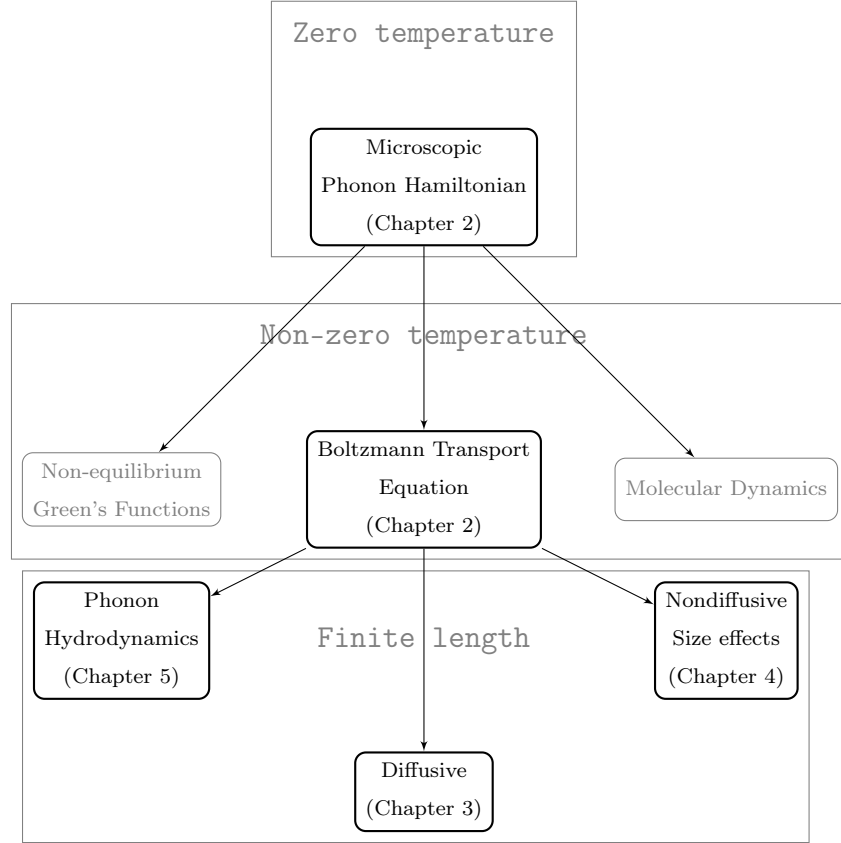


Figure 1-1: Diagram of the organization of this thesis.

The organization of the thesis is as follows. In Chapter 2, we will present the theoretical background upon which this work is built. The numerical tools and experimental techniques used in this work will be reviewed. In Chapter 3, under the diffusive picture, an experimental investigation into the effects of crystal structure, ferroelectric domain density and ionic insertion on thermal conductivity of thin films is carried out. We find that while the effect of ferroelectric domains is small to negligible, the combination of crystal phase transformations and varying ionic species produces a reversible and tunable one order of magnitude change in thermal conductivity. In Chapter 4, first principle calculations are used as input into a variational technique for solving the BTE to obtain predictions of the length-dependent effec-

tive thermal conductivity in a SiGe alloy. These predictions are then experimentally verified using reflection-mode transient thermal grating, where agreement between theory and experiment is found. In Chapter 5, the BTE is extended to study size effects in materials where the relaxation time approximation fails. In doing so, the framework is found to be capable of capturing what was previously considered to be exotic phenomena: hydrodynamic thermal transport. Using this theory, experimental confirmation of phonon hydrodynamics in graphite is reported. A discussion of future work is summarized in Chapter 6.



# Chapter 2

## Theoretical Foundations and Experimental Techniques

### 2.1 Theory

The connection between the Hamiltonian picture of anharmonic lattices and the Boltzmann Transport equation is presented. First, the harmonic description of phonons and the role of anharmonicity is reviewed. The Wigner-Weyl transformation is presented in combination with the necessary approximations to derive the BTE. The connection to real crystals is made and the quantities that are calculated from first principles are presented. A brief review of a numerical technique used to simulating the BTE is offered.

Before we present the mathematical details, some comments about the characteristics of the regime in which we will operate within. First, we assume that a quasiparticle description is valid. For this to be the case:  $\tau \gg \hbar/k_B T$  [27], where  $\tau$  is the quasi-particle lifetime. We further restrict ourselves to the case where the renormalization of the quasiparticle dispersion can be neglected. This is valid if our materials are not “strongly” anharmonic<sup>1</sup>. If the reader is familiar with derivations of the BTE or would prefer a more general picture, the following section may be overlooked and revisited at a later reading.

---

<sup>1</sup>This is not the case for materials like SrTiO<sub>3</sub> [28].

### 2.1.1 From the phonon Hamiltonian to the phonon Boltzmann Transport Equation

Peierls' original work invoked Fermi's golden rule to arrive at the phonon BTE [4] as do the standard references [29, 30]. Instead, we will present a single mathematical framework to obtain the BTE directly from the dynamics of a weakly anharmonic chain. To do so, we closely follow the presentation of Spohn [31]. To begin, a lattice is defined as a set of points in  $\mathbb{Z}^d$ , where  $d$  is the dimension. We can write our phonon Hamiltonian  $H$  as a sum of a harmonic and anharmonic terms over the lattice:

$$H = H_0 + V \quad (2.1)$$

where  $H_0$  corresponds to a Hamiltonian for a lattice of point masses connected by linear springs

$$H_0 = \frac{1}{2} \sum_{i \in \mathbb{Z}^3} p_i^2 + \frac{1}{2} \sum_{i,j \in \mathbb{Z}^3} \alpha(x_i - x_j) q_i q_j \quad (2.2)$$

where  $\alpha$  denotes the linear spring constant between lattice points  $i$  and  $j$  and  $q$  and  $p$  are the position (defined as displacement from the equilibrium lattice site) and momentum variables respectively. The anharmonic contribution to  $H$  has the general form of

$$V_{anh} = \sum_{i,j,k \in \mathbb{Z}^3} V_3(q_i, q_j, q_k) + \sum_{i,j,\dots,n \in \mathbb{Z}^3} V_n(q_i, q_j, \dots, q_n) \quad (2.3)$$

where  $V_3$  is the third-order potential term and  $V_n$  is the  $n$ th-order potential term. There exists only a handful of functional forms for  $V_{anh}$  that render  $H$  exactly integrable (i.e.: the equations of motions can be analytically obtained) [32]. For non-integrable Hamiltonians, perturbation theory based on the single particle functions is the typical resort. It is sufficient to consider a Hamiltonian of the form

$$H = \frac{1}{2} \sum_{i \in \mathbb{Z}^3} (p_i^2 + \omega_0^2 q_i^2) + \frac{1}{2} \sum_{i,j \in \mathbb{Z}^3} \alpha(x_i - x_j) q_i q_j + \lambda \sum_{i \in \mathbb{Z}^3} q_i^3 \quad (2.4)$$

where there is now an onsite interaction term,  $\omega_0^2 q_i^2$ , to illustrate the perturbative approach<sup>2</sup>.  $\lambda$  is the strength of the anharmonic term. We use the following Fourier transform convention

$$\tilde{f} = \sum_{x \in \mathbb{Z}^3} e^{-2\pi i k \cdot x} f. \quad (2.5)$$

Using the Hamiltonian defined in Eq. 2.4, the usual equations of motions of the Fourier-transformed  $p_i, q_i$  are

$$\frac{\partial}{\partial t} \tilde{q}_k(t) = \tilde{p}_k(t) \quad (2.6)$$

and

$$\frac{\partial}{\partial t} \tilde{p}_k(t) = -\omega_k^2 \tilde{q}_k(t) - \lambda \int dk_1 dk_2 \delta(k - k_1 - k_2) \tilde{q}_{k_1}(t) \tilde{q}_{k_2}(t). \quad (2.7)$$

At this point, one can choose to numerically integrate Eqs. 2.6 and 2.7 and study systems from a molecular dynamics perspective. Alternatively, one can push on and investigate the dynamics under certain assumptions. First, let  $a_k$  be a field operator defined by<sup>3</sup>

$$a_k = \frac{1}{2} \left( \sqrt{\omega_k} \tilde{q}_k + i \frac{1}{\sqrt{\omega_k}} \tilde{p}_k \right). \quad (2.8)$$

The position variable can be written in terms of  $a_k$  as follows

$$\tilde{q}_k = \frac{1}{\sqrt{2\omega_k}} (a_k + a_{-k}^*) \quad (2.9)$$

and, likewise, the momentum variable

$$\tilde{p}_k = \frac{i\sqrt{\omega_k}}{\sqrt{2}} (-a_k + a_{-k}^*) \quad (2.10)$$

---

<sup>2</sup>Systems without onsite interaction have unfortunately been referred to as momentum-conserving [33, 34]. The absence or presence of an onsite term is intimately tied to question of which systems thermalize.

<sup>3</sup>In the quantum derivation, the field operators become the creation and annihilation operators acting on a Fock space.

where  $*$  denotes the complex conjugate. Plugging Eqs. 2.9 and 2.10 and setting  $\lambda = 0$ , we recover the solution for the harmonic system:

$$a_k = Ae^{-i\omega_k t}. \quad (2.11)$$

The time-dependence of  $a_k$  is subsequently taken to be implicit unless otherwise noted. In the anharmonic system where  $\lambda \neq 0$ :

$$\frac{\partial}{\partial t} a_k = -i\omega_k a_k - i\lambda \int dk_1 dk_2 \delta(k - k_1 - k_2) (8\omega_k \omega_{k_1} \omega_{k_2})^{-\frac{1}{2}} (a_{k_1} + a_{-k_1}^*) (a_{k_2} + a_{-k_2}^*). \quad (2.12)$$

At this point, we will assume that  $a_k$  is a complex random variable with a well-defined probability measure, where  $\langle \dots \rangle$  denotes ensemble average over this probability measure. This probability measure is not known *a priori*, and Spohn argues that Gaussian measures are the most obvious choice. To see why this is a reasonable ansatz, consider an arbitrary distribution of initial values of momenta<sup>4</sup>. As time evolves, this distribution will flow to a stationary distribution, which for the Hamiltonians considered here, is a Gaussian distribution. This behavior is shown in Figure 2-1 and further evidence can be found in [35, 36].

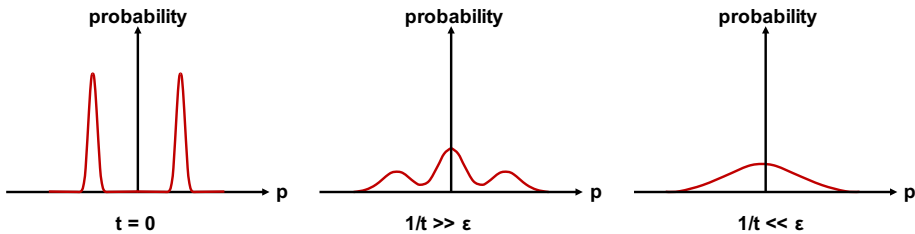


Figure 2-1: Evolution of the probability distribution of the momentum variables  $p$  for a 1D anharmonic chain. The  $\frac{1}{t} \ll \epsilon$  is an example of a stationary distribution.

From this statistical perspective, the quantities of interest are not only  $a_k$  but also the correlations between the random operators,  $\langle a_{k,1} a_{k,2} \dots a_{k,n} \rangle$ . This leads us to a series of statistical statements. The first is that of stationarity (or equivalently,

---

<sup>4</sup>The same principle applies to  $a_k$ .

translational invariance) in space

$$\begin{aligned} \langle q_i q_j \rangle^\epsilon &= Q(x_i - y_j) \\ \langle p_i p_j \rangle^\epsilon &= P(x_i - y_j) \\ \langle q_i p_j \rangle^\epsilon &= C(x_i - y_j) \end{aligned} \tag{2.13}$$

where  $\langle \dots \rangle^\epsilon$  denotes a local Gaussian average over the region of size  $\epsilon^{-1}$  and stationarity in time (or equivalently, conservation of energy)

$$\begin{aligned} \langle q_i(t') q_j(t) \rangle^\epsilon &= Q(t' - t) \\ \langle p_i(t') p_j(t) \rangle^\epsilon &= P(t' - t) \\ \langle q_i(t') p_j(t) \rangle^\epsilon &= C(t' - t) \end{aligned} \tag{2.14}$$

where  $Q, P, C$  are placeholder functions that only depend on the differences in space and time and not absolute points. In the  $a$ -field representation the assumption of space-time stationarity is summarily expressed as

$$\begin{aligned} \langle a_k \rangle^\epsilon &= 0 \\ \langle a_k a_{k'} \rangle^\epsilon &= 0. \end{aligned} \tag{2.15}$$

To understand the missing statistical definition of  $\langle a_k^* a_{k'} \rangle^\epsilon$ , it is worth first recalling the definition of the Wigner function

$$W^\epsilon(x, k) = \int_{\mathbb{R}^3} d\eta e^{i2\pi x \cdot \eta} \tilde{\psi}^*(k - \epsilon\eta/2) \tilde{\psi}(k + \epsilon\eta/2) \tag{2.16}$$

where  $\tilde{\psi}$  is the Fourier transform of a quantum wavefunction and  $\epsilon$  is the semiclassical parameter<sup>5</sup>, where  $\epsilon \rightarrow 0$  recovers the classical limit. This is a transformation that brings functions defined on a Hilbert space,  $\tilde{\psi}$ , to functions defined on a phase space,

---

<sup>5</sup>This is clearly the case if  $\epsilon = \hbar$ .

$W^\epsilon(x, k)$ . The relationship with  $W_k$  can be seen if  $\epsilon$  is used to coarse grain the lattice where  $x = \epsilon^{-1}y$

$$W^\epsilon(y, k) = \frac{\epsilon^3}{2} \int d\eta e^{i2\pi y \cdot \eta} \langle a^*(k - \epsilon\eta/2) a(k + \epsilon\eta/2) \rangle^\epsilon. \quad (2.17)$$

Thus,  $W^\epsilon(y, k)$  is naturally referred to as the one-point Wigner function. It is assumed that the distributions that are sufficiently separated in space,  $1 \ll l \ll \epsilon^{-1}$ , are independent. In the case of the anharmonic chain, this condition states that if one were to examine two or more distinct local subsets (as part of this assumption, the existence of these subsets is taken for granted) of the degrees of freedom, independent distributions over the canonical observables defined on these subsets would be obtained. Given the explicit dependence on the spatial coordinate, the Wigner function can capture spatial variations. Eventually, this will indeed be necessary to capture the spatial dependence of macroscopic observables, like temperature. 2-point Wigner functions have the form

$$\begin{aligned} W^\epsilon(y_1, k_1, y_2, k_2) &= \frac{\epsilon^6}{2} \int d\eta_1 d\eta_2 e^{i2\pi(y_1 \cdot \eta_1 + y_2 \cdot \eta_2)} \\ &\quad \langle a(k_1 - \epsilon\eta_1/2) a^*(k_1 + \epsilon\eta_1/2) a(k_2 - \epsilon\eta_2/2) a^*(k_2 + \epsilon\eta_2/2) \rangle^\epsilon. \end{aligned} \quad (2.18)$$

Taking  $\lim_{\epsilon \rightarrow 0}$  recovers what is referred to as the kinetic limit<sup>6</sup>

$$\lim_{\epsilon \rightarrow 0} W^\epsilon(y_1, k_1, \dots, y_n, k_n) = \prod_i^n W(y_i, k_i). \quad (2.19)$$

Before continuing, let's examine the kinetic limit of  $H_0$ . The equation of motion of the Wigner function is

---

<sup>6</sup>The guaranteed existence of this limit remains an open question. See [37] for a detailed discussion. Spohn argues that if  $a_k$  obeys Gaussian statistics, then the limit exists [31]. There is evidence that the chaotic nature of dynamics of the lattice underlies the Gaussian statistics of the canonical variables [38].

$$\begin{aligned} \frac{\partial}{\partial t} & \langle a^*(k - \epsilon\eta/2) a(k + \epsilon\eta/2) \rangle^{t/\epsilon} = \\ & -i\epsilon^{-1}(\omega_{k+\epsilon\eta/2} - \omega_{k-\epsilon\eta/2}) \langle a^*(k - \epsilon\eta/2) a(k + \epsilon\eta/2) \rangle^{t/\epsilon} \end{aligned} \quad (2.20)$$

where  $\langle \dots \rangle^{t/\epsilon}$  denotes the time-evolved measure at  $t/\epsilon$ . Taking  $\epsilon \rightarrow 0$  and Fourier transforming from  $\eta \rightarrow r$

$$\frac{\partial}{\partial t} W(r, k, t) = -\frac{1}{2\pi} \nabla \omega_k \cdot \nabla_r W(r, k, t) \quad (2.21)$$

which is the free-streaming Boltzmann transport equation where the collision operator has been set to zero. It shouldn't come as a surprise that  $W(r, k, t)$  is indeed the phonon counting function. With these statistical constraints in mind, we return to Eq. 2.12. Assuming a Gaussian distribution at initial  $t = 0$  and denoting  $\langle \dots \rangle_t$  as the time-evolved measure at  $t$  and working through  $\frac{\partial}{\partial t} a_p^* a_q$ , we can show that equation of motion of the 2-point correlation function will have the form<sup>7</sup>

$$\frac{\partial}{\partial t} \langle a_p^* a_q \rangle_t = i(\omega_p - \omega_q) \langle a_p^* a_q \rangle_t + \sqrt{\epsilon} F(q, p, t) \quad (2.22)$$

where we have rescaled  $\lambda \rightarrow \sqrt{\epsilon}\lambda$  and

$$\begin{aligned} F(q, p, t) &= i \sum_{\sigma_1, \sigma_2 = \pm 1} \int_{\mathbb{T}^6} dk_1 dk_2 \\ & \left( \phi(p, k_1, k_2) \delta(-p + \sigma_1 k_1 + \sigma_1 k_2) \langle a_{k_1, \sigma_1} a_{k_2, \sigma_2} a_q \rangle_t \right. \\ & \left. - \phi(q, k_1, k_2) \delta(q + \sigma_1 k_1 + \sigma_1 k_2) \langle a_p^* a_{k_1, \sigma_1} a_{k_2, \sigma_2} \rangle_t \right) \end{aligned} \quad (2.23)$$

where

$$\phi(k, k_1, k_2) = \lambda (8\omega_k \omega_{k_1} \omega_{k_2})^{-\frac{1}{2}}. \quad (2.24)$$

---

<sup>7</sup>This form is a classical analogue of the equation of motion of a Green's function [39, 40].

Since the terms with an odd number of moments vanish by the symmetry of Gaussian statistics, we must express our non-linear term as an integral in time to account for correlations between modes  $q$  and  $p$  at all previous times  $s$  that give rise to correlations at time  $t$  and rewrite our kinetic equation as

$$\frac{\partial}{\partial t} \langle a_p^*(t) a_q(t) \rangle_t = i(\omega_p - \omega_q) \langle a_p^*(t) a_q(t) \rangle_t + \epsilon \int_0^t ds G(p, q, t-s, s) \quad (2.25)$$

where

$$\begin{aligned} G(p, q, t, s) = & \sum_{\sigma_1, \sigma_2 = \pm 1} \int_{\mathbb{T}^6} dk_1 dk_2 \sum_{\tau_1, \tau_2 = \pm 1} \int_{\mathbb{T}^6} dl_1 dl_2 \phi(p, k_1, k_2) \phi(q, l_1, l_2) \\ & (\delta(-p + \sigma_1 k_1 + \sigma_1 k_2) \delta(q + \tau_1 l_1 + \tau_2 l_2) e^{-it\omega_q} \\ & + \delta(q + \sigma_1 k_1 + \sigma_1 k_2) \delta(-p + \tau_1 l_1 + \tau_2 l_2) e^{it(\sigma_1 \omega_{k_1} + \sigma_2 \omega_{k_2})} \langle a_{k_1, \sigma_1} a_{k_2, \sigma_2} a_{l_1, \tau_1} a_{l_2, \tau_1} \rangle_s) \\ & - 2 \sum_{\sigma_1, \sigma_2 = \pm 1} \int_{\mathbb{T}^6} dk_1 dk_2 \sum_{\tau_1, \tau_2 = \pm 1} \int_{\mathbb{T}^6} dl_1 dl_2 \phi(k_1, l_1, l_2) \delta(\sigma_1 k_1 + \tau_1 l_1 + \tau_2 l_2) e^{-it\omega_q} \\ & + \delta(q + \sigma_1 k_1 + \sigma_1 k_2) \sigma_1 (\phi(p, k_1, k_2) \delta(-p + \sigma_1 k_1 + \sigma_1 k_2) e^{-it\omega_q} \langle a_q a_{k_2, \sigma_2} a_{l_1, \tau_1} a_{l_2, \tau_1} \rangle_s \\ & - (q, k_1, k_2) \delta(q + \sigma_1 k_1 + \sigma_1 k_2) e^{-it\omega_p} \langle a_p^* a_{k_2, \sigma_2} a_{l_1, \tau_1} a_{l_2, \tau_1} \rangle_s). \end{aligned} \quad (2.26)$$

The time integration in Eq. 2.25 extends the correlations from the 3-point functions in Eq. 2.23 to the 4-point functions in Eq. 2.26. At this point, we can write down the equations of motion for the 4-point correlation functions that appear in Eq. 2.26, which will depend on even higher order correlation functions. To decouple this hierarchy, we assume “local stationarity”: the idea is that on the kinetic time scale  $1 \ll t \ll \epsilon^{-1}$ , the  $\langle \dots \rangle_s$  distribution does not change and on a space scale  $1 \ll l \ll \epsilon^{-1}$ , these distributions are statistically independent and are well approximated by Gaussian measures.

Assuming that the  $\langle \dots \rangle_s$  terms in Eq. 2.26 satisfy the condition of local stationarity, the 4-point functions can be written as a sum of products of 2-point pairs

using Isserlis' theorem<sup>8</sup>

$$\begin{aligned} \langle a_{k_1} a_{k_2} a_{l_1} a_{l_2} \rangle_s &= \langle a_{k_1} a_{k_2} \rangle_s \langle a_{l_1} a_{l_2} \rangle_s + \langle a_{k_1} a_{l_1} \rangle_s \langle a_{k_2} a_{l_2} \rangle_s \\ &\quad + \langle a_{k_1} a_{l_2} \rangle_s \langle a_{k_2} a_{l_1} \rangle_s . \end{aligned} \quad (2.27)$$

Then, the 4-point function terms take the following form

$$\langle a_{k_1, \sigma_1} a_{k_2, \sigma_2} a_{l_1, \tau_1} a_{l_2, \tau_2} \rangle \propto W^\epsilon(\eta', k') W^\epsilon(\eta'', k'') \quad (2.28)$$

where we have switched to a set of Wigner variables

$$k_1 = k' - \epsilon \sigma_1 \eta'/2 \quad (2.29)$$

$$k_2 = k'' - \epsilon \sigma_2 \eta''/2 \quad (2.30)$$

$$l_1 = k' + \epsilon \sigma_1 \eta'/2 \quad (2.31)$$

$$l_2 = k'' + \epsilon \sigma_2 \eta''/2. \quad (2.32)$$

With the necessary approximations in place, the remaining task is to show that the last term will in Eq. 2.25 will map to the collision operator of the Boltzmann Transport Equation. We direct the reader to the references for the detailed manipulations. As was done for the free-streaming case, the penultimate piece is to take the  $\epsilon \rightarrow 0$  limit so the kinetic equation then becomes the full-fledged Boltzmann Transport Equation:

$$\frac{\partial}{\partial t} W(k, t) + \frac{1}{2\pi} \nabla \omega_k \cdot \nabla_r W(k, t) = C[W(k, t)] \quad (2.33)$$

where  $C$  is the collision operator

---

<sup>8</sup>In the quantum version of this derivation, Wick's theorem is used to preserve the time ordering of the operators [31].

$$\begin{aligned}
C[W(k, t)] = \gamma \int_{\mathbb{T}^6} (\omega_k \omega_{k_1} \omega_{k_2})^{-1} & (2\delta(\omega_k + \omega_{k_1} - \omega_{k_2})\delta(k + k_1 - k_2) \\
& (W(k_1, t)W(k_2, t) + W(k, t)W(k_2, t) - W(k, t)W(k_1, t)) \\
& + \delta(\omega_k - \omega_{k_1} - \omega_{k_2})\delta(k - k_1 - k_2) \\
& (W(k_1, t)W(k_2, t) - W(k, t)W(k_2, t) - W(k, t)W(k_1, t))). 
\end{aligned} \tag{2.34}$$

The final step is the linearization of the collision operator.

$$W = W_\beta + W_\beta \tilde{W}_\beta f \tag{2.35}$$

where  $\tilde{W}_\beta = W_\beta + 1^9$  and we have Taylor expanded about the equilibrium distribution<sup>10</sup>. For the classical case, the solution that satisfies  $C[W(k, t)] = 0$  is

$$W_\beta = \frac{1}{\beta \omega_k} \tag{2.36}$$

where  $\beta = (k_B T)^{-1}$ . For the quantum case, one obtains the expected Bose-Einstein distribution

$$W_\beta = \frac{1}{e^{\beta \omega_k} - 1} \tag{2.37}$$

which will be used for the remainder of this work. So Eq. 2.33 becomes the linear BTE (LBTE)

$$\frac{\partial}{\partial t} f + \frac{1}{2\pi} \nabla \omega_k \cdot \nabla_r f = -L f \tag{2.38}$$

where  $L$  is the linearized collision operator defined as

---

<sup>9</sup>Some authors implicitly add the  $\nabla T$  term to  $f$ .

<sup>10</sup>A further linearization of the nonequilibrium distribution where the actual temperature rise is assumed to be small will be discussed in the following sections.

$$\begin{aligned}
Lf_k = & \frac{\gamma}{W_\beta \tilde{W}_\beta} \int_{\mathbb{T}^6} (\omega_k \omega_{k_1} \omega_{k_2})^{-1} \\
& (2\delta(\omega_k + \omega_{k_1} - \omega_{k_2})\delta(k + k_1 - k_2) \tilde{W}_{k,\beta} \tilde{W}_{k_1,\beta} W_{k_2,\beta} (f_k + f_{k_1} - f_{k_2})) \\
& + \delta(\omega_k - \omega_{k_1} - \omega_{k_2})\delta(k_0 - k_1 - k_2) \tilde{W}_{k,\beta} W_{k_1,\beta} W_{k_2,\beta} (f_k - f_{k_1} - f_{k_2}))
\end{aligned} \tag{2.39}$$

where we have kept terms that are first order in  $f$ . Or, equivalently, in a more concise form

$$Lf_k = \sum_{k_1, k_2} (P_{k,k_1}^{k_2} (f_k + f_{k_1} - f_{k_2}) + \frac{1}{2} P_k^{k_1, k_2} (f_k - f_{k_1} - f_{k_2})) \tag{2.40}$$

where

$$P_{k,k_1}^{k_2} = \gamma (\omega_k \omega_{k_1} \omega_{k_2})^{-1} n_k^0 n_{k_1}^0 (n_{k_2}^0 + 1) (\omega_k + \omega_{k_1} - \omega_{k_2}) \delta(k + k_1 - k_2) \tag{2.41}$$

and

$$P_k^{k_1, k_2} = \gamma (\omega_k \omega_{k_1} \omega_{k_2})^{-1} n_k^0 (n_{k_1}^0 + 1) (n_{k_2}^0 + 1) (\omega_k - \omega_{k_1} - \omega_{k_2}) \delta(k - k_1 - k_2) \tag{2.42}$$

### 2.1.2 Extension to real crystals

The usefulness of the above framework comes from its convenient applicability to physical crystals. Here, we summarize the dictionary that enables the translation from the idealized anharmonic chain to 3D crystals. To start, the Hamiltonian (Eq.2.1) for a 3D crystal now becomes [30]

$$H = T + V \tag{2.43}$$

where  $T$  is the kinetic energy and  $V$  is the potential defined as

$$\begin{aligned}
V = V_0 + \sum_{l\mathbf{b},\alpha} \frac{\partial V}{\partial u_\alpha(l\mathbf{b})} |_0 u_\alpha(l\mathbf{b}) + \frac{1}{2} \sum_{l\mathbf{b},l'\mathbf{b}',\alpha,\beta} \frac{\partial^2 V}{\partial u_\alpha(l\mathbf{b}) \partial u_\beta(l'\mathbf{b}')} |_0 u_\alpha(l\mathbf{b}) u_\beta(l'\mathbf{b}') \\
+ \frac{1}{3!} \sum_{l\mathbf{b},l'\mathbf{b}',l''\mathbf{b}'',\alpha,\beta,\gamma} \frac{\partial^3 V}{\partial u_\alpha(l\mathbf{b}) \partial u_\beta(l'\mathbf{b}') \partial u_\gamma(l''\mathbf{b}'')} |_0 u_\alpha(l\mathbf{b}) u_\beta(l'\mathbf{b}') u_\gamma(l''\mathbf{b}'') + \dots
\end{aligned} \tag{2.44}$$

where  $u_\alpha(l\mathbf{b})$  denotes the displacement of the  $b$  basis atom in the  $l$  unit cell in the  $\alpha$  direction. This expansion admits a natural definition of force constants. The harmonic forces constants are defined by

$$\Phi_{\alpha\beta}(l\mathbf{b}, l'\mathbf{b}') = \frac{\partial V}{\partial u_\alpha(l\mathbf{b}) \partial u_\beta(l'\mathbf{b}')} |_0 \tag{2.45}$$

and the third-order force constants are defined by

$$\Psi_{\alpha\beta\gamma}(l\mathbf{b}, l'\mathbf{b}', l''\mathbf{b}'') = \frac{\partial^3 V}{\partial u_\alpha(l\mathbf{b}) \partial u_\beta(l'\mathbf{b}') \partial u_\gamma(l''\mathbf{b}'')} |_0. \tag{2.46}$$

Using the harmonic force constants and neglecting higher order force constants for a moment, a harmonic (or normal mode) basis description of the system is obtained from the equations of motion

$$m_b \partial_{tt} u_\alpha(l\mathbf{b}) = - \sum_{l'\mathbf{b}'\beta} \Phi_{\alpha\beta}(l\mathbf{b}, l'\mathbf{b}') u_\beta(l'\mathbf{b}') \tag{2.47}$$

and then Fourier transforming the above

$$\omega^2 U_\alpha(\mathbf{q}\mathbf{b}) = \sum_{h'b'\beta} \frac{1}{\sqrt{m_b m_{b'}}} \Phi_{\alpha\beta}(\mathbf{0}\mathbf{b}, h\mathbf{b}') U_\beta(\mathbf{q}\mathbf{b}') e^{i\mathbf{q}' \cdot \mathbf{h}} \tag{2.48}$$

where  $\mathbf{h} = \mathbf{l}' - \mathbf{l}$ , yields the characteristic equation

$$|D_{\alpha\beta}(\mathbf{q}\mathbf{b}\mathbf{b}') - \omega^2 \delta_{\alpha\beta} \delta_{bb'}| = 0 \tag{2.49}$$

where

$$D_{\alpha\beta}(\mathbf{q}\mathbf{b}\mathbf{b}') = \frac{1}{\sqrt{m_b m_{b'}}} \sum_h \Phi_{\alpha\beta}(\mathbf{0}\mathbf{b}, \mathbf{h}\mathbf{b}') e^{i\mathbf{q}\cdot\mathbf{h}}. \quad (2.50)$$

By solving the eigenvalue problem of Eq. 2.49 for all  $q$  in the first Brillouin zone (BZ), we obtain the familiar phonon dispersion, where the phonon frequencies are the square root of the eigenvalues. An example phonon dispersion for silicon is shown in Figure 2-2. The eigenvectors, also referred to as polarization vectors, form a complete basis that can be used to study phonons from a normal mode perspective [41].

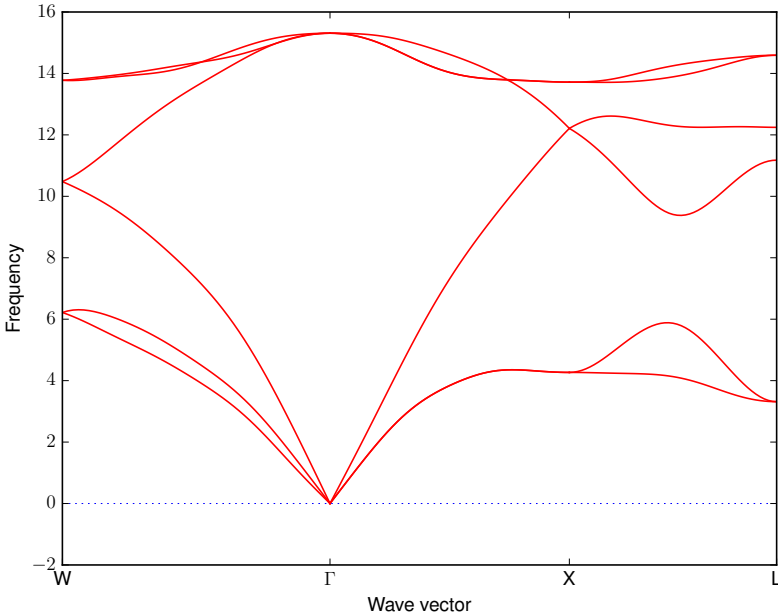


Figure 2-2: Phonon dispersion for silicon obtained using force constants from DFT calculations. Frequency in THz.

To include the anharmonic portion of the potential energy, we begin by Fourier transforming 2.46

$$V_3(\mathbf{q}s, \mathbf{q}'s', \mathbf{q}''s'') = \sum_{bb'b'', \alpha, \beta, \gamma} \left( \frac{\hbar^3}{8m_b m_{b''} m_{b'''} \omega_{\mathbf{q}s} \omega_{\mathbf{q}'s'} \omega_{\mathbf{q}''s''}} \right)^{1/2} e_{\mathbf{q}s}^{b,\alpha} e_{\mathbf{q}'s'}^{b',\beta} e_{\mathbf{q}''s''}^{b'',\gamma} \Psi_{\alpha\beta\gamma}(\mathbf{q}\mathbf{b}, \mathbf{q}'\mathbf{b}', \mathbf{q}''\mathbf{b}'') \quad (2.51)$$

where  $e_{qs}^{b,\alpha}$  is the  $b, \alpha$  component of the  $\mathbf{q}s$  eigenvector and

$$\Psi_{\alpha\beta\gamma}(\mathbf{q}\mathbf{b}, \mathbf{q}'\mathbf{b}', \mathbf{q}''\mathbf{b}'') = \sum_{l,l',ll'} \Psi_{\alpha\beta\gamma}(l\mathbf{b}, l'\mathbf{b}', l''\mathbf{b}'') e^{i\mathbf{q}\cdot\mathbf{l}} e^{i\mathbf{q}'\cdot\mathbf{l}'} e^{\mathbf{q}''\cdot\mathbf{l}''}. \quad (2.52)$$

The second and third force constants can be obtained using empirical potentials [42] or from first principles [43, 44]. Invoking the dictionary of the 1D chain from Section 2.1.1 and applying the same linearization of Eq 2.39, Eqs. 2.41 and 2.42, which, by matching  $k \rightarrow \mathbf{q}s \rightarrow n$ , become

$$P_{n,n'}^{n''} = V_3(n, n', n'') (\omega_n \omega_{n'} \omega_{n''})^{-1} n_n^0 n_{n'}^0 (n_{n''}^0 + 1) (\omega_n + \omega_{n'} - \omega_{n''}) \delta(n + n' - n'') \quad (2.53)$$

and

$$P_n^{n',n''} = V_3(n, n', n'') (\omega_n \omega_{n'} \omega_{n''})^{-1} n_n^0 (n_{n'}^0 + 1) (n_{n''}^0 + 1) (\omega_n - \omega_{n'} - \omega_{n''}) \delta(n - n' - n'') \quad (2.54)$$

where we have used

$$n_n = n_n^0 + n_n^0 (n_n^0 + 1) f_n^{ex} \nabla T. \quad (2.55)$$

The linear collision operator in matrix form is then

$$A_{n,n'} = \left( \sum_{n'',n'''} \left( P_{n,n'''}^{n''} + \frac{P_{n''',n''}^n}{2} \right) + \sum_{n''} P_{n,n''}^{isot} \right) \delta_{n,n'} - \sum_{n''} (P_{n,n''}^{n'} - P_{n,n'}^{n''} + P_{n',n''}^n) + P_{n,n'}^{isot}. \quad (2.56)$$

We now have all the necessary ingredients to write down an expression for the bulk thermal conductivity. In a bulk system in steady state under a weak temperature gradient, the microscopic flux is defined as

$$\begin{aligned}
Q &= \frac{1}{N_0 V} \sum_n v_n \hbar \omega_n n_n \\
&= \frac{1}{N_0 V k_B T^2} \sum_n v_n \hbar \omega_n n_n^0 (n_n^0 + 1) f_n^{ex} \nabla T
\end{aligned} \tag{2.57}$$

where  $N_0$  the number of discretized  $q$  points and  $V$  is the volume of the BZ. The heat flux is macroscopically related to Fourier's law

$$Q = -k \nabla T. \tag{2.58}$$

The bulk thermal conductivity tensor  $k$  can be written as

$$k_{bulk} = -\frac{\hbar}{N_0 V k_B T^2} \sum_n v_n \omega_n n_n^0 (n_n^0 + 1) f_n^{ex}. \tag{2.59}$$

$f_{n'}^{ex}$  can then be found by solving the steady state LBTE

$$-v_n \hbar \omega_n n_n^0 (n_n^0 + 1) = A_{n,n'} f_{n'}^{ex} \tag{2.60}$$

which is a straightforward inversion problem for  $f^{ex}$ . The existence of an inverse is necessary (but not sufficient as will be discussed) for a finite thermal conductivity. <sup>11</sup>

### 2.1.3 Application of BTE to nanoscale thermal transport

The bulk LBTE can be extended to study systems which are *not bulk*, like thin films or nanowires, or systems where the length scale of the heating profile is commensurate with the mean free path of the phonons or where the time scale is commensurate with the phonon-phonon scattering time. This will be discussed in detail in the following chapters, but some points of connection with the derivation above should be mentioned. To begin, this work will use a deviational form of the LBTE

---

<sup>11</sup>Spohn pointed out that  $L$  has a nondegenerate 0 eigenvalue, but the eigenvector is orthogonal to the streaming operator of BTE (the left-hand side of Eq. 2.60, so inversion is indeed guaranteed [31].

$$\frac{\partial g_n}{\partial t} + \vec{v}_n \cdot \nabla g_n = \sum_{n'} \tilde{\Omega}_{n,n'} (g_{n'}^0 - g_{n'}) \quad (2.61)$$

where  $g_n = \frac{\hbar\omega_n}{Nv} \left( f_n - f_{BE}(\frac{\hbar\omega_n}{k_B T_0}) \right)$  and  $g_n^0 = \frac{\hbar\omega_n}{Nv} \left( f_n^0 - f_{BE}(\frac{\hbar\omega_n}{k_B T_0}) \right) = c_n \delta T$ . The discrete sums can be converted to continuous integrations over the Brillouin zone as  $\sum_n() = \sum_{s=1}^b \sum_k() \rightarrow \sum_{s=1}^b Nv \int \frac{d^d k}{(2\pi)^d}()$ , where  $s$  is an index running over the  $b$  branches of phonons. The collision matrix  $\tilde{\Omega}$  in this deviational form is related to the collision matrix of Eq. 2.56 by

$$\tilde{\Omega}_{n,n'} = \omega_n A_{n,n'} \frac{1}{\omega_{n'}} \frac{1}{f_{n'}^0 (f_{n'}^0 + 1)}. \quad (2.62)$$

We have seen how the LBTE is capable of recovering the diffusive regime governed by a bulk thermal conductivity (see Eq. 2.59), but how does the BTE framework recover the opposite extreme: the ballistic regime? The ballistic regime is recovered by setting the scattering kernel to zero so that the LBTE becomes

$$\frac{\partial g_n}{\partial t} + \vec{v}_n \cdot \nabla g_n = 0 \quad (2.63)$$

which is identical to the free streaming solution of Eq. 2.21. Solutions to Eq. 2.63 can be expressed as a sum of weighted cosines, which will only converge in the continuous limit. In the following chapters, the intermediate regimes between purely ballistic and purely diffusive will be discussed. In Chapter 4, we will investigate the relationship between geometry and thermal transport using the relaxation time approximation (RTA), which can be expressed simply by setting the off-diagonal elements of  $\tilde{\Omega}_{n,n'}$  to zero

$$\tilde{\Omega}_{n,n} = \frac{1}{\tau_n}. \quad (2.64)$$

In Chapter 5, we will present a theoretical framework for studying size and hydrodynamic effects using the LBTE with the collision matrix. The point of entry is to add a source term  $Q_n$  to the right hand side of the Eq. 2.61. Physically, this represents

a heating (cooling) source (sink) that one encounters in relevant geometries like those generated in transient thermal grating experiments.

### 2.1.4 Some remarks concerning the origin of thermal resistance

The long history of the question of what governs the emergence of irreversible macroscopic behaviour from reversible microscopic dynamics casts its long shadow once more. In the present context, how do the deterministic dynamics of a given Hamiltonian unavoidably lead to the dissipation of energy and consequently yield a finite resistance? While a rigorous answer to this question is still an active area of research [45], a conceptual one is presented. First consider an electron moving through a medium. The electron inevitably interacts with other electrons, imperfections or the lattice itself, its energy is transferred and entropy is generated. Each interaction is subject to the laws of thermodynamics and thus heat is unavoidably generated. But how can this picture apply to phonons, which are heat carriers to begin with? How is the second law of thermodynamics satisfied in the context of phonon transport? The answer is that phonons act as each others thermodynamic bath and, because of energy conservation, the treatment of this interaction must be done in a self-consistent way.<sup>12</sup><sup>13</sup> To begin, a self-consistent treatment of phonon thermalization requires energy conservation. The original non-linear collision operator, Eq. 2.34, satisfies energy conservation simply<sup>14</sup>

$$\int_k \omega_k C[W(k, t)] = 0. \quad (2.65)$$

The linearization of the collision operator,  $\tilde{\Omega}$ , does not break the property of energy conservation. Inserting  $g_n^0 = \delta T c_n$  and  $\delta T = \frac{1}{C} \sum_n g_n$  into the right hand side of Eq. 2.61, energy conservation requires

---

<sup>12</sup>This is in contrast to the device-environment pictures, where the environment is so large that any change in its energy is taken to be negligible.

<sup>13</sup>This is a necessary condition for thermalization, in contrast to localization [46].

<sup>14</sup>This is strictly true for isotopically pure systems, while isotopic scattering can be modeled to be energy conserving.

$$\sum_{n,n'} \tilde{\Omega}_{n,n'} \left( \sum_{n''} g_{n''} \frac{c_{n'}}{C} - g_{n'} \right) = 0. \quad (2.66)$$

Since this equality must be satisfied for an arbitrary distribution of modes  $g_n$ ,  $\tilde{\Omega}$  is constrained by

$$\sum_n \tilde{\Omega} e_n = \frac{1}{C} \sum_n \tilde{\Omega} \vec{c} \quad (2.67)$$

which must be true for every phonon mode indexed by  $n \in M$  where  $e_n$  is a unit Cartesian vector and  $\vec{c}$  is the vector of modewise specific heat. For a scattering matrix which satisfies the condition of Eq. 2.67, the system is energy conserving in any heat transfer configuration.

For the RTA, setting the off-diagonal elements to zero (Eq. 2.64), and using the constraint imposed by Eq. 2.67, we find the following restriction for the relaxation times in order for the system to be energy conserving

$$\frac{1}{\tau_n} = \frac{1}{C} \sum_j \frac{c_j}{\tau_j}. \quad (2.68)$$

This equation is satisfied if and only if the relaxation times are identical for all modes. Thus, the only conserving diagonal matrix  $\tilde{\Omega}$  is one where all of the diagonal entries are the same, which is only satisfied if  $\tilde{\Omega}$  is an identity matrix with a single relaxation time. What is typically done to alleviate the breaking of energy conservation for the RTA is a re-definition of the temperature, such that the energy conservation equation is used to obtain a temperature, called the pseudo-temperature as opposed to a temperature defined from the energy density given by  $\delta T = \frac{1}{C} \sum_n g_n$  [47]. The collision matrix is formally energy conserving and the temperature is justifiably defined from the energy density.

How does a self-consistent treatment of phonon scattering relate to a finite value of thermal conductivity? The literature traditionally draws a category between two types of scattering: Normal (also known as momentum conserving) and Umklapp (also known as momentum destroying) processes. It is said that Umklapp processes

are responsible for a finite thermal resistance. Normal scattering is defined as

$$k_1 \pm k_2 - k_3 = 0 \quad (2.69)$$

and Umklapp scattering is defined as

$$k_1 \pm k_2 - k_3 = G \quad (2.70)$$

where  $G$  is a reciprocal lattice vector. This distinction between Normal and Umklapp is used in the Callaway approximation to the BTE, which will be reviewed in Chapter 5 as part of the work on phonon hydrodynamics.

However, the distinction between Normal and Umklapp isn't unique. As pointed out in Ref. [48], the definition of the Brillouin zone is not unique and thus the distinction between Normal and Umklapp is not gauge invariant as shown in Figure 2-3.<sup>15</sup> For instance, one can ask what would be the equivalent distinction between Normal and Umklapp scattering in an amorphous system? The existence of gauge invariant normal scattering processes remains an open question.

---

<sup>15</sup>This is reminiscent of the gauge fixing that is necessary in the Feynman integral calculations [49] to account for the invariance of the Lagrangian under the action of a Lie group. To the author's knowledge, no work has studied the relationship between the collision operator and the relevant Lie groups. A step in this direction has been taken by Togo et al. who used point and space group symmetries to remove the redundancy in the 3-phonon scattering calculation [50].

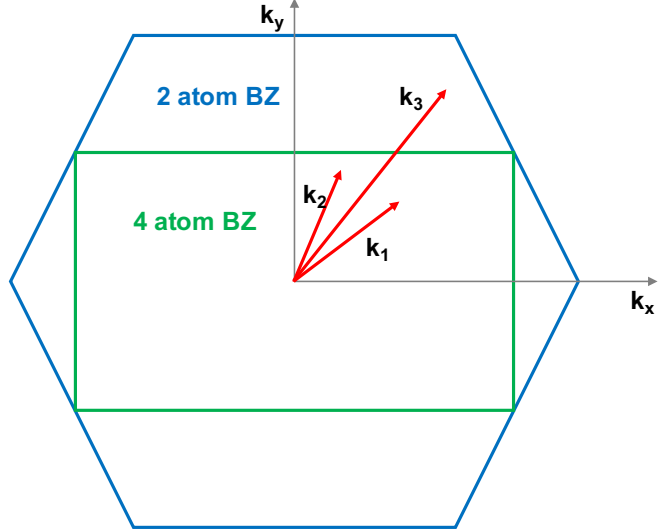


Figure 2-3: An example of a 3-phonon scattering process in graphene (or any 2D material with the same lattice as graphene) that is considered to be a Normal process in the 2-atom BZ but an Umklapp process in the 4-atom BZ.

Peierls observed that Normal scattering events preserve the non-equilibrium phonon distribution and keenly pointed out that, in the absence of other types of scattering, a heat current, that was generated at some time in past due to an imposed temperature gradient, would continue to persist indefinitely even upon the removal of this temperature gradient. The resolution is that at any non-zero temperature, other types of scattering (or entropy generating events) cannot be avoided if the phonon system is considered in a self-consistent way. As pointed out in [48], if we extend our dispersion to include a minimum of two branches (say LA and TA) such that each branch has a distinct group velocity, then indeed, momentum conserving events can reverse the direction of heat flux, as shown in Figure 2-4. Finally, going beyond classical transport, it has been shown that Umklapp scattering is not a necessary requirement for the existence of a finite resistance [51].

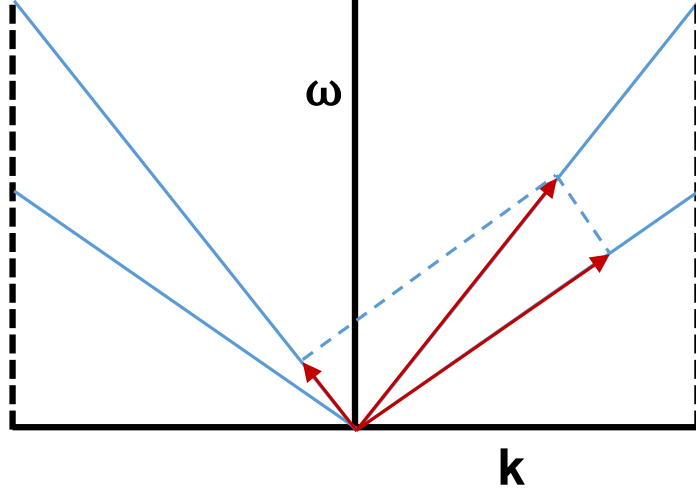


Figure 2-4: Debye dispersion with two branches. Arrows denote modes involved in a Normal process that reverses momentum.

We take care to point out if one (a Peierls demon) were to exclude all other types of scattering except for Normal scattering, the resulting collision operator would not necessarily obey Boltzmann's famous H-Theorem in the strong sense. This can be clearly seen from the definition of H

$$H(t) = \int d^3p d^3q f(p, q, t) \ln f(p, q, t). \quad (2.71)$$

As a gedanken, consider a three-phonon system (i.e.: a discretization of the BZ) characterized by single phonon branch with a Debye dispersion, as depicted in Figure 2-5.

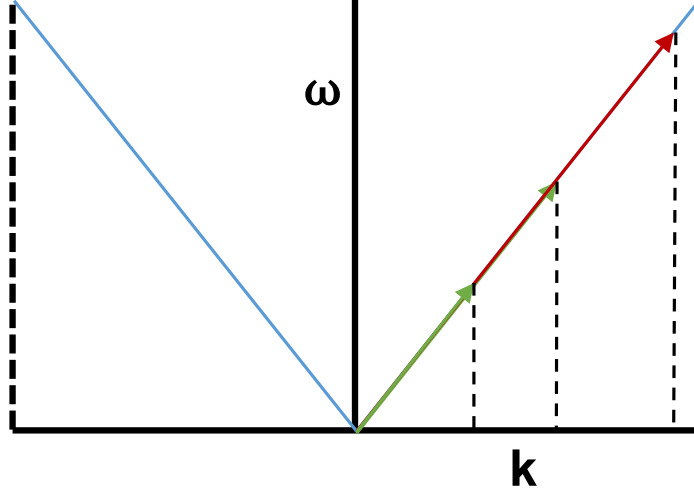


Figure 2-5: Debye dispersion with three phonon modes where each arrow corresponds to a single mode.

A possible normal collision operator for such a system that satisfies the condition 2.69 could have the following properties

$$\begin{aligned} N|a, b, c\rangle &= |e, f, g\rangle \\ N|e, f, g\rangle &= |a, b, c\rangle . \end{aligned} \tag{2.72}$$

Here  $N = N^{-1}$  and  $H(t)$  does not decrease with time, but oscillates. Thus, a normal collision operator potentially has a non-trivial fixed point.<sup>16</sup> A complete collision operator, on the other hand, necessarily has the following property

$$\lim_{n \rightarrow \infty} C^n f = 0 \tag{2.73}$$

and is symmetric (time reversal) and positive semidefinite (any number of phonons at any time is always  $\geq 0$ ). Under the ergodic assumption <sup>17</sup>, a complete collision operator has only one fixed point, the trivial one. This is equivalent to the statement that thermalization always occurs under the BTE. Equivalently, since there is a single

---

<sup>16</sup>Another confusing subtlety is that the Normal operator can, but is not required to, satisfy ergodicity.

<sup>17</sup>In the phonon systems discussed here, ergodicity is defined as follows: for any  $k$  there exists a finite number of processes that will bring  $k$  to any other  $k'$ .

zero eigenvalue, there is only a single conserved quantity: energy [52].<sup>18</sup> Given the above nuances, this work will treat Normal, Umklapp and disorder processes on equal footing within the BTE framework.

### 2.1.5 Numerical techniques for solving the BTE

Solving the phonon BTE for complex geometries requires a numerical approach. The Variance Reduced Monte Carlo (VRMC) approach to solving the phonon BTE under the RTA was first described by Peraud et al. [53, 54]. At its core, VRMC is simulating the random walking of individual phonons as they propagate according to their group velocity and scatter according to their lifetime. This is illustrated in Figure 2-6.

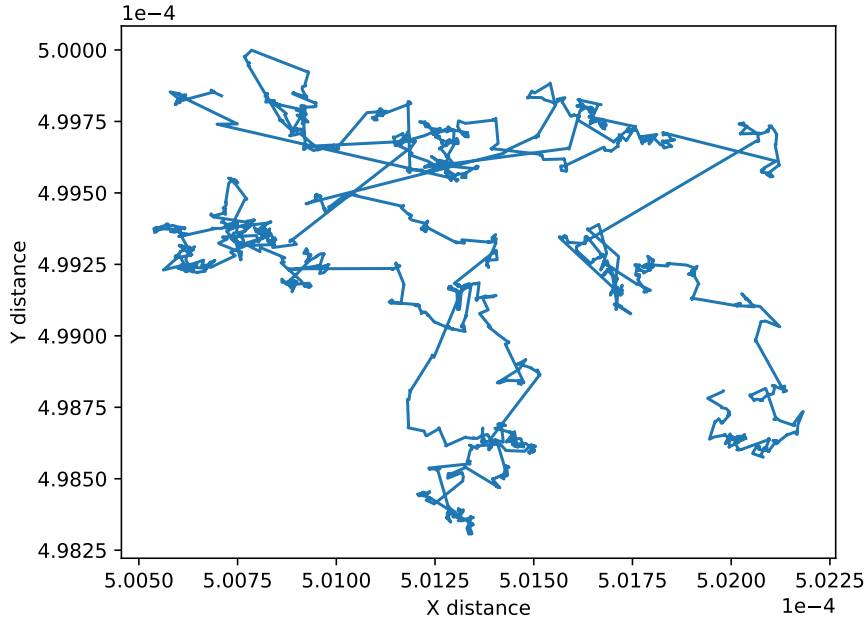


Figure 2-6: Example of the random walk taken by a particle in VRMC as part of a simulation of phonon transport in silicon at room temperature.

The computational efficiency of VRMC is due to two observations: the first is that energy conservation is satisfied by conserving the number of simulated particles and

---

<sup>18</sup>In the phonon hydrodynamics literature, quasi-momentum is treated as a conserved quantity. Clearly, this is not strictly true for all times. However, it appears to produce a reasonable picture for times  $t$  where  $\tau_{\text{boundary}} > t > \tau_{\text{Normal}}$ .

the second is that an individual phonon scattering event does not require knowledge on the difference between the local and equilibrium temperature because the normalized distributions from which phonons are sampled is temperature independent. Algorithm 1 presents the order of operations of this MC technique.

---

**Algorithm 1** *Variance Reduced MC*


---

**Require:** Phonon properties:  $v_v$ ,  $\tau_v$ ,  $\omega_v$ ,  $DOS(v)$

```

1:  $v \leftarrow \tau_v DOS(v) dv$ 
2: while  $t < \text{total time}$  do
3:   if  $x + v_v \tau_v$  intersects boundary then
4:      $v \leftarrow \text{boundary conditions}$  (i.e.: diffuse or specular)
5:   else (Simulate phonon-phonon scattering)
6:      $v' \leftarrow \tau_{v'} DOS(v') dv'$ 
7:      $v \leftarrow v'$ 
8:   Record position and time of  $v$  to perform averaging to return observable  $O$ 
return  $O$ 


---


end

```

---

Using VRMC, it is a straightforward exercise to track phonons and perform statistical averaging of the quantities of interest (i.e.: temperature, heat flux, etc.). For example, the mean square displacement as a function of time of the phonons can be calculated. In Figure 2-7, the scaling of the mean square displacement (MSD) with time can be seen to clearly delineate between the ballistic and the diffusive regimes.

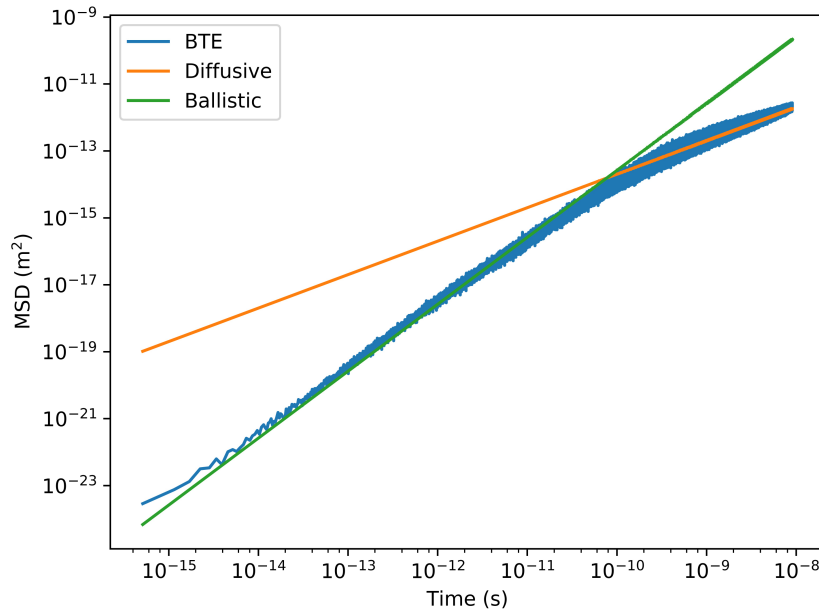


Figure 2-7: Mean square displacement as a function of time obtained from a VRMC simulation of a volumetric point heat source in bulk silicon at 300 K.

## 2.2 Experimental Techniques

### 2.2.1 Time-domain thermoreflectance

Time-domain thermoreflectance (TDTR) has been described in detail in the literature [18, 55] and is briefly reviewed here. The Nanoengineering Group at MIT uses a pulsed laser (Ti:Sapphire) at 800 nm with a repetition rate of 80.7 MHz and a pulse width of approximately 200 fs and a power per pulse of 15 nJ from which the pump and probe beams are split using a polarizing beam splitter. Since the changes in the sample's surface reflectance due to changes in temperature are small ( $O(10^{-4})$ ), a lockin-amplifier detection scheme is used. The pump beam passes through an electro-optic modulator and then converted to 400 nm using a BIBO crystal prior to striking the sample surface. The probe beam passes through the delay stage and the optical elements (see Figure 2-8) before striking the sample surface. The reflected probe is thus modulated at the same frequency of the pump. A photodiode coupled with an

optical blue filter collects the probe signal, which is then passed to the lockin amplifier that is collecting at the selected modulation frequency. Due to the interplay of sensitivity and noise, the data presented here was collected at modulation frequencies between 3 and 12 MHz.

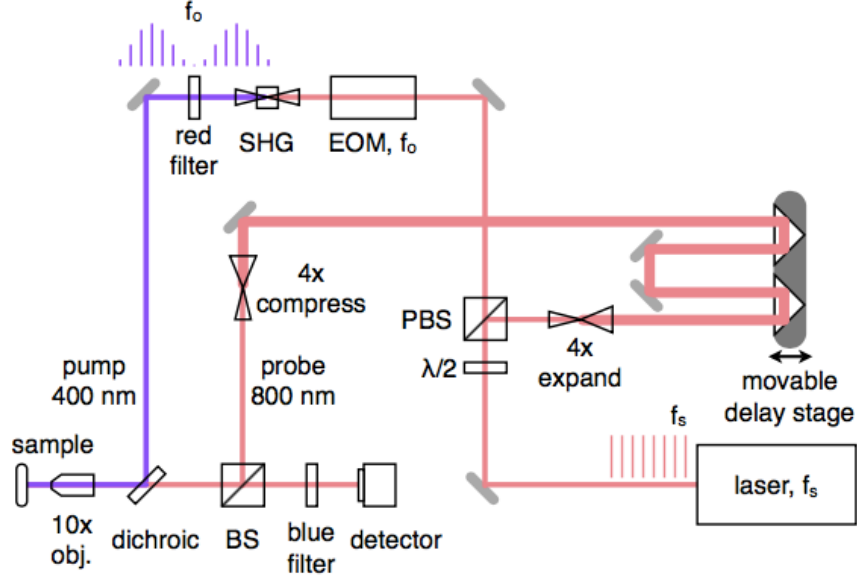


Figure 2-8: Diagram of the TDTR setup used in this work to perform the thermal conductivity measurements. Courtesy Kimberlee Collins.

The time traces obtained from TDTR are interpreted using a multi-layer solution to the heat diffusion equation [18, 55]. The heat transfer model of the TDTR geometry begins with the heat equation in cylindrical coordinates

$$C \frac{\partial T}{\partial t} = \frac{k_r}{r} \frac{\partial}{\partial r} \left( r \frac{\partial T}{\partial r} \right) + k_z \frac{\partial^2 T}{\partial z^2} \quad (2.74)$$

where  $C$  is the volumetric specific heat,  $k_r$  is the radial component of the thermal conductivity tensor and  $k_z$  is the axial component of the thermal conductivity. Using Fourier and Hankel transforms (denoted by  $\tilde{\cdot}$ ), the heat equation becomes

$$i\omega C \tilde{T} = -k_r k^2 \tilde{T} + k_z \frac{\partial^2 \tilde{T}}{\partial z^2} \quad (2.75)$$

where  $\omega$  is the frequency Fourier transform variable and  $k$  is the spatial Hankel transform variable. Rearranging using  $q^2 = (k_r k^2 + i\omega C)/k_z$  gives

$$\frac{\partial^2 \tilde{T}}{\partial z^2} = q^2 \tilde{T}. \quad (2.76)$$

This form is amenable to the thermal quadrupole framework, meaning that we can construct a sequence of solution to the equations that is physically representative of a layered system. For an individual layer, we define

$$M_n = \begin{bmatrix} \cosh(qd) & \frac{-1}{k_z q} \sinh(qd) \\ -k_z q \sinh(qd) & \cosh(qd) \end{bmatrix} \quad (2.77)$$

where  $d$  is the layer thickness. For an interface

$$M_n = \begin{bmatrix} 1 & G^{-1} \\ 0 & 1 \end{bmatrix} \quad (2.78)$$

where  $G^{-1}$  is the interface conductance. Using these definitions, we can construct a representation of our layered system

$$\begin{bmatrix} \tilde{T}_{bottom} & \tilde{q}_{bottom} \end{bmatrix} = M_n M_{n-1} \dots M_1 = \begin{bmatrix} A & B \\ C & D \end{bmatrix} \tilde{T}_{top} \tilde{q}_{top} \quad (2.79)$$

where  $\tilde{q}$  is the Fourier-Hankel domain heat flux. Using the condition that the bottom surface is adiabatic, we have

$$\tilde{T}_{top} = \frac{-D}{C} \tilde{q}_{top} \quad (2.80)$$

where for a Gaussian-shaped heating flux profile

$$\tilde{q}_{top} = \frac{A_o}{2\pi} \exp\left(\frac{-k^2 \omega_0^2}{8}\right). \quad (2.81)$$

The final step is to perform inverse Fourier and Hankel transforms to obtain  $T_{top}$ . With an expression for  $T_{top}$  as a function of material parameters (thermal conductivity, interface conductance, heat capacity and layer thickness), a non-linear least squares minimization against the experimental data is used to extract the unknowns of a given thermal system (typically the thermal conductivity of the film and the

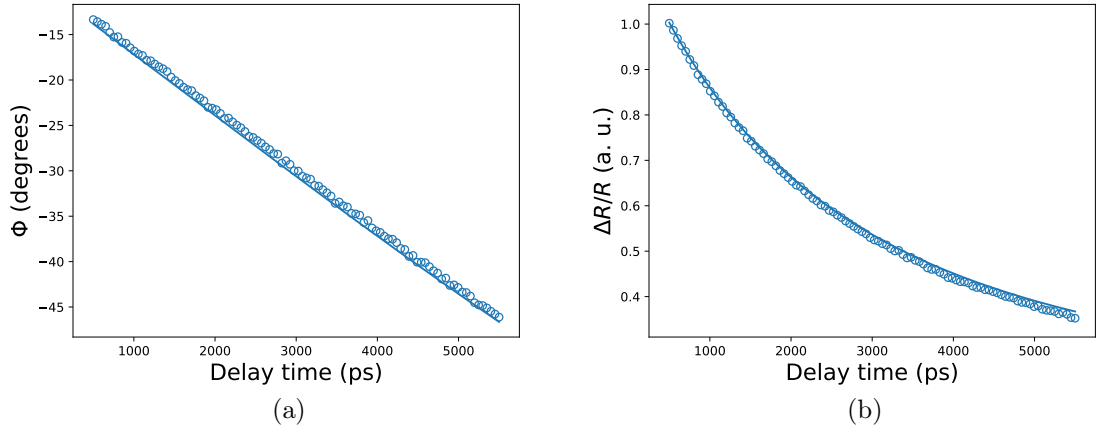


Figure 2-9: Example (a) phase and (b) amplitude TDTR traces and fits of an aluminum-sapphire sample.

interface conductance between the Aluminum layer and the film).  $T_{top}$  is a complex quantity and therefore one can fit to the amplitude or the phase, examples of which are shown in Figure 2-9<sup>19</sup>. The parameters used in the fitting procedure are reported in Appendix A.

While TDTR has been used to investigate deviations from the diffusive regime [56], in this work, the technique will be used in Chapter 3 to characterize the thermal conductivity of thin films under a Fourier law interpretation. To experimentally study thermal transport outside the diffusive regime, an alternative technique, referred to as the transient thermal grating technique, will be used.

### 2.2.2 Transient thermal grating

Transient grating spectroscopy is a variant on four-wave-mixing spectroscopic techniques that can measure thermal transport dynamics over a well-defined in-plane length scale. In this technique, two pump laser pulses (515 nm, 60 ps FWHM) are crossed at the surface of the sample, where they interfere to yield a sinusoidal intensity pattern. Absorption by the sample creates a matching temperature profile, which evolves as a function of time through in-plane and cross-plane transport. The

---

<sup>19</sup>Theoretically, one should fit to the entire complex quantity. Practically, however, this doesn't consistently yield reliable fits.

time dynamics of this “transient grating” are measured by the diffraction of a quasi-continuous probe beam (532 nm), and phase-specific information is extracted through heterodyned detection of the TTG signal by superposition of the diffracted signal with a reference beam (local oscillator) derived from the probe beam source. The signal is detected using a fast photodiode (1 GHz bandwidth) and recorded on an oscilloscope (4GHz bandwidth). Specific details of the optical setup can be found elsewhere [57, 58, 59] and a depiction of the TTG setup is shown in Figure 2-10.

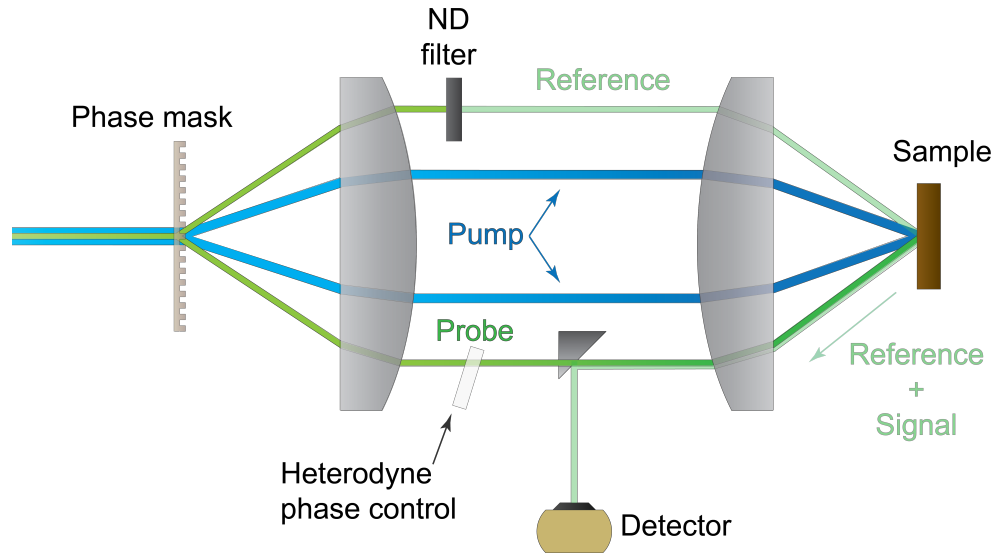


Figure 2-10: A diagram of the reflection mode TTG geometry. The pump and probe beams are passed through the diffraction grating (referred to here as the phase mask), which sets the period length of the heating profile. The  $\pm 1$  orders of the pump and probe are then imaged on the sample surface using the  $4f$  lens system. An ND filter attenuates the reference beam of the probe, while an optic (the heterodyne phase control) is placed in the signal beam of the probe to control the relative phase between the reference and the signal. The diffracted signal and the reflected reference are collected at the detector. Reproduced from [1] with permission from the American Physical Society.

The optical model of the TTG geometry is as follows. A grating of length  $L$  is defined by

$$L = \frac{2\pi}{q} = \frac{\lambda_e}{2 \sin(\theta/2)} \quad (2.82)$$

where  $q$  is the grating wavevector magnitude,  $\lambda_e$  is the optical wavelength and  $\theta$  is the angle of incidence. The optical fields for the probe beam,  $p$

$$E_p = E_{0p} \exp(i(k_p^2 - q^2/4)^{1/2}z - i(q/2)x - i\omega_p t + i\phi_p) \quad (2.83)$$

and the reference beam,  $R$

$$E_R = t_r E_{0p} \exp(i(k_p^2 - q^2/4)^{1/2}z - i(q/2)x - i\omega_p t + i\phi_R) \quad (2.84)$$

are approximated by plane waves where  $E_{0p}$  is the original amplitude of the probe,  $k_p$  is the optical wavevector,  $\omega_p$  is the optical frequency,  $\phi_p$  and  $\phi_R$  are the phases of the probe and reference beam respectively and  $t_R$  is the attenuation factor for the reference beam. The diffracted signal is obtained from a transfer function model of the grating

$$t^*(t) = r_0(1 + \cos(qx)[r'(t) + i(r''(t) - 2k_p u(t) \cos \beta_p)]) \quad (2.85)$$

where  $r'(t)$  and  $r''(t)$  denote the real and imaginary components of the reflectivity and  $u(t)$  is the vertical surface displacement. Both the reflectivity due to a dependence of the refractive index on temperature (i.e.: thermoreflectance) and the displacement due to thermal expansion encode temperature information.

The first order diffracted field of the probe is obtained by multiplying Eq. 2.83 by Eq. 2.85

$$\begin{aligned} E_{p(+1)} &= \frac{1}{2} r_0 E_{0p} [r'(t) + i(r''(t) - 2k_p u(t) \cos \beta_p)] \\ &\quad \exp(i(k_p^2 - q^2/4)^{1/2}z - i(q/2)x - i\omega_p t + i\phi_p) \end{aligned} \quad (2.86)$$

and the reflected reference field is simply obtained by multiplying Eq. 2.84 by  $r_0$

$$E_{R(0)} = r_0 t_r E_{0p} \exp(i(k_p^2 - q^2/4)^{1/2} z - i(q/2)x - i\omega_p t + i\phi_R). \quad (2.87)$$

As the reference and probe are collinear, their interference intensity is given by

$$I_s = \frac{1}{2} I_{0p} R_0 [t_r^2 + r'^2(t) + (r''(t) + 2k_p^2 u^2(t) \cos \beta_p)^2 + 2t_r(r'(t) \cos(\phi) - (r''(t) - 2k_p u(t) \cos \beta_p) \sin \phi)] \quad (2.88)$$

where  $R_0 = |r_0|^2$  and  $\phi = \phi_p - \phi_R$ . If the intensity of the reference beam is much greater than the diffracted probe beam, the signal is dominated by the last two terms of Eq. 2.88

$$I_{het} = t_r I_{0p} R_0 [r'(t) \cos \phi - (r''(t) - 2k_p u(t) \cos \beta_p) \sin \phi]. \quad (2.89)$$

Thus, the TTG signal will in principle have both real and imaginary field contributions due to “amplitude-grating” and “phase-grating” responses, respectively. The phase grating contributions contains decay components that correspond to thermal expansion and the imaginary part of the thermoreflectance and acoustic oscillations corresponding to the impulsive stimulation of surface acoustic waves (SAWs), whereas the amplitude-grating response only contains one term corresponding to the real part of the thermoreflectance [58]. Analysis of the amplitude-grating contribution is simpler due to the single contribution, and so this term was isolated during the SiGe measurements discussed in Chapter 4 by optimizing the heterodyne phase to minimize the SAW signal which only appears in the phase-grating response [58]. The phase-grating was used for the graphite measurements in Chapter 5 due to the absence of SAWs and the large contribution to the signal from thermal expansion. Example phase and amplitude grating signals are shown in Figure 2-11.

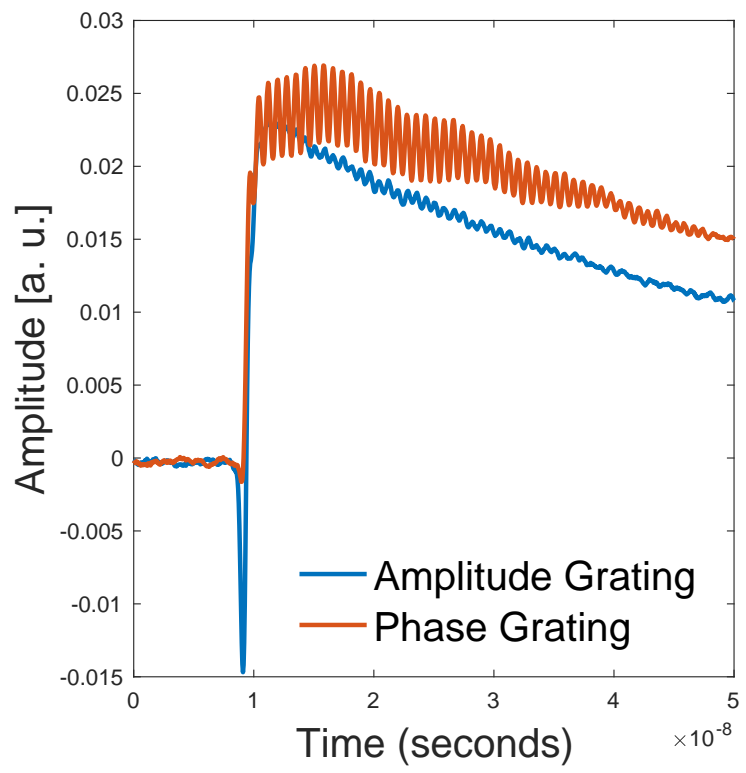


Figure 2-11: Example phase and amplitude grating traces taken from a Si<sub>93.4</sub>Ge<sub>6.6</sub> sample.

# Chapter 3

## Tuning thermal conductivity

### 3.1 Introduction

Defects such as vacancies, isotopes or alloying compounds are traditionally used to increase the scattering rates of thermal carriers, thereby reducing the thermal conductivity until a minimum is reached [60]. While the established understanding, which relies on a perturbative treatment [61, 62, 63], of defects has been successful in improving thermoelectric device performance [64, 65], it has yet to provide the insight necessary in order to obtain the large tunable ranges of thermal conductivity necessary for thermal switch applications. For example, the impact of Li<sup>+</sup> ion intercalation upon thermal conductivity has also been theoretically investigated in graphite, reporting a 3 to 5 fold change [66] and experimentally studied in MoS<sub>2</sub>, reporting a 2 to 5 fold change [67]. Recent work extended this static alloying effect to a “dynamic alloying effect” via Li<sup>+</sup> ion intercalation in the LiCoO<sub>2</sub> electrodes of electrochemical cells which yielded reversible changes of 150% to 270% in thermal conductivity [68]. Looking beyond Li<sup>+</sup> ions, a negligible effect of oxygen non-stoichiometry in La<sub>0.5</sub>Sr<sub>0.5</sub>CoO<sub>3</sub> thin films on thermal conductivity was reported [69]. On the other hand, oxygen stoichiometry was shown, for example, in Pr<sub>0.1</sub>Ce<sub>0.9</sub>O<sub>2</sub> thin films to induce a 50% change in thermal conductivity over a 10% change in the oxygen non-stoichiometry [70]. The second strategy to dynamically control thermal conductivity involves the modification of the crystal structure and the concomitant properties of

thermal carriers (i.e.: phonon dispersion, modewise specific heats, group velocities and lifetimes) via the application of mechanical, thermal or electrical work. For instance, molecular dynamics simulations have shown an exponential dependence of thermal conductivity on strain [71]. Examples of temperature-induced phase transitions include the metal to insulator transition in  $\text{VO}_2$  which relies on moving across a critical temperature of  $\sim 340$  K to affect a  $\sim 30\%$  change in thermal conductivity [72]. Similarly, in  $\text{PbTiO}_3$  thin films, a  $\sim 15\%$  change in thermal conductivity due to changes in the ferroelectric domain density as a function of electric field has been reported [73]. A recent molecular dynamics simulation of this system predicts an upper limit of  $\sim 20\%$  change in the interface conductance between ferroelectric domains [74].

In the first portion of this chapter, we report the investigation of thermal properties of epitaxial BFO thin films, grown under different conditions on different substrates. The room temperature phonon thermal conductivity is found to be almost independent of the oxygen partial pressure but dependent on the BFO polymorph. Through piezoresponse force microscopy (PFM) characterization and thermal analysis with an in-situ electric field, we observed that ferroelectric domain wall density does not play a significant role in determining the thermal conductivity. In the second part of this chapter, we make use of the interplay between defects and structure; ions are electrochemically inserted into strontium cobalt oxide ( $\text{SrCoO}_{2.5}$ , denoted as SCO) thin films and trigger phase transitions to yield large reversible changes in thermal conductivity at room temperature. This large tuning range is achieved by spanning three distinct phases induced via the incorporation of two different ions,  $\text{H}^+$  and  $\text{O}^{2-}$ .

## 3.2 BFO

$\text{BiFeO}_3$  (BFO) is a lead-free single-phase ferroelectric material of serious interest due to its complex physical properties including multiferroicity [75]. Bulk BFO exhibits a rhombohedral structure in which oxygen octahedra are slightly tilted from the center of symmetry along the  $<111>$  pseudocubic direction. When epitaxially

grown on perovskite substrates such as SrTiO<sub>3</sub> (STO), a small monoclinic distortion of the rhombohedral structure is present, and the structure is denoted as R-like BFO. In general, R-like BFO tends to polarize along the <111> directions [76], resulting in 8 possible domain variants with both in-plane and out of plane components, which is undesirable for practical applications. As a result, domain engineering of BFO thin films has been explored as a mechanism to improve the ferroelectric performance, such as by utilizing different substrates [77, 78] and tuning the buffer thickness [78, 79]. Recently, a new approach for ferroelectric domain engineering of BFO thin films has emerged with the observation of a new tetragonal polymorph with a large c/a ratio ( $\sim 1.25$ ) stabilized by much larger in-plane compressive strain ( $>4.5\%$ ) [80], with a slight monoclinic distortion [81] and therefore denoted as T-like BFO. This T-like polymorph is expected to support a simpler switching process and a higher remnant polarization. Furthermore, a reversible morphotropic phase transformation between R- and T-like BFO can be driven by simple stimuli [82, 83, 84] and the morphotropic phase boundary shows a strong electromechanical response [85, 86]. In light of these differences, we investigated the thermal transport properties of epitaxial R- and T-like BFO thin films and the dependence of thermal conductivity on the polarization state.

## Sample Details

Sample growth and characterization was performed by Shuai Ning and the details can be found in [2]. The samples are summarized in Table 3.1. The R and T-like polymorphs are obtained by substrate or underlayer strain engineering, and the film strain state, as well as the ferroelectric domain features, are controlled via the oxygen partial pressure during deposition.



Figure 3-1: Crystal structures for the (a) R-BFO and (b) T-BFO phases.

Table 3.1: BFO samples

Sample	BFO phase	Substrate	BFO film	Unit- cell	c/a ratio
			Lattice parameter (Å)	Lattice parameter (Å)	volume (Å³)
BFO/STO	R-like	$a_{STO} = c_{STO} =$	$a = 3.900$	62.25	1.049
5 mTorr		3.905	$c = 4.093$		
BFO/STO	R-like	$a_{STO} = c_{STO} =$	$a = 3.904$	61.98	1.042
100 mTorr		3.905	$c = 4.067$		
BFO/SRO/LAO	R-like	$a_{SRO} = 3.947$	$a = 3.942$	61.07	0.997
5 mTorr		$c_{SRO} = 3.930$	$c = 3.930$		
BFO/LAO	T-like	$a_{LAO} = c_{LAO} =$	$a = 3.778$	66.93	1.241
5 mTorr		3.788	$c = 4.689$		
BFO/LAO	T-like	$a_{LAO} = c_{LAO} =$	$a = 3.783$	66.13	1.222
100 mTorr		3.788	$c = 4.621$		
BFO/LSMO/LAO	T-like	$a_{LSMO} = 3.776$	$a = 3.772$	67.10	1.249
5 mTorr		$c_{LSMO} = 4.007$	$c = 4.710$		

### 3.2.1 Thermal conductivity characterization

#### Role of structure

The room temperature thermal conductivity was measured using the TDTR system described in Section 2.2.1. The thermal conductivities of the underlying layers (LSMO and SRO) and the bare substrates (STO and LAO) were first measured

(see Appendix A), and then used as known input parameters in the non-linear least squares minimization fitting procedure to obtain the cross-plane thermal conductivity of BFO thin films. To ensure that the TDTR technique is sensitive to the thermal conductivity of the BFO films, a sensitivity analysis [87, 55] was carried out and is reported Figure 3-2, indicating that the measurement is indeed sensitive to the thermal conductivity of BFO.

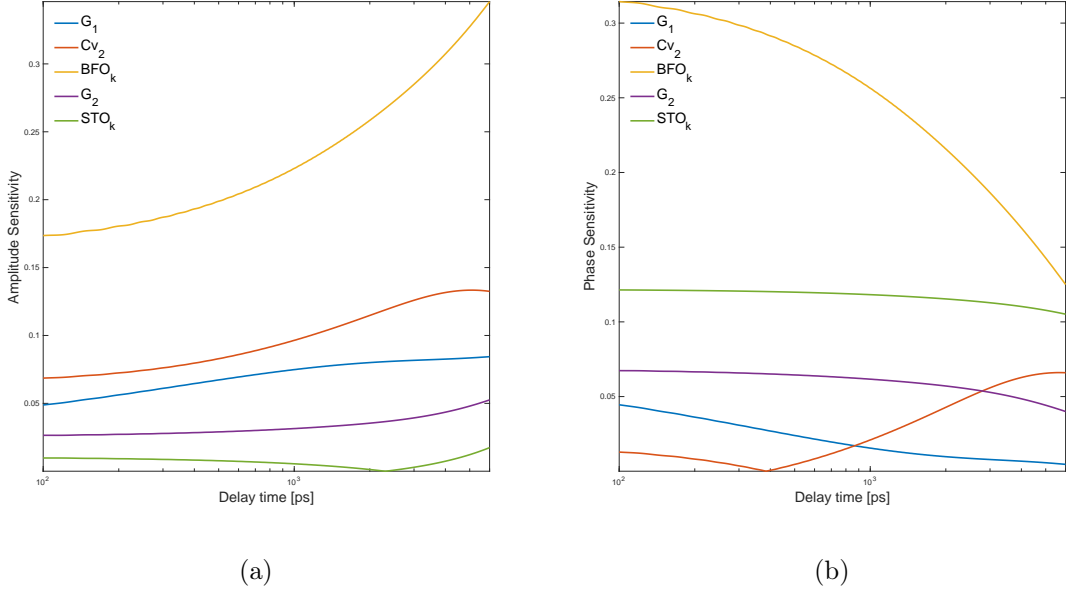


Figure 3-2: (a) Amplitude and (b) phase sensitivity for the TDTR BFO measurements. Here,  $BFO_k$  corresponds to the BFO thermal conductivity,  $G_1$  corresponds to the interface conductance between aluminum and BFO,  $Cv_2$  corresponds volumetric heat capacity of BFO,  $G_2$  corresponds to the interface conductance between BFO and STO and  $STO_k$  corresponds to the STO substrate thermal conductivity.

To ensure that the fitting procedure yielded a local minimum, the error landscape was calculated. Sample error landscapes are shown in Figure 3-3, where a local minimums are found for both the R-like and T-like films. Example fits to phase and amplitude are shown in Figure 3-4.

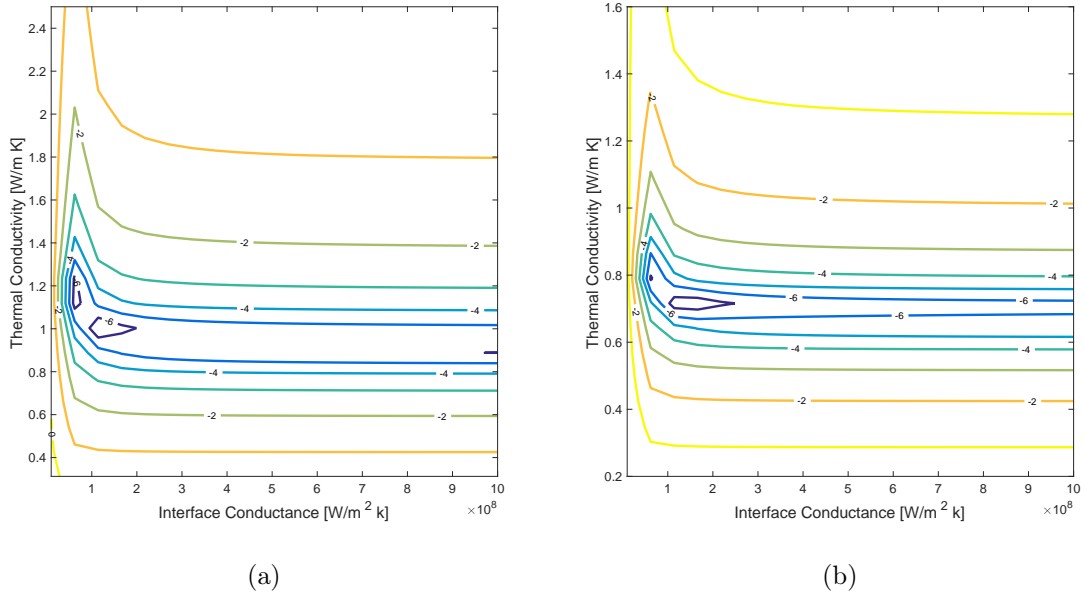


Figure 3-3: Example error landscapes for (a) R-BFO and (b) T-BFO. The contours correspond to iso-error curves defined by taking the logarithm of the residual error between the fit and the experimental data.

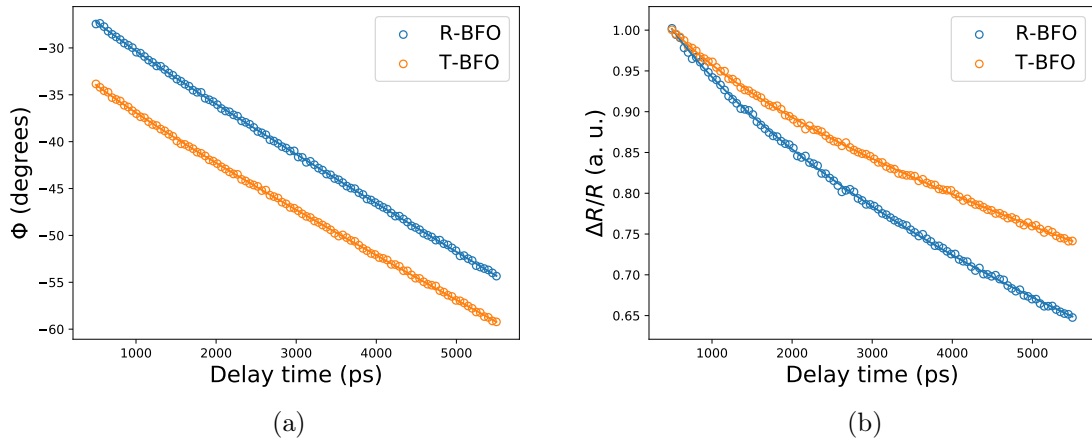


Figure 3-4: Raw TDTR data (circle markers) and best fits (lines) to (a) phase and (b) amplitude representations for R-BFO (blue) and T-BFO (orange).

Comparing the results of BFO/STO and BFO/SRO/LAO grown under the same oxygen pressure, as well as BFO/LAO and BFO/LSMO/LAO, one can observe that the thermal conductivity is independent of the underlayers or substrates. The thermal

Table 3.2: Effect of film thickness on the thermal conductivity of BFO.

Sample	Film Thickness [nm]	Thermal Conductivity [W/mK]
A1: BFO on STO	37.7	$1.29 \pm 0.13$
A2: BFO on STO	29.3	$1.31 \pm 0.13$
A3: BFO on STO	36.1	$1.19 \pm 0.07$
A4: BFO on STO	41.0	$1.26 \pm 0.10$
A5: BFO on STO	56.9	$1.62 \pm 0.12$
B1: BFO on LAO	37.7	$0.84 \pm 0.04$
B2: BFO on LAO	29.3	$0.82 \pm 0.02$
B3: BFO on LAO	36.1	$0.71 \pm 0.18$

Table 3.3: Effect of substrate on the thermal conductivity of BFO.

Sample	Thermal Conductivity [W/mK]
S1: RBFO/SRO/LAO	$1.48 \pm 0.15$
S2: SRO/LAO	$1.32 \pm 0.03$
S3: TBFO/LSMO/LAO	$0.64 \pm 0.06$
S4: LSMO/LAO	$1.53 \pm 0.16$
S5: RBFO/STO	$1.44 \pm 0.26$
S6: TBFO/LAO	$0.50 \pm 0.04$

conductivity is nearly independent of the oxygen pressure for each polymorph despite the varying film strain states. The thermal conductivity is dependent on the crystal structure, with the value of T-like BFO consistently  $\sim 2/3$  that of R-like BFO.

To put the thermal conductivity dependence on structure in perspective, we note that there are more atoms in the T-like BFO unit cell, there are concomitantly more phonon branches in the first Brouilllin zone [82] available to satisfy the scattering selection rules, leading to a reduction of the phonon lifetimes and decrease in the overall thermal conductivity relative to R-like BFO. Furthermore, the distortion of oxygen octahedra caused by the larger  $c/a$  ratio may lead to a much weaker Fe-O bonding along the  $<001>$  direction in T-like BFO. The reduced thermal conductivity of T-like BFO can be also understood as a result of this weaker inter-layer coupling and increased anharmonicity for T-like BFO.

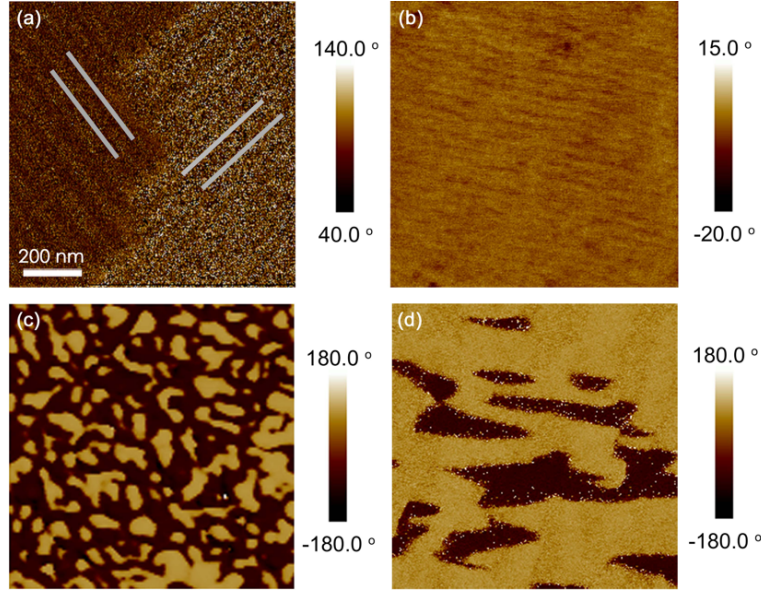


Figure 3-5: Vertical PFM phase images of (a) T-5, (b) T-100, (c) R-5, and (d) R-100. Reproduced from [2] with permission from the American Physical Society.

### Role of ferroelectric domains

The ferroelectric domain features were examined by piezoresponse force microscopy (PFM), which is sensitive to the out-of-plane component of the polarization, on four representative samples: T-like BFO/LSMO/LAO grown at 5 mTorr and 100 mTorr, and R-like BFO/Nb:STO grown at 5 mTorr and 100 mTorr, denoted as T-5, T-100, R-5 and R-100 respectively. The R-like BFO/Nb:STO was used for PFM characterization instead of R-like BFO/SRO/LAO because of the higher surface roughness of the latter.

Figure 3-5 contains representative PFM phase images, where contrast can be seen in all the samples, indicating ferroelectric domains with different out-of-plane components coexist in each sample. A stripe-like domain structure can be seen in both T-like samples, while a qualitatively different mosaic-like domain pattern exists in R-like samples. The domain size, shape and density vary considerably with oxygen pressure during deposition, suggesting that adjusting oxygen pressure during deposition can be an approach to domain engineering in both R- and T-like polymorphs [88]. This may be a result of changes in the surface chemistry during growth at different oxygen pressures in order to achieve charge compensation and maintain the

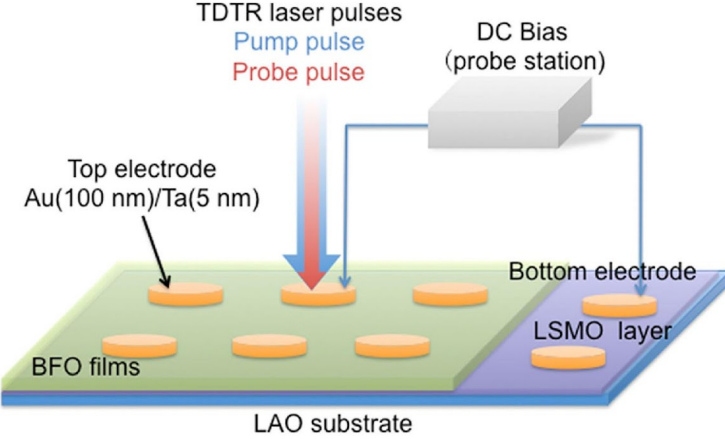


Figure 3-6: Schematic of the in-situ TDTR measurement. Reproduced from [2] with permission from the American Physical Society.

polarization [89, 90], or a consequence of structural relaxation. The micrometers-long stripes in T-100 shown in Figure 3-5 appear to be much narrower than those in T-5 (see Figure 3-5), thus leading to a much higher domain wall density. Meanwhile, both of them exhibit a weak vertical PFM contrast, indicating those domains might have an in-plane polarization component due to a deviation of the ferroelectric axis from the c-axis[91, 92]. As for R-like samples, the domains of R-5 are more random, smaller, and of a higher density than R-100. As suggested by previous work [93], the phase image of R-5 in Figure 3-5 indicates 8 possible domain variants might coexist, resulting in 3 possible polarization angles at the domain walls ( $180^\circ$ ,  $71^\circ$  and  $109^\circ$  boundaries, where the latter two are ferroelastic) which can be charged or neutral. In comparison, the image of R-100 in Figure 3-5 is characteristic of a system with fewer possible domain variants [94] and lower domain wall density.

To investigate the role that domain walls play in determining the thermal conductivity, in-situ TDTR measurements were conducted. The physical layout of the PFM instrument obstructs access to the TDTR laser, so instead the in-situ measurements were accomplished by applying the DC bias through top electrodes during the TDTR measurement as shown schematically in Figure 3-6. A DC bias ranging from 0 to 6/-6 V was determined to be sufficient to polarize both BFO polymorph films based on the hysteresis loops shown in Figure 3-7.

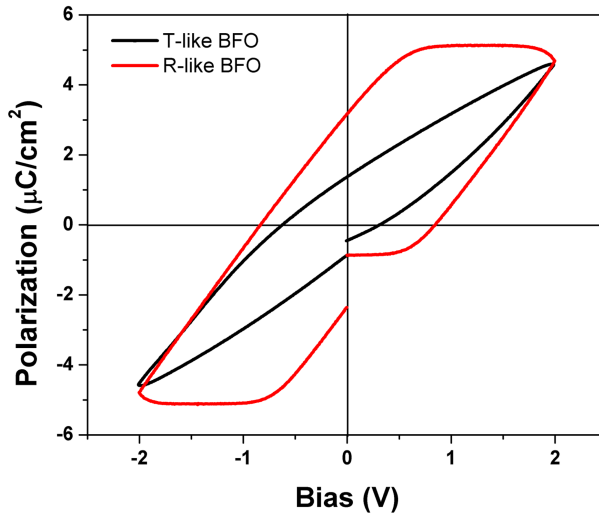


Figure 3-7: Example P-E loop for R and T-like BFO. Reproduced from [2] with permission from the American Physical Society.

Table 3.4: In-situ thermal conductivity of BFO as a function of applied electric field.

Sample	Applied Voltage [V]	Thermal Conductivity [W/mK]
T-like BFO	0	$0.78 \pm 0.06$
T-like BFO	3	$0.74 \pm 0.04$
T-like BFO	6	$0.78 \pm 0.06$
R-like BFO	0	1.02
R-like BFO	3	1.02
R-like BFO	6	0.96
R-like BFO	-3	0.99
R-like BFO	-6	1.01

From the raw TDTR traces collected during the in-situ measurement (examples are shown in Figure 3-8), no dependence on electric field is observed. This is confirmed in the thermal conductivity estimates obtained from the fitting procedure, which are reported in Table 3.4.

Some comments concerning the independence of thermal conductivity on electric field are warranted. To begin, given the thinness of the BFO films, the domain walls are expected to be oriented through the film thickness which is parallel or at a slight angle to the direction of heat flow in the TDTR measurements as shown in Figure 3-9

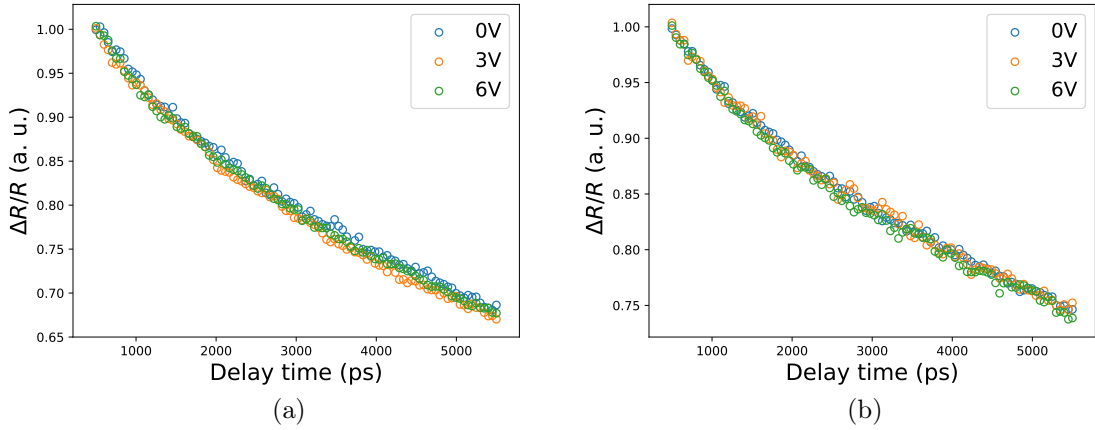


Figure 3-8: Raw TDTR data taken during the in-situ measurement on (a) R-BFO and (b) T-BFO.

so that the domain walls do not act as direct barriers to phonon transport.

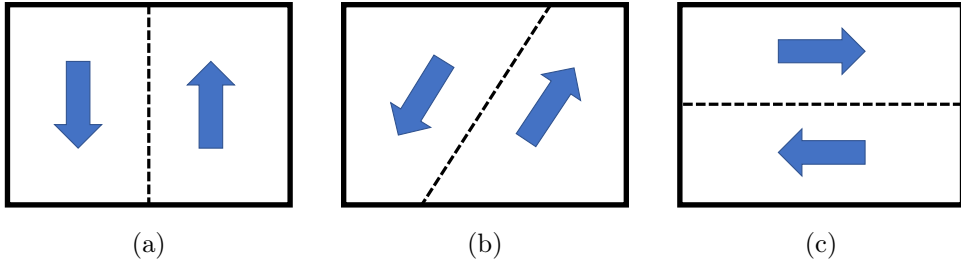


Figure 3-9: Possible ferroelectric domain configurations in BFO thin films. Adapted from [2] with permission from the American Physical Society.

For T-like (001) epitaxial BFO films which are predicted to be polarized out-of-plane, it is possible that the insensitivity of thermal conductivity to domain wall density in the in-situ experiment occurs because polarization changes are accomplished by movement of only the  $180^\circ$  walls which are not ferroelastic and would not be expected to interact strongly with phonons due to the absence of structural distortion.

As for R-like (001) BFO epitaxial films, prior work has shown that an out-of-plane voltage can result in not only the switching of  $180^\circ$  oriented domains (ferroelectric), but also the switching of  $71^\circ$  and  $109^\circ$  oriented domains (ferroelastic) [95, 96, 97]. Detailed PFM mapping uncovered a switching path for R-like BFO in which the out-

of-plane electric field induced  $71^\circ$  switching, and the unstable  $71^\circ$  domains then relax into stable  $180^\circ$  domains at remanence [95]. The complex switching mechanisms in R-like BFO likely produce a distribution over the number of the domain variants. Previous thermal conductivity measurements on R-BFO controlled for the number of domain variants and reported small differences ( $\sim 5\%$ ) in thermal conductivity as a function of the number of domain variants [94].

### 3.2.2 Summary

Two different phases of PLD-grown epitaxial BFO thin films, i.e.: R-like and T-like BFO, were obtained by substrate strain engineering and characterized using PFM and TDTR. The as-grown ferroelectric domain features of each polymorph are quite different: T-like BFO shows a periodic stripe-like domain pattern, while R-like shows a mosaic domain structure. The oxygen pressure has a substantial effect on the ferroelectric domain morphology for each polymorph, providing a convenient method for domain engineering.

There was little difference in thermal conductivity with oxygen pressure suggesting that the domain configuration for either R-like or T-like samples did not greatly influence the thermal conductivity. Further in-situ TDTR analysis, in which the domain state was changed by applying a voltage during the thermal conductivity measurement, also supports the conclusion that domain wall density in the films and geometry studied here has only minor effects on the thermal transport.

However, a dependence of thermal conductivity on the morphotropic phase structure was observed. The thermal conductivity of T-like BFO is about  $2/3$  that of R-like BFO. In comparison with the effects of domain walls in our work, as well as that reported in Ref. [94], the structural dependence of thermal conductivity observed here has a much greater effect, suggesting that the morphotropic phase transformation could be used to control the thermal properties of BFO thin films.

### 3.3 SCO

We chose SCO as the material system of interest due to the “tri-state” phase transitions achieved by incorporating ionic species by ionic liquid gating [98]. In this system the phase transitions are essentially controlled by the amount of oxygen ions and protons in SCO. More specifically, the phase transition from the Brownmillerite phase  $\text{SrCoO}_{2.5}$  (denoted as BM-SCO) to the perovskite phase  $\text{SrCoO}_{3-\delta}$  (denoted as P-SCO,  $\delta$  represents oxygen non-stoichiometry) can be triggered by applying an anodic bias to oxygenate the SCO [99, 100]. Hydrogenating SCO to form the proton ( $\text{H}^+$ ) containing H- $\text{SrCoO}_{2.5}$  (denoted as H-SCO) can be induced by reversing the polarity of the gating voltages to cathodic biases. While  $\text{BM-SCO} \rightarrow \text{P-SCO}$  phase transition is accompanied by a metal-insulator transition [101, 100, 102], the  $\text{BM-SCO} \rightarrow \text{H-SCO}$  transition introduces a further opening of the bandgap in SCO [101]. Considering the distinct chemical compositions, crystal and electronic structures of these three phases (P-SCO, BM-SCO and H-SCO), it is reasonable to expect a significant change in thermal transport. We hypothesized that the defect-free P-SCO phase will have the largest thermal conductivity, since it belongs to the space group with the highest symmetry of the three different phases and it is understood that this relatively increased symmetry consequently imposes a greater number of constraints on the scattering phase space of phonons. On the other hand, the phase transition to H-SCO is expected to decrease thermal conductivity, due to creation of more scattering sites introduced by the intercalated protons and reduced Co cations. TDTR measurements confirmed that the  $\text{BM-SCO} \rightarrow \text{P-SCO}$  phase transition indeed increased the thermal conductivity by more than a factor of 3. This is in contrast to the traditional understanding in which defects only contribute to a reduced thermal conductivity. On the other hand, the  $\text{BM-SCO} \rightarrow \text{H-SCO}$  phase transition decreased the thermal conductivity to  $\sim 30\%$  of its original value. Combining these bidirectional phase transitions triggered in the same device, we achieved a tunable range of more than one order of magnitude in thermal conductivity. We also constructed a solid-state version using ionic gels capable of producing a  $\sim 4$ -fold reversible change

in thermal conductivity.

### 3.3.1 Sample information

The SCO samples were grown and characterized by Qiyang Lu. High quality BM-SCO thin films ( $\sim 44$  nm) on yttria-stabilized zirconia (YSZ) substrates with (100)-orientation. A gadolinia-doped ceria (GDC) buffer layer ( $\sim 10$  nm) was used to bridge the large lattice mismatch between YSZ ( $a/\sqrt{2} = 3.624$  Å) and BM-SCO ( $a = 3.905$  Å). In previous studies, structural and chemical characterization including in situ X-ray absorption spectroscopy (XAS)[99] and X-ray diffraction (XRD)[98] were performed on BM-SCO thin films grown by using the same procedure. Ion intercalation induced phase transition was accomplished using ionic liquid gating with BM-SCO as a working electrode, as shown in Figure 3-10a. 1-hexyl-3-methylimidazolium bis(trifluormethylsulfonyl)imide (HMIM-TFSI) was used as the ionic liquid electrolyte. Electrical biases were applied between BM-SCO thin films and a wound platinum wire as the counter electrode. An anodic bias (oxidizing) applied on BM-SCO is referred to as a positive gate voltage.

Phase transitions in SCO was achieved by intercalating oxygen anions or protons into BM-SCO, by using ionic liquid gating with the BM-SCO film as a working electrode, as shown in Figure 3-10a. BM-SCO was then switched to the oxygenated perovskite phase P-SCO by applying a +3 V gate voltage, or to the hydrogenated phase H-SCO by applying a -4 V gate voltage. The phase transition was confirmed by performing XRD on the switched thin films, as shown in Figure 3-12. The liquid form of the ionic liquid electrolyte can impose constraints in practical device applications and also in some material characterization schemes. Therefore, an ionic gel, instead of an ionic liquid, was used for triggering the ion intercalation and phase transitions as demonstration of a solid-state application of this concept. The ionic gels were fabricated by absorbing the ionic liquid into a block copolymer framework [103]. Figure 3-10b shows a schematic of using an ionic gel for gating. The oxygenation using ionic gels resulted in similar chemical and structural changes to those obtained by using ionic liquid gating, although a lower oxygen stoichiometry in ionic gel gated

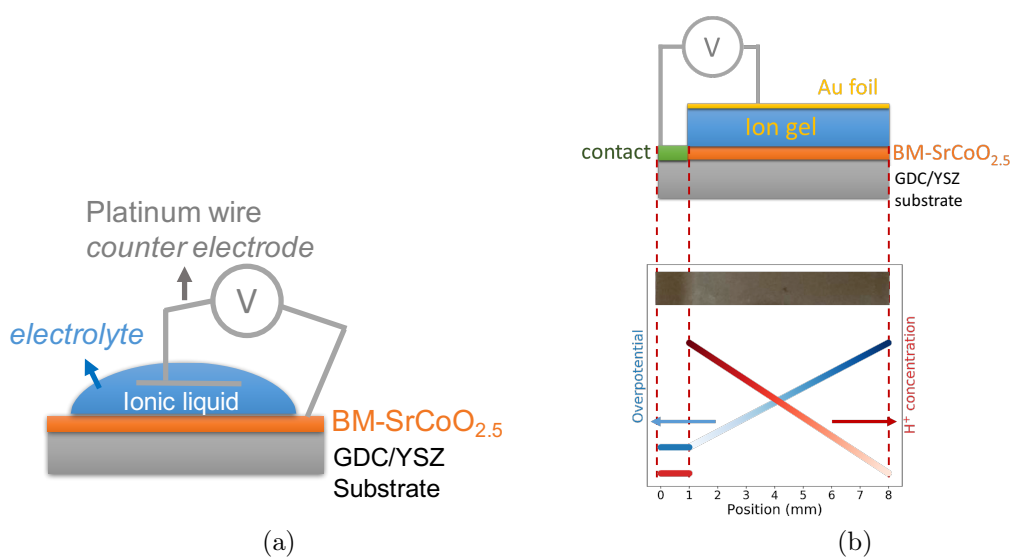


Figure 3-10: (a) Schematic showing the ionic liquid gating of  $\text{SrCoO}_{2.5}$ . (b) Schematic showing the overpotential distribution in the BM-SCO thin film sample before the hydrogenation reaction and the resulting proton concentration gradient. The overpotential decreases with increasing distance away from the contact due to the ohmic loss from the resistance of SCO thin film. The dashed lines matches the position in the overpotential gradient with the positions in the optical picture of the sample. Hydrogenation caused a color change of SCO from brownish to light greyish.

P-SCO was reached (confirmed by XRD, not shown). Hydrogenation using ionic gels enabled the design of a geometry by which a lateral gradient of  $H^+$  concentration in the sample could be obtained, as shown in Figure 3-10b. Since both the BM-SCO and the H-SCO have low electrical conductivity [101], when an electrical bias was applied between the edge of the sample and the top of the ionic gel, the hydrogenation reaction was self-limiting due to the difficulty of current collection with high ohmic losses after forming the insulting H-SCO. Figure 3-10b depicts the estimated overpotential distribution from the contact to the other end of the BM-SCO sample, before forming any H-SCO. The electrochemical driving force decreases gradually starting from the contact region due to the increased ohmic loss from the resistance of the BM-SCO thin film. The end result was a concentration gradient of  $H^+$  from the contact area to the other edge of the thin film sample and a corresponding color gradient was observed in the optical picture of the sample. This concentration gradient was used to study the effect of  $H^+$  concentration on thermal conductivity.

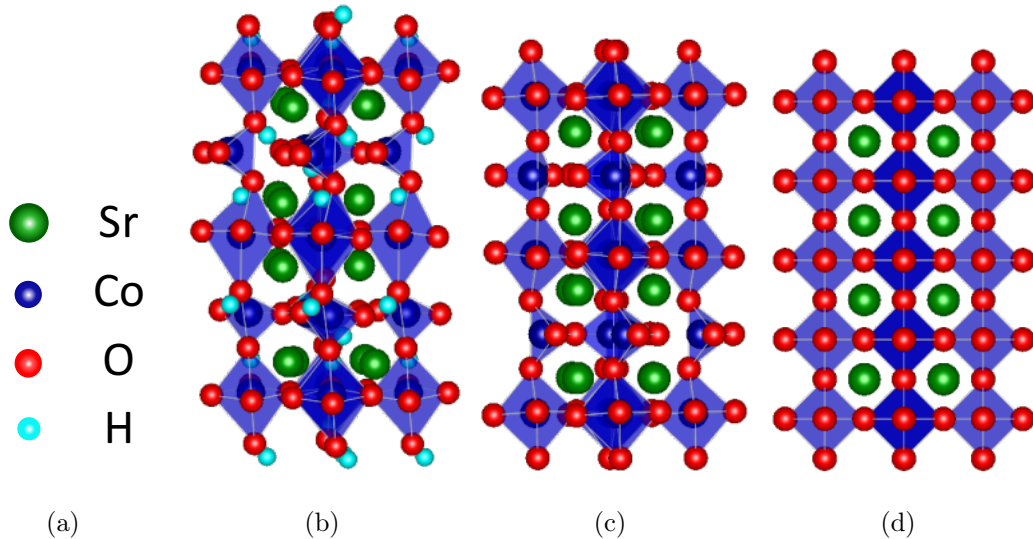


Figure 3-11: (a) Atomic legend for the (b) H-SCO, (c) BM-SCO and (d) P-SCO crystal structures.

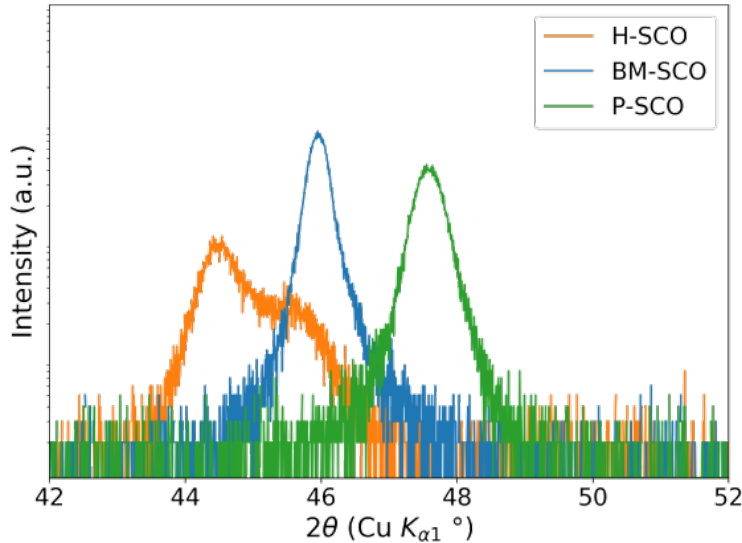


Figure 3-12: X-ray diffraction showing the BM-SCO (008) diffraction peak, hydrogenated  $\text{SrCoO}_{2.5}$  (H-SCO) (008) peak after -4 V ionic liquid gating, and the oxygenated perovskite  $\text{SrCoO}_3$  (P-SCO) after +3 V gating. The shoulder peak in H-SCO at higher  $2\theta$  position is due to the non-switched BM-SCO regions of the sample under the silver electrode used.

### 3.3.2 Thermal conductivity characterization

#### Role of phase

We performed TDTR measurements on BM-SCO, H-SCO and P-SCO to probe the effect of incorporated ionic species and phase transitions on the thermal transport property. Example raw TDTR data is shown in Figure 3-13 and the results of fitting are reported in Table 3.5.

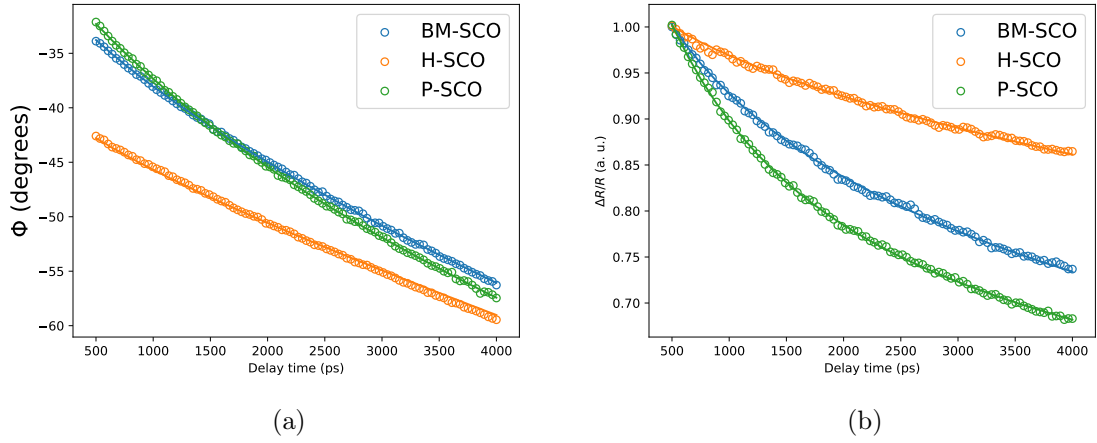


Figure 3-13: Raw TDTR data (circle markers) and best fits (lines) to (a) phase and (b) amplitude representations for H-SCO (orange), BM-SCO (blue) and P-SCO (green). The H-SCO and P-SCO were obtained by gating BM-SCO through ionic liquid gating.

A sensitivity analysis, shown in Figure 3-14, was conducted to ensure sensitivity to the SCO thermal conductivity. As expected, the sensitivity to the SCO thermal conductivity decreases with increasing the thermal conductivity. Nevertheless, the measurement remains sensitive to the SCO thermal conductivity relative to the other thermal model parameters.

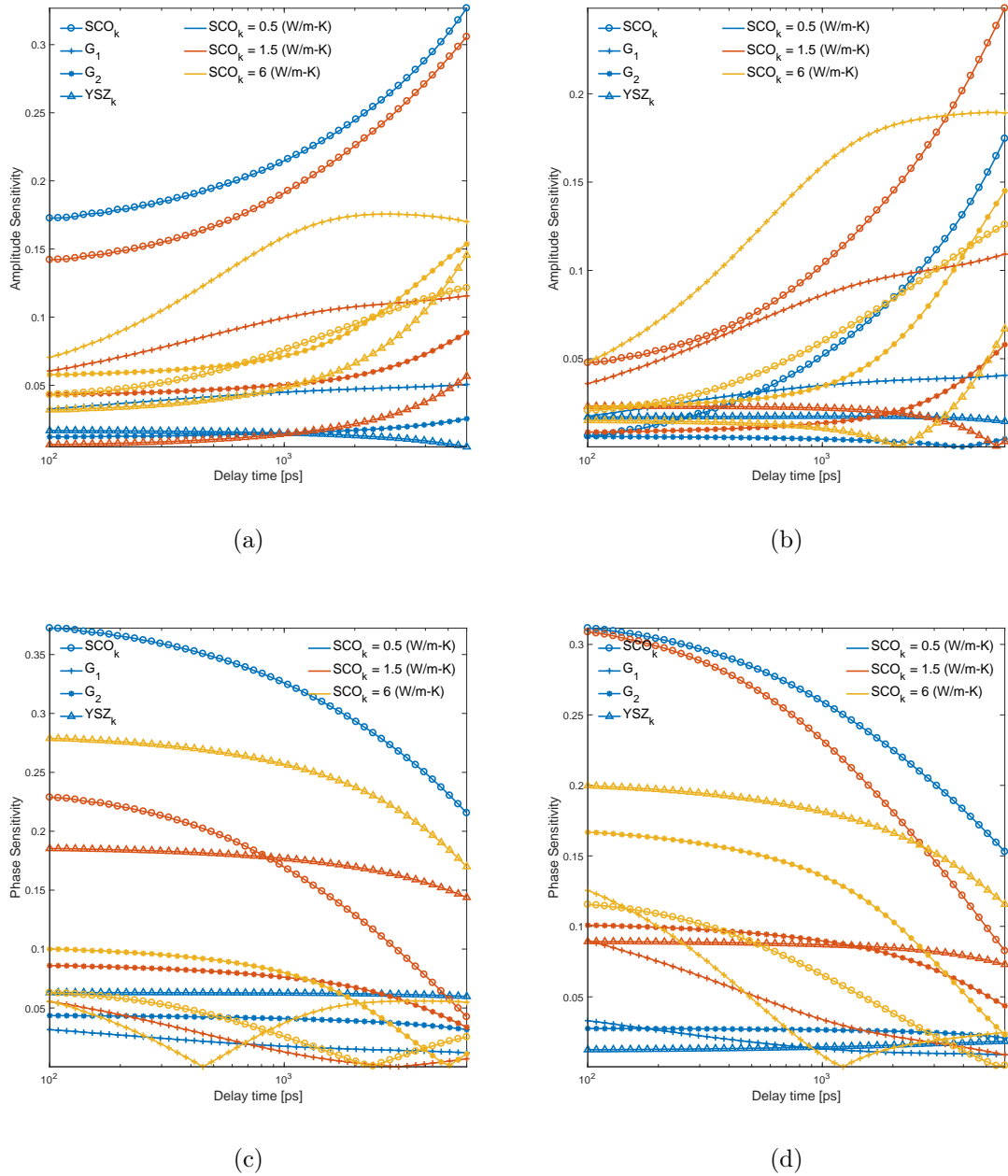


Figure 3-14: Sensitivity analysis for the SCO thin film TDTR measurements where  $\text{SCO}_k$  corresponds to the SCO thermal conductivity,  $G_1$  corresponds to the interface conductance between aluminum and SCO,  $G_2$  corresponds to the interface conductance between SCO and YSZ and  $\text{YSZ}_k$  corresponds to the YSZ substrate thermal conductivity. Subplots correspond to: (a) amplitude sensitivity at 6 MHz, (b) amplitude sensitivity at 12 MHz, (c) phase sensitivity at 6 MHz and (d) phase sensitivity at 12 MHz.

Finally, the error landscape was calculated to ensure uniqueness in the estimates

of the  $G, k$  pairs. Example error landscapes are shown in Figure 3-15, where unique minima are observed.

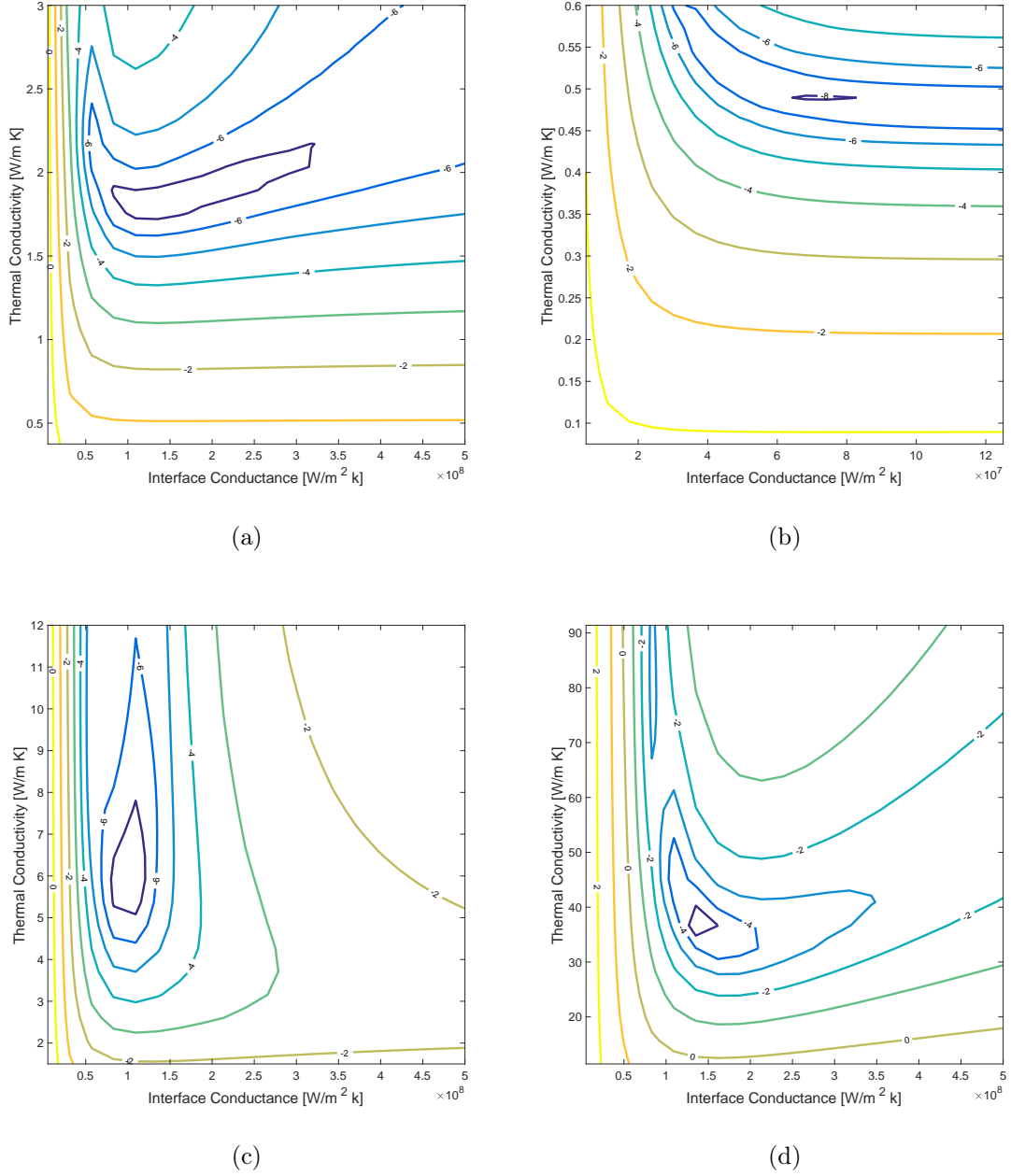


Figure 3-15: Error landscapes for the SCO thin film TDTR measurements. Subplots correspond to (a) BM-SCO, (b) H-SCO, (c) P-SCO and (d) a sapphire reference sample.

A 15-fold range of thermal conductivity modulation by ionic liquid and 4-fold range by ionic gel gating was achieved (see Table 3.5). The electrical resistivity of

Table 3.5: Thermal conductivity of H-SCO, BM-SCO and P-SCO.

Sample	Thermal Conductivity [W/mK]
P-SCO (liquid)	$6.58 \pm 1.71$
BM-SCO	$1.70 \pm 0.027$
H-SCO (liquid)	$0.43 \pm 0.056$
P-SCO (gel)	$2.47 \pm 0.16$
BM-SCO (reversed)	$1.36 \pm 0.063$
H-SCO (gel)	$0.641 \pm 0.086$

the P-SCO phase was measured using the van der Pauw resistance geometry of a Hall effect electronic transport measurement system (Lake Shore 7504), yielding a value of  $5 \times 10^{-2} \Omega\text{-cm}$ . Using this value and the Weidemann-Franz law, one expects a thermal conductivity of  $\sim 0.07 \text{ W}/(\text{m}\cdot\text{K})$ , significantly lower than the measured value. This suggests that phonons, and not electrons, are the dominant thermal carriers in the P-SCO phase. The measured value of  $k$  for P-SCO is comparable with other semiconducting oxide perovskite systems [104]. We have also demonstrated the reversibility of the tuning of thermal conductivity upon switching the sample back to the BM phase from the P-SCO phase. The slightly decreased thermal conductivity compared with the as-prepared BM-SCO samples might be due to additional defects or disordering induced by the switching cycle. This bi-directional tuning of thermal conductivity by simply reversing the polarity and using multiple ion insertions is a novel phenomenon not reported in previous literature. Tunable thermal conductivity can also be obtained by ionic gel gating, albeit the tunable range was smaller compared with ionic liquid gating because of the non-ideal contact between the ionic gel and the film.

### Role of oxygen ions

As defects (isotopic, interstitial, substitutional etc.) are introduced into a perfect crystal, the thermal conductivity is expected to decrease since these defects provide an additional scattering sites experienced by thermal energy carriers [105]. In this sense, the increase of thermal conductivity with electrochemical oxygenation of BM-SCO is surprising. In order to better understand the mechanism behind the increase

in thermal conductivity, additional  $\text{SrCoO}_x$  samples, each with a different oxygen stoichiometry  $x$ , were measured. The controlled tuning of stoichiometry was achieved by applying electrical biases to the SCO thin films on YSZ substrates at 300 °C, since YSZ conducts oxygen ions at elevated temperatures [98]. Upon electrochemical insertion of oxygen into BM-SCO on YSZ at 300 °C, the samples were cooled and their structures and thermal conductivities were measured. We found that applying moderate electrical biases ( $< 2$  V) induced a partial phase transition (Figure 3-16). This finding is consistent with literature reporting that reaching a certain oxygen stoichiometry in SCO is needed in order to complete the BM→P phase transition [98]. The mixtures of BM-SCO and P-SCO (Figure 3-16) were found to have higher thermal conductivities than the as-prepared pure BM-SCO at 0 V. Upon completion of the BM→P transition, the thermal conductivity continued to increase (1 V→2 V). To summarize, when the sample consists of a mixture of the BM-SCO and P-SCO phases (i.e.: incomplete phase transition), the thermal conductivity can be approximated by a rule of mixtures. Once the critical oxygen stoichiometry is reached, the complete phase transition to P-SCO occurs, and the scattering from the oxygen vacancies becomes the dominant mechanism affecting thermal conductivity.

Furthermore, the difference in thermal conductivity between the P-SCO obtained by using ionic liquid or ionic gel as electrolytes (denoted as P-SCO (gel) and P-SCO (liquid), see Table 3.5) can be attributed to a difference in the obtained oxygen non-stoichiometry. XRD and X-ray absorption spectroscopy (XAS) results (not shown) showed that P-SCO (gel) indeed has a larger lattice parameter compared with P-SCO (liq.), indicating a higher oxygen non-stoichiometry level. That is, the P-SCO (gel) is more oxygen deficient ( $\delta$  is greater in  $\text{SrCoO}_{3-\delta}$ ) than the P-SCO (liq.). This higher oxygen defect concentration increases the rate of scattering experienced by the thermal energy carriers, resulting in a lower thermal conductivity of P-SCO (gel).

## Role of hydrogen ions

As previously described, a lateral proton concentration gradient along the SCO sample was created using ionic gel gating, opening the door for the examination of

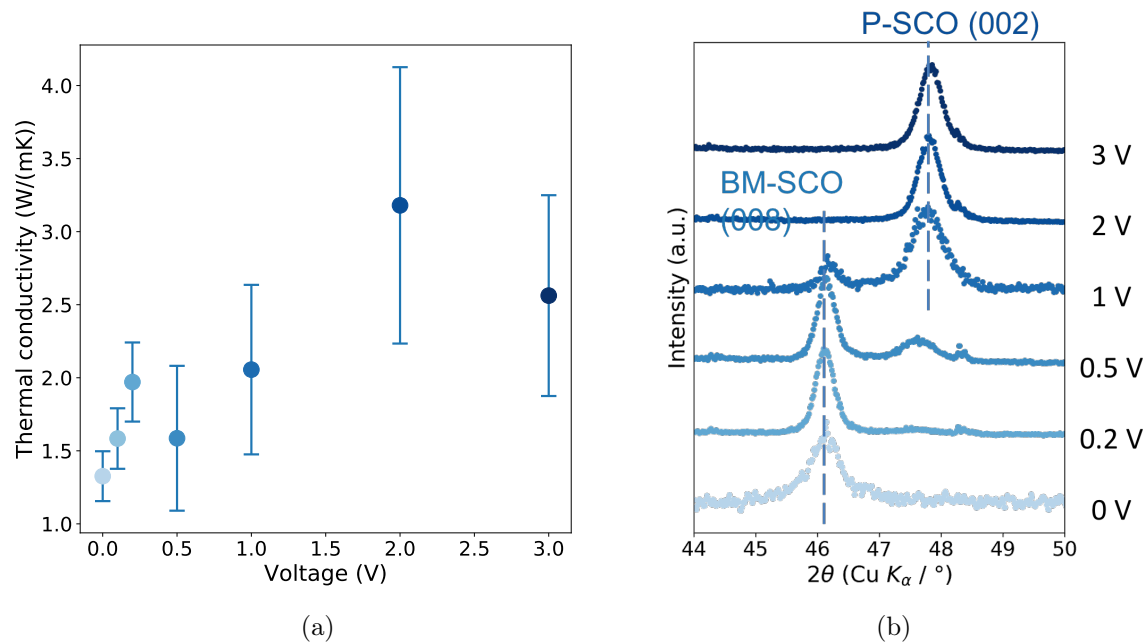


Figure 3-16: (a) Room temperature thermal conductivity of  $\text{SrCoO}_x$  plotted as a function of applied electrical bias (anodic) at 300°C by using YSZ as a solid gating electrolyte. (b) XRD results on  $\text{SrCoO}_x$  upon applying the electrochemical potentials shown in (a). The gradual transition from a mixture of BM-SCO and P-SCO phases to single P-SCO phase was observed.

the role of hydrogen concentration on thermal conductivity. To confirm the presence of a gradient of H<sup>+</sup> along the sample, soft XAS was performed. Example XAS data is shown in Figure 3-17. Details of the XAS analysis can be found in [99]. Briefly, by examining the intensity of the peaks, a correlation between chemical state and hydrogen concentration can be constructed. A relative hydrogen concentration was extracted by taking XAS measurements at different points along the gradient.

The thermal conductivity obtained from TDTR measurements and the H<sup>+</sup> concentration estimated from the XAS spectrum fitting are plotted in Figure 3-17. In contrast to the role played by oxygen in the BM→P-SCO transition, the thermal conductivity decreases with increasing H<sup>+</sup> concentration. Three factors likely contribute in some manner of combination to yield this decrease in thermal conductivity: first, the increase in mass disorder as the H<sup>+</sup> ions occupy interstitial sites in the BM framework [101], second, the displacement of oxygen ions from their equilibrium positions in the BM structure when they bond with protons [101] and third, the ionic size change of Co cations. H<sup>+</sup> insertion into the BM-SCO reduces the Co cations from 3+ to 2+ and this is accompanied by an increase of the Co cation radii. The effect of ionic radius was discussed in previous work on the Pr<sub>0.1</sub>Ce<sub>0.9</sub>O<sub>2- $\delta$</sub>  [70], in which it was shown that the significantly larger size of Pr<sup>3+</sup> compared to Pr<sup>4+</sup>, and the accompanying lattice distortions, were the dominant reason behind a decrease in thermal conductivity upon reducing this oxide (increase in  $\delta$ ). Therefore, it is reasonable to expect a similar effect in H-SCO because of the larger Co<sup>2+</sup> in H-SCO. Importantly, we point out that, if the alloy picture describing thermal conductivity [60] were applicable here, we would obtain a minimum thermal conductivity as a function of H<sup>+</sup> concentration while transitioning from BM-SCO to H-SCO. However, our data, going up to nearly full hydrogenation using the ionic gel and ionic liquid electrolytes, does not present a minimum, but rather a continuous decrease in thermal conductivity between BM-SCO and H-SCO. Theoretical modeling, using tools like molecular dynamics or DFT, combined with experimental characterization techniques, like inelastic neutron scattering, will provide further insight into the mechanisms responsible for the substantial and continuous decrease in thermal conductivity from BM-SCO to H-SCO.

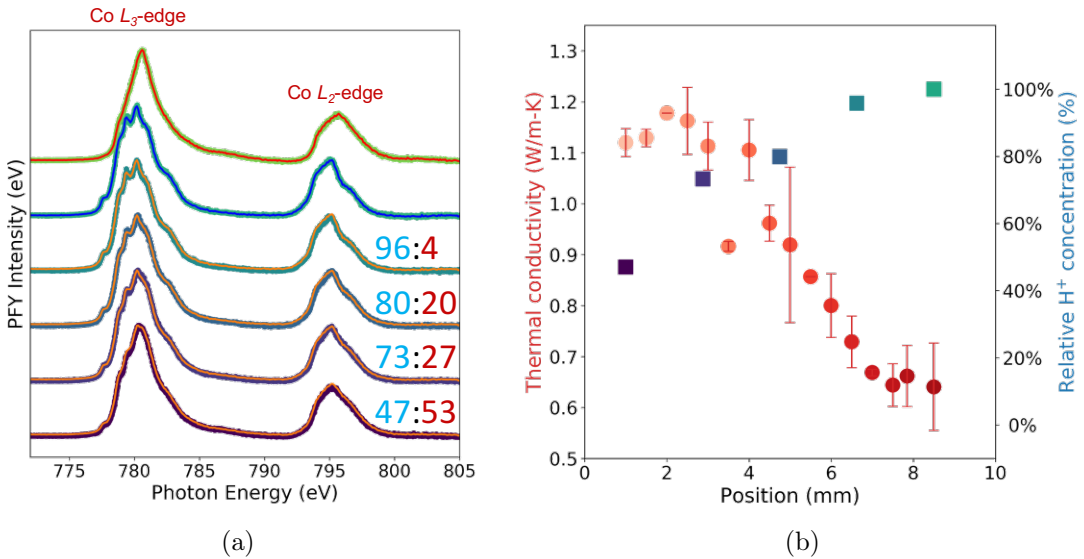


Figure 3-17: The effect of H<sup>+</sup> concentration on the thermal transport property of SCO. (a) Co L<sub>2,3</sub>-edge XAS spectra fitted with linear combinations of spectra measured at spot 1 and 2. The symbols are measured data while the lines are the fitting. (b) Thermal conductivity (in red symbols) of ionic gel hydrogenated SCO measured along the H<sup>+</sup> concentration gradient. In the same plot, the relative H<sup>+</sup> concentrations deduced from the spectra fitting results in (a) were plotted in square symbols, referenced to the spectrum measured at spot 2.

### 3.3.3 Summary

In summary, we demonstrated bi-directional and reversible tuning across one order of magnitude of the thermal conductivity of SCO at room temperature. This large tunable range was obtained by accessing the tri-state phases of SCO electrochemically by applying either a positive bias to insert  $O^{2-}$  and trigger a phase transition to P-SCO, or a negative bias to insert  $H^+$  to obtain the H-SCO phase. By performing the  $O^{2-}$  electrochemical biasing at 300 °C, we uncovered that, at low oxygen stoichiometry, there exists a mixed BM-P SCO phase where the thermal conductivity is effectively an average of the two phases. Once a critical oxygen stoichiometry is reached, the complete BM→P-SCO transition occurs, and thermal conductivity increases with increasing oxygen stoichiometry as a result of increased lattice order and electronic conductivity. We also succeeded in constructing a solid state version of this thermal conductivity manipulation by using ionic gels for triggering the phase transition in SCO. By using ionic gels, a concentration gradient of  $H^+$  was obtained in the SCO thin films, characterized by using synchrotron-based XAS measurements. The  $H^+$  concentration gradient allowed us to correlate the thermal conductivity measured by TDTR and  $H^+$  concentration measured by XAS. The monotonically decreasing thermal conductivity with increasing  $H^+$  concentration suggests that the  $H^+$  themselves as well as the consequent chemical and structural changes play the role as phonon scattering sources. Our larger range of tunable thermal conductivity in oxides, compared with previous studies, provides a new path for designing functional oxides for applications such as smart windows [106], thermal management and energy harvesting [105].

## 3.4 Future work

The work on BFO and SCO sought to elucidate the impact of ferroelectric domains and ionic concentration on thermal conductivity, respectively. Recent preliminary work used TDTR to characterize the impact of strain on the thermal conductivity of  $WO_3$  thin films. The results, reported in Table 3.6, suggest that strain engineering

can be a promising knob for tuning thermal conductivity and will be the focus of future work.

Table 3.6:  $\text{WO}_3$  TDTR measurements

Sample	Substrate	a (Å)	c (Å)	out-of-plane strain	$k$ (W/m-K)
$\text{WO}_3$	LAO	3.788	3.645	-0.033	7.84
$\text{WO}_{2.96}$	LAO	3.791	3.742	-0.007	3.71
$\text{WO}_{2.87}$	LAO	3.764	3.844	0.020	1.52
$\text{WO}_{2.83}$	LAO	3.775	3.854	-0.023	2.46
$\text{WO}_3$	YAO	3.757	3.846	0.021	2.97
$\text{WO}_{2.95}$	YAO	3.752	3.851	0.022	3.26
$\text{WO}_{2.89}$	YAO	3.739	3.851	0.022	3.17
$\text{WO}_3$	STO	3.787	3.649	-0.032	6.61
$\text{H}_x\text{WO}_3$	LAO	3.789	3.745	-0.006	3.37
Liquid Gating					
$\text{H}_y\text{WO}_3$	LAO	3.789	3.699	-0.018	4.14
Liquid Gating					



# Chapter 4

## Size effects in SiGe alloys

### 4.1 Introduction

Deviations from the Fourier regime of thermal transport occur when length scales become on the order of the mean free paths of thermal energy carriers. Geometries where the dimensions of heating or sample size can be shrunk to such a scale have provided experimentalists with a tool for probing size effects in thermal transport. For instance, Hu et al. used nanoscale metal heaters exposed to optical heating in the time domain thermoreflectance (TDTR) configuration to measure size effects in bulk substrates [56] and Cuffe et al. used the transmission mode transient thermal grating (TTG) geometry to study the effect of film thickness in silicon membranes [107].

The nano-heater technique requires careful fabrication and microscopic knowledge of the thermal interface between the heaters and substrate for an accurate description of the transport. The transmission TTG requires optically thin and mechanically free membranes, limiting the range of materials that can be studied. Thus, a technique which overcomes these disadvantages is desirable. First used by Johnson et al. to observe non-diffusive transport in GaAs [108], the reflection mode TTG technique is a simple geometry that is not obfuscated by an interface or limited to thin membranes. The objective of this work is to use a bottom up theoretical approach and apply the framework to the reflection mode TTG. In doing so, we are able to unify the

pictures obtained from the macroscopic observables of experiment to the microscopic properties from theory.

Our candidate material is a silicon-germanium (SiGe) alloy, as this system has proven to be a canonical case for the study of thermal transport in a mass-disordered, yet crystalline system, evidenced by the plethora of work, dating back to the original work by Stohr [109], Toxen [110] and Abeles [111, 60], where it was noted that the mass-disorder scatters short-wavelength phonons consequently shifting the dominant contribution to thermal conductivity to long wavelength phonons.

The concept of large contribution to thermal conductivity from long wavelength phonons with large mean free paths (MFP) was used to explain the observation from Koh et al., who reported a modulation frequency dependent estimate of thermal conductivity under the Fourier model of the experimental geometry of TDTR [112]. The authors suggested that the frequency dependence corresponds to a reduction in the contribution to thermal conductivity of the large MFP phonons. This result led to a series of theoretical explanations [113, 114, 115, 116, 117]. However, each of these explanations invoked a set of fitting parameters to accurately capture the experimental observable.

Inspired by the multiple theoretical attempts to explain the experimental observations, we present theoretical predictions that accurately capture our experimental observables without relying upon fitting parameters or unnecessary approximations. The structure of the paper is as follows. In Section 4.2 we present the phonon properties obtained using density functional theory. In Section 4.2.2, the variational solution to the phonon BTE for the TTG experimental geometry is developed. In Section 4.3, results obtained from TTG are presented and compared with our BTE-based predictions. Finally, we close with a discussion and outlook in Section 4.4.

## 4.2 Theory

### 4.2.1 First Principle Calculations

We follow the general procedure established by Broido [118, 16] and Esfarjani [17], to obtain the phonon properties for SiGe. While the details can be found in these works, an outline of the procedure is included for the sake of completeness.

For a non-alloy system, the harmonic phonon properties are obtained using density-functional perturbation theory (DFPT). The underlying premise is to treat the mechanical displacement corresponding the wavevector of a phonon as a linear perturbation to the electronic Hamiltonian, from which atomic forces can be calculated under the self-consistent criteria of DFT. These forces are then converted into harmonic force constants and used to construct the dynamical matrix for the perturbing wavevector, which can then be diagonalized to obtain the corresponding frequencies. The anharmonic properties can be obtained by extending the perturbation to higher orders [119]. The approach we follow begins with constructing a symmetry-reduced set of atomic displacements in a supercell, where each member of the set undergoes a standard DFT self-consistent calculation, each yielding the force field for the configuration. With this set of force fields, the third order force constants are extracted. Phonon lifetimes are related to the third order force constants through the application of Fermi's golden rule. Integrating the modal thermal conductivity over the Brillouin zone, under the relaxation time approximation to the phonon BTE, yields the lattice thermal conductivity. This full procedure is implemented in the ShengBTE package [43].

To extend the above procedure to a crystalline alloy, approximations are necessary. As discussed by Toxen [110] and Abeles [111], the SiGe alloys are ideal candidates for studying the validity of the VCA. Following Garg et al. [120], we use the VCA to modify the DFT calculations. Within this approximation, two paths can be taken. One can compositionally average the pseudopotentials for the constituent atoms, and then proceed with the usual procedure. Alternatively, one can calculate the harmonic and third order force constants for the unalloyed crystalline versions of the constituent

atoms, take the mass normalized compositional average and then proceed to calculate the phonon properties

$$A_{VCA} = x A^{Si} + (1 - x) A^{Ge} \quad (4.1)$$

where  $x$  is the percent composition of silicon and  $A^i$  is a placeholder for the harmonic force constants, the third order force constants, the atomic masses and the lattice constants [121] of the constituent atoms. We have followed both VCA procedures, and find negligible difference in the phonon properties (see Appendix B).

The penultimate step in the alloy calculation is to include the effect of mass disorder. Again, following Garg's work, the phonon lifetimes are modified under Matthiessen's rule using the theory established by Tamura [63] to treat isotope scattering as an elastic perturbation. Garg et al. went a step further to estimate the anharmonic shifts due to disorder through supercell calculations. Feng et al. used molecular dynamics to show that the application of Matthiessen's rule leads to an overestimation of thermal conductivity by more than  $\sim 20\%$  in SiGe due to neglecting four and five-phonon processes [122]. Our experimental results will show that the harmonic mass disorder approximation under Matthiessen's rule produces reasonable theoretical predictions. We note that the procedure followed in this work will not capture the frequency shifts that can be observed in the SiGe Raman spectra [123, 124] (see Appendix B). It is expected that these Raman active modes do not significantly contribute to thermal conductivity, as their group velocities are small and their lifetimes have been reduced by mass disorder scattering. The phonon properties are reported in Figure 4-1. The DFT calculation parameters used in this Chapter are the following: for the DFPT portion, a  $16 \times 16 \times 16$  Monkhorst-Pack  $k$  mesh with a kinetic energy cutoff of 50 Ry and a convergence criteria of 1E-12 Ry is used. For the supercell calculations, a  $4 \times 4 \times 4$  supercell was used such that third order force constants up to the fifth nearest neighbor could be obtained and only wavefunctions at the gamma point were calculated. Both (Si,Ge).pz-bhs.UPF and (Si,Ge).pz-nnc.UPF pseudopotentials were tested yielding a negligible difference between thermal

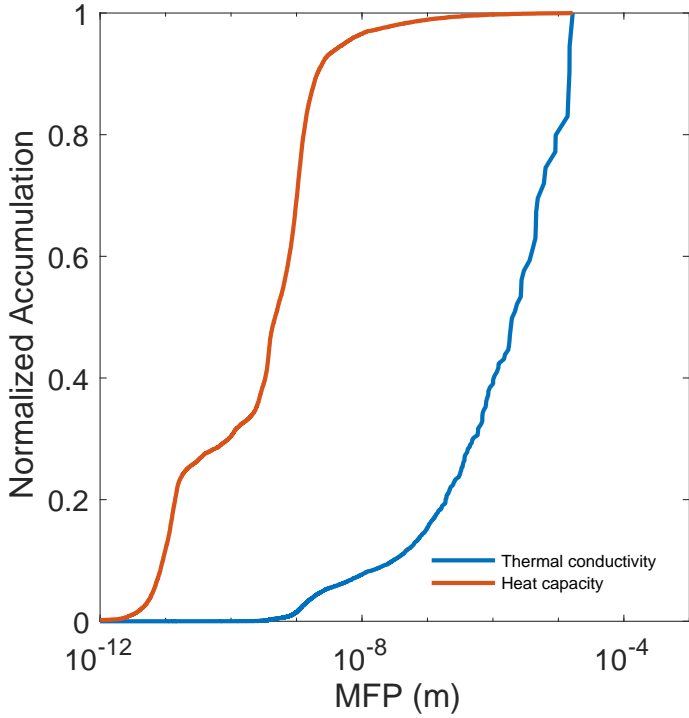


Figure 4-1:  $\text{Si}_{93.4}\text{Ge}_{6.6}$  MFP accumulation of thermal conductivity and heat capacity at 300 K. Reproduced from [1] with permission from the American Physical Society.

conductivity estimates. The DFPT calculations were done with a  $6 \times 6 \times 6 q$  mesh. Interpolation was done on a  $48 \times 48 \times 48 q$  mesh with a Gaussian smearing parameter of 0.1 for the Kronecker delta approximation to yield convergence of the thermal conductivity. All calculations were done with the quantum-ESPRESSO package [125].

#### 4.2.2 Solving the Boltzmann Transport Equation

Given the bulk phonon properties of  $\text{Si}_{93.4}\text{Ge}_{6.6}$ , we now turn to the study of the effect of grating period length on thermal transport in the reflection mode TTG geometry. The diffusive temperature profile has previously been obtained in order to analyze the temperature signal using TTG for opaque materials [58]. For the experimental conditions of a spatially periodic heat source defined by wavevector  $q = \frac{2\pi}{\lambda}$ , the temperature is given by  $T(x, z, t) = T_0 + T_0 e^{iqx} h(z, t)$  in complex form, and this serves as a definition of the non-dimensional temperature  $h$ . The temperature  $T_0$  is the background equilibrium temperature of the system, for example the room tem-

perature. The heating by the laser is incorporated with a volumetric heat generation term, given by the functional form

$$Q = \delta(t) e^{iqx} U_0 \beta e^{-\beta z} \quad (4.2)$$

where  $U_0$  represents the energy per unit area deposited into the substrate by the pulse, and  $\beta$  is the inverse penetration depth of the heating profile. The derivation found in [58] takes into consideration different in-plane and cross-plane thermal conductivities, however the experimental signal is mostly sensitive to the in-plane thermal conductivity. For simplicity, we show the derivation for an isotropic system, where the Fourier heat conduction equation simplifies to

$$\frac{\partial h}{\partial t} = -\alpha q^2 h + \alpha \frac{\partial^2 h}{\partial z^2} + \frac{\beta U_0}{CT_0} e^{-\beta z} \delta(t) \quad (4.3)$$

with the initial and boundary conditions given by

$$\begin{aligned} h(z, t = 0^-) &= 0 \\ \frac{\partial h}{\partial z} \Big|_{z=0} &= 0 \\ h(z \rightarrow \infty, t) &= 0 \end{aligned} \quad (4.4)$$

which assumes an adiabatic surface at  $z = 0$ , and that the system starts at equilibrium prior to the energy deposited by the laser. We present the solution in the Laplace transformed domain for convenience

$$\hat{h}(z, s) = \frac{\frac{\beta U_0}{CT_0}}{s + \alpha(q^2 - \beta^2)} \left( e^{-\beta z} - \frac{\beta}{\sqrt{q^2 + \frac{s}{a}}} e^{-z\sqrt{q^2 + \frac{s}{a}}} \right). \quad (4.5)$$

We intend to utilize this Fourier heat conduction temperature profile in our variational solution of the BTE. Taking the inverse Laplace transform of this yields the temperature as a function of the depth into the substrate and time

$$h(z, t) = \frac{\beta U_0}{2CT_0} e^{-\alpha t(q^2 - \beta^2)} \left( e^{\beta z} \operatorname{erfc}(\beta \sqrt{\alpha t} + \frac{z}{2\sqrt{\alpha t}}) + e^{-\beta z} \operatorname{erfc}(\beta \sqrt{\alpha t} - \frac{z}{2\sqrt{\alpha t}}) \right) \quad (4.6)$$

where the surface temperature is

$$h(z = 0, t) = \frac{\beta U_0}{CT_0} e^{-\alpha t(q^2 - \beta^2)} \operatorname{erfc}(\beta \sqrt{\alpha t}). \quad (4.7)$$

### Temperature integral equation

We begin with the spectral Boltzmann transport equation under the relaxation time approximation (RTA)

$$\frac{\partial g_\omega}{\partial t} + \mathbf{v}_\omega \cdot \nabla g_\omega = \frac{g_0 - g_\omega}{\tau_\omega} + \frac{Q_\omega}{4\pi} \quad (4.8)$$

where  $g_\omega$  is the phonon energy density per unit frequency interval per unit solid angle above the reference background energy, related to the distribution function as  $g_\omega = \frac{\hbar\omega D(\omega)}{4\pi}(f_\omega - f_0(T_0))$ .  $\mathbf{v}_\omega$  is the group velocity,  $\tau_\omega$  is the relaxation time, and  $g_0$  is the equilibrium energy density, given by  $g_0 \approx \frac{1}{4\pi} C_\omega (T - T_0)$  in the linear response regime. The sinusoidal heating profile in the  $x$ -direction (in-plane), given by the pulse form  $Q_\omega(x, z, t) = \delta(t) e^{iqx} \tilde{Q}_\omega(z)$ , means we can expect that the spectral and equilibrium energy densities to also obey a sinusoidal profile  $g_\omega = e^{iqx} \tilde{g}_\omega$  and the equilibrium distribution will simplify accordingly to  $\tilde{g}_0 = \frac{C_\omega T_0}{4\pi} h(z, t)$ . By inputting this in-plane sinusoidal profile and utilizing the Laplace transform (denoted by the  $\hat{\cdot}$  symbol) in the time domain, the BTE simplifies to

$$\frac{\partial \hat{\tilde{g}}_\omega}{\partial z} + \hat{\tilde{g}}_\omega \frac{1 + s\tau_\omega + i\eta_\omega \mu_x}{\Lambda_\omega \mu_z} = \frac{\hat{\tilde{g}}_0 + \tau_\omega \frac{Q_\omega}{4\pi}}{\Lambda_\omega \mu_z} \quad (4.9)$$

where we have defined  $\eta_\omega = q\Lambda_\omega$ . For convenience, we define the parameter  $V = \frac{1 + s\tau_\omega + i\eta_\omega \mu_x}{\Lambda_\omega \mu_z}$  to group the variables in a compact form for the following solution of the BTE

$$\hat{\tilde{g}}_\omega(z, s, \mu_x, \mu_z) = e^{-Vz} \hat{\tilde{g}}_\omega(z=0, s, \mu_x, \mu_z) + \int_0^z dz' e^{-V(z-z')} \frac{\hat{\tilde{g}}_0(z', s) + \tau_\omega \frac{\tilde{Q}_\omega}{4\pi}}{\Lambda_\omega \mu_z}. \quad (4.10)$$

The boundary conditions are taken to be

$$\begin{aligned} \hat{\tilde{g}}_\omega(z=L, s, \mu_x, \mu_z < 0) &= 0 \\ \hat{\tilde{g}}_\omega(z=0, s, \mu_x, \mu_z > 0) &= \sigma. \end{aligned} \quad (4.11)$$

The first boundary condition takes an imaginary blackbody wall at length  $L$  into the substrate at the background temperature to account for the semi-infinite substrate, where this length approaches infinity. The second boundary condition provides the adiabatic boundary condition with diffuse scattering, where  $\sigma = \frac{1}{\pi} \int d\Omega \Theta(\mu_z) \mu_z \hat{\tilde{g}}_\omega(z=0, s, \mu_x, -\mu_z)$ , which is proportional to the specular heat flux approaching the surface. We have utilized the Heaviside step function to reduce the integration over the solid angle only to consider phonons approaching the surface. Applying the boundary conditions, and taking the artificial length  $L$  to infinity yields the formal solution to the BTE for the spectral energy density in terms of the equilibrium energy density

$$\begin{aligned} \hat{\tilde{g}}_\omega(z, s, \mu_x, \mu_z) &= -\Theta(-\mu_z) \int_z^\infty e^{-V(z-z')} \frac{\hat{\tilde{g}}_0(z', s) + \tau_\omega \frac{\tilde{Q}_\omega}{4\pi}}{\Lambda_\omega \mu_z} \\ &\quad + \Theta(\mu_z) \left( \int_0^z e^{-V(z-z')} \frac{\hat{\tilde{g}}_0(z', s) + \tau_\omega \frac{\tilde{Q}_\omega}{4\pi}}{\Lambda_\omega \mu_z} \right. \\ &\quad \left. + \int_0^\infty 2e^{-V(z)} F_2(z') \frac{\hat{\tilde{g}}_0(z', s) + \tau_\omega \frac{\tilde{Q}_\omega}{4\pi}}{\Lambda_\omega} \right) \end{aligned} \quad (4.12)$$

where we have defined the following solid angle integral function

$$F_n(z) = \frac{1}{2\pi} \int d\Omega \Theta(\mu_z) \mu_z^{n-2} (e)^{-Vz}. \quad (4.13)$$

The first term represents phonons moving towards the surface of heating at  $z=0$ ,

whereas the second term represents phonons moving away from the surface.

The temperature can be derived by utilizing the equilibrium condition obtained by integrating Eq. 4.12 with respect to frequency and the solid angle [8]. The equilibrium condition in this case can be expressed as

$$4\pi \int d\omega \frac{1}{\tau_\omega} \hat{g}_0(z, s) = \int d\omega \frac{1}{\tau_\omega} \int d\Omega \hat{g}_\omega(z, s, \mu_x, \mu_z). \quad (4.14)$$

Performing the solid angle integral, and inputting the expression for the non-dimensional temperature expression  $\hat{g}_0 = \frac{C_\omega T_0}{4\pi} \hat{h}(z, s)$ , we obtain the integral equation for the temperature distribution

$$\begin{aligned} \hat{h}(z, s) \int d\omega \frac{C_\omega}{\tau_\omega} &= \int d\omega \frac{C_\omega}{2\Lambda_\omega \tau_\omega} \int_0^\infty dz' (\hat{h}(z', s) + \frac{\tau_\omega \tilde{Q}_\omega(z')}{C_\omega T_0} (F_1(|z - z'|) \\ &\quad + 2F_2(z)F_2(z'))). \end{aligned} \quad (4.15)$$

This is an integral equation in the spatial variable  $z$  for the non-dimensional temperature in the Laplace domain, which after solving, requires an inverse Laplace transform in order to obtain the full temperature solution in the time domain. For the thermal distribution, the spectral heat generation takes the form

$$\tilde{Q}_\omega(z) = \frac{C_\omega}{C} U_0 \beta e^{-\beta z}. \quad (4.16)$$

Note that  $\frac{C_\omega}{C}$  is a weighting of the contribution of a given mode to heat generation under the assumption of thermalized distribution [126]. While other distributions can be taken, we utilize this form in order to compare to the Fourier heat conduction solution.

## Variational solution

Eq. 4.15 can be numerically solved using finite difference methods [13] or Monte Carlo methods [53, 54]. In this work, we extend a variational approach previously presented for the 1D TTG [3] and thin film TTG geometries [127] to the reflection

mode TTG geometry. The starting point of this approach is to select a trial function. The simplest trial function is to take the diffusive temperature profile and allow just the thermal diffusivity to be a variational parameter. In general, the size effects exhibited by the BTE will affect both the temporal as well as the spatial distributions of the temperature. However, the simple variational solution that varies only one parameter, the thermal diffusivity, performs well by approximately solving for the thermal decay from the BTE over a broad range of grating period length scales. We proceed by taking the Fourier heat conduction solution of Eq. 4.5 as a trial function and use the thermal diffusivity as the variational parameter.

To solve for the variational parameter, we can utilize mathematical optimization methods such as least squares on the error residual of the temperature equation [3], or impose a physical condition that we wish the trial function to satisfy. Here, we impose that the trial function must satisfy energy conservation taken over the control volume of the semi-infinite substrate over all time, analogous to the condition utilized for the thin film TTG geometry [127]. This mathematical condition can be obtained by integrating the BTE of Eq. 4.14 over the solid angle and frequency, and then also over the depth variable  $z$  as well as over all time to yield

$$U_0 \frac{\lambda}{\pi} = 2i \int_0^\infty dz \int_0^\infty dt \tilde{q}_x(z, t). \quad (4.17)$$

This statement says that the total energy per unit area perpendicular to the  $z$ -axis deposited in the semi-infinite substrate initially (left hand side of Eq. 4.16) must be equal to the total energy that moves away in the in-plane direction. The in-plane heat flux is obtained by utilizing the spectral energy density of Eq. 4.12, and integrating over the frequency and solid angle  $\hat{q}_x(z, s) = \int d\omega \int d\Omega \Theta v_\omega \mu_x \hat{g}_\omega(z, s, \mu_x, \mu_z)$  to obtain the in-plane heat flux

$$\hat{q}_x(z, s) = \frac{T_0}{2} \int d\omega \frac{C_\omega v_\omega}{\Lambda_\omega} \int_0^\infty dz' \left( \hat{h}(z', s) + \frac{\tau_\omega \tilde{Q}_\omega(z')}{C_\omega T_0} \right) (G_1(|z - z'|) + 2G_2(z)F_2(z')) \quad (4.18)$$

where we have defined the solid angle integral function

$$G_n(z) = \frac{1}{2\pi} \int d\Omega \Theta(\mu_z) \mu_z^{n-2} \mu_x(e)^{-Vz}. \quad (4.19)$$

Inserting the heat flux expression of Eq. 4.18 into the energy conservation statement of Eq. 4.17, and inputting the variational trial function of the Fourier heat conduction solution of Eq. 4.5 as well as the thermal distribution for the heat generation rate, we can solve for the effective thermal conductivity after cleaning up some of the solid angle integrals. We obtain a form similar in structure to the results from the thin film TTG [127] and the one-dimensional limit of the TTG [3]

$$k = \frac{\frac{1}{3} \int d\omega C_\omega v_\omega \Lambda_\omega f(\eta_\omega, \text{Kn}_\omega)}{\frac{1}{C} \int d\omega C_\omega g(\eta_\omega, \text{Kn}_\omega)} \quad (4.20)$$

where  $\text{Kn}_\omega = \Lambda_\omega \beta$ . Note that information concerning the spectral contribution to heat capacity is needed in the equation for effective thermal conductivity [128].  $f$  and  $g$  are the kernels that weigh a given mode's contribution to effective thermal conductivity under the imposed size effects, explicitly given as

$$\begin{aligned} f(\eta_\omega, \text{Kn}_\omega) &= \frac{3}{\eta_\omega^2} \left( 1 - \frac{1}{\eta_\omega} \arctan(\eta_\omega) + \frac{\eta_\omega^2 \Psi(\eta_\omega, \text{Kn}_\omega) - \text{Kn}_\omega^2 \Psi(\eta_\omega, \text{Kn}_\omega)}{\eta_\omega^2 - \text{Kn}_\omega^2} \right) \\ g(\eta_\omega, \text{Kn}_\omega) &= \frac{1}{\eta_\omega} \arctan(\eta_\omega) + \Psi(\eta_\omega, \text{Kn}_\omega). \end{aligned} \quad (4.21)$$

We have defined the following solid angle integral functions

$$\begin{aligned} \Psi(x, z) &= \frac{1}{2} \psi_1(x, z) - \frac{1}{1 + \sqrt{1 + x^2}} \psi_0(x, z) \\ \psi_n(x, z) &= \frac{1}{2\pi} \int d\Omega \Theta(\mu_z) \frac{z \mu_z}{(1 + ix\mu_x)^n (1 + z\mu_z + ix\mu_x)}. \end{aligned} \quad (4.22)$$

If we take the limit of  $\text{Kn}_\omega \rightarrow 0$ , i.e. the case of very long penetration depth, the solid angle integrals vanish as  $\psi_n(\eta_\omega, \text{Kn}_\omega \rightarrow 0) \propto \text{Kn}_\omega$ , and we recover the one-dimensional TTG limit described by the previously derived effective thermal con-

ductivity [3]. The more interesting case for this problem is the reduction to surface heating, i.e.  $\text{Kn}_\omega \rightarrow \infty$ . In this case, the kernel functions simplify to

$$\begin{aligned} f(\eta_\omega, \text{Kn}_\omega \rightarrow \infty) &= \frac{3}{2\eta_\omega^2} \left( 1 - \frac{1}{\eta_\omega} \arctan(\eta_\omega) \right) \\ &\quad - \frac{1}{\eta_\omega^3(1 + \sqrt{1 + \eta_\omega^2})} \left( (1 + \eta_\omega)^{\frac{3}{2}} - \frac{3}{2}\eta_\omega^2 - \eta_\omega^3 - 1 \right) \quad (4.23) \\ g(\eta_\omega, \text{Kn}_\omega \rightarrow \infty) &= \frac{1}{2\eta_\omega} \arctan(\eta_\omega) + \frac{1}{1 + \sqrt{1 + \eta_\omega^2}}. \end{aligned}$$

For the general case of arbitrary penetration depth, the solid angle integral functions can be calculated analytically, which allows for a fully analytical effective thermal conductivity for any penetration depth into the substrate

$$\psi_0(x, z) = \begin{cases} z \frac{1+z-\sqrt{1+x^2}}{z^2-x^2} + \frac{z^2}{(x^2-z^2)^{\frac{3}{2}}} \\ [\arctan(\sqrt{x^2-z^2}) + \arctan(\frac{1}{z}\sqrt{x^2-z^2})] \\ -\arctan(\frac{1}{z}\sqrt{1+x^2}\sqrt{x^2-z^2})], & \text{if } z < x \\ \frac{(1+x^2)^{\frac{3}{2}}-x-1}{3x}, & \text{if } z = x \\ z \frac{1+z-\sqrt{1+x^2}}{z^2-x^2} + \frac{z^2}{(z^2-x^2)^{\frac{3}{2}}} \ln \left( \frac{1+\frac{1}{z}\sqrt{1+x^2}\sqrt{z^2-x^2}}{(1+\sqrt{z^2-x^2})(1+\frac{1}{z}\sqrt{z^2-x^2})} \right), & \text{if } z > x \end{cases}$$

$$\psi_1(x, z) = \begin{cases} \frac{1}{x} \arctan(x) - \frac{1}{\sqrt{x^2-z^2}} \\ [\arctan(\sqrt{x^2-z^2}) + \arctan(\frac{1}{z}\sqrt{x^2-z^2})] \\ -\arctan(\frac{1}{z}\sqrt{1+x^2}\sqrt{x^2-z^2})], & \text{if } z < x \\ \frac{1}{x} \arctan(x) - 1 + \frac{x}{1+\sqrt{1+x^2}}, & \text{if } z = x \\ \frac{1}{x} \arctan(x) + \frac{1}{\sqrt{z^2-x^2}} \ln \left( \frac{1+\frac{1}{z}\sqrt{1+x^2}\sqrt{z^2-x^2}}{(1+\sqrt{z^2-x^2})(1+\frac{1}{z}\sqrt{z^2-x^2})} \right), & \text{if } z > x. \end{cases}$$

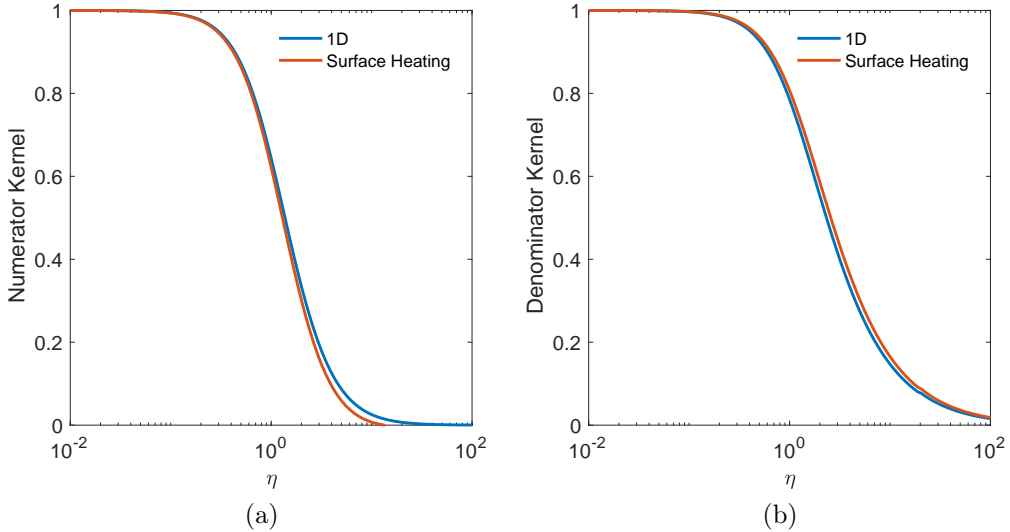


Figure 4-2: Kernels of the effective conductivity in Eq. 4.20. (a) The numerator kernel  $f$  that shows the size effects and appears beside the differential conductivity and (b) the denominator kernel  $g$  that shows the size effects and appears beside the spectral heat capacity. Reproduced from [1] with permission from the American Physical Society.

### Comparison between the Variational Solution and Monte Carlo Simulations

To study the effect of the optical penetration depth in the case of a diffuse surface boundary condition, we first plot the kernels  $f$  and  $g$  as a function of  $\eta$  for the extremal limits of  $\text{Kn}_\omega$ . The one-dimensional limit of  $\text{Kn}_\omega \rightarrow 0$  and the surface heating limit of  $\text{Kn}_\omega \rightarrow \infty$  define the envelope of curves for which the kernels for arbitrary values of the penetration depth must lie between. As the Knudsen number increases, the size effect due to the optical penetration depth increases, which physically results in a decrease of the effective thermal conductivity. This occurs due to the decrease in the numerator kernel  $f$ , and the increase of the denominator kernel  $g$ . However, the variational solution produces a one-dimensional limit and the surface heating limit that are practically indistinguishable (Figure 4-2), suggesting that the effective thermal conductivity due to a diffuse boundary experiences weak effects from the optical penetration depth.

Utilizing the derived kernels to calculate the effective thermal conductivity for

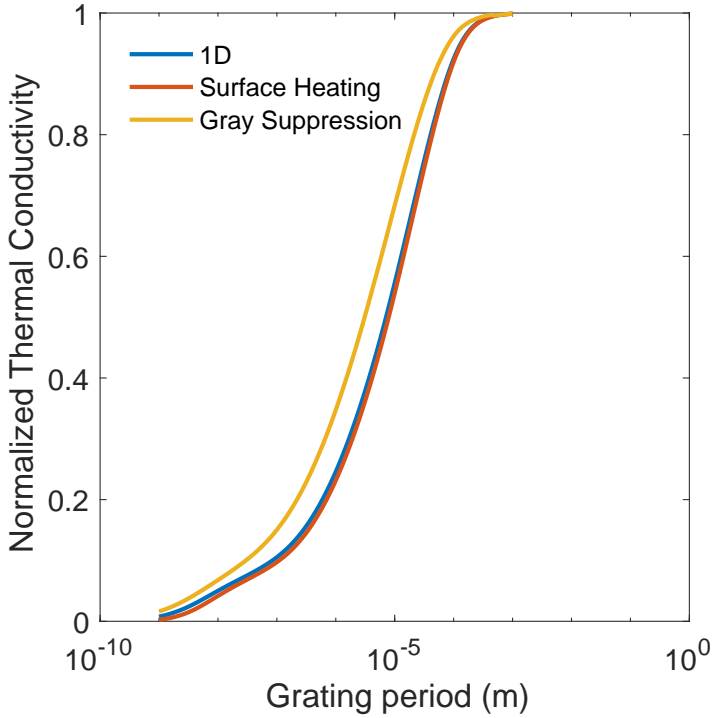


Figure 4-3: Effective thermal conductivity for  $\text{Si}_{93.4}\text{Ge}_{6.6}$  in the one-dimensional limit and the surface heating limit. The effective thermal conductivity using the gray suppression function for one-dimensional TTG (Eq. 4.24) is also shown [3]. Reproduced from [1] with permission from the American Physical Society.

$\text{Si}_{93.4}\text{Ge}_{6.6}$ , we show in Figure 4-3 the effective thermal conductivity in the various limits. Note that the effective thermal conductivity is quite similar in the one-dimensional limit and in the surface heating limit. As expected, when the thermal grating period is much smaller than the optical penetration depth, the effective thermal conductivity takes on values of the one-dimensional limit, as the transport is mostly in-plane. In the opposite case, when the grating period is much larger than the optical penetration depth, the effective thermal conductivity approaches the surface heating limit.

Figure 4-3 demonstrates that the variational technique predicts that transport has a weak dependence on the optical penetration depth, a consequence of the kernels' weak dependence on optical penetration depth. In the limit of  $q/\beta \gg 1$ , the one dimensional TTG is recovered. In the limit of  $q/\beta \ll 1$ , the modified Fourier approach fails to capture the short time behavior. In this regime, the use of effective thermal conductivity (obtained either using the variational approach or otherwise) is

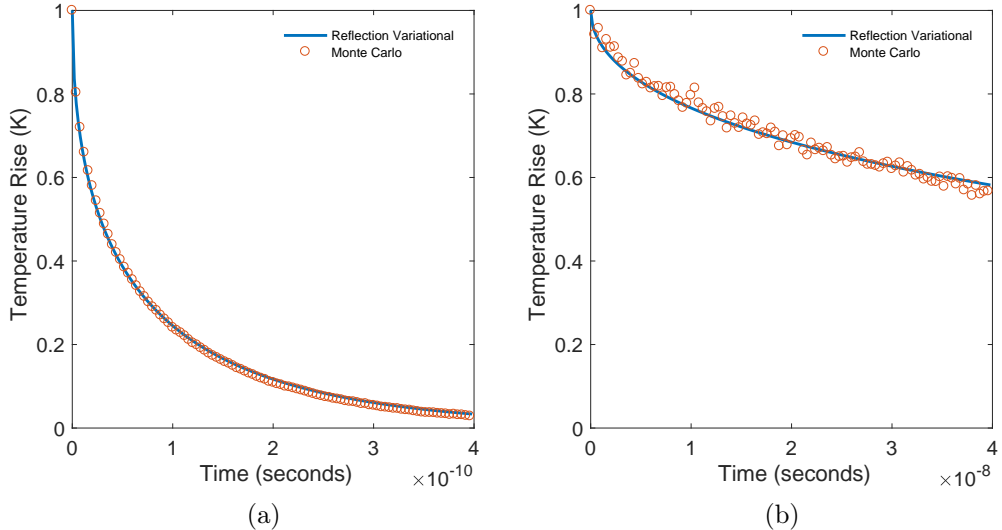


Figure 4-4: Temperature profiles obtained from Monte Carlo simulations compared with the corresponding variational predictions for  $\text{Si}_{93.4}\text{Ge}_{6.6}$  at 300 K with a (a) grating period of 100 nm and optical penetration depth of 10 nm and a (b) grating period of 10  $\mu\text{m}$  and optical penetration depth of 1  $\mu\text{m}$ . The Monte Carlo trace for case (b) contains noise because of the computational cost of simulating longer decays for a large number of effective particles. Reproduced from [1] with permission from the American Physical Society.

insufficient to characterize thermal transport. An example of this failure is presented in Appendix B. Even with such a limitation, our variational approach sufficiently characterizes the intermediate regime.

In the limit of  $q/\beta \ll 1$ , the variational method, using the Fourier temperature profile as input, reveals that the thermal conductivity that best recovers this behavior is the bulk value. This can be understood as a consequence of the constraint imposed by the equilibrium condition of Eq. 4.17, which dictates the behavior of the variational temperature profile in the large time limit where transport is diffusive. To ensure that this limitation is not present in the current experimental study, we compare against established Monte Carlo simulations of the RTA-BTE [53, 54].

As is seen in Figure 4-4, agreement at a grating period of 100 nm and an optical penetration depth of 10 nm and for a grating period of 10  $\mu\text{m}$  and an optical penetration depth of 1  $\mu\text{m}$  is observed. As our experiments have penetration depths on the order of 1  $\mu\text{m}$  for  $\text{Si}_{93.4}\text{Ge}_{6.6}$  [129], and use grating periods of between 1 and 13.5

$\mu\text{m}$ , we are not in the  $q/\beta \ll 1$  regime and we can move forward with our variational solutions.

## 4.3 Experiment

### 4.3.1 Sample specifications

The SiGe sample was fabricated by metal-organic chemical vapor deposition (MOCVD). Briefly,  $\text{SiH}_4$  and  $\text{GeH}_4$  enter the reactor, which break up into Si, Ge, and  $\text{H}_2$  from exposure to high temperatures ( $750\text{-}800^\circ\text{C}$ ). The composition is controlled by tuning the flow rates of  $\text{SiH}_4$  and  $\text{GeH}_4$ . A single crystal sample consisting of 93.4% Si, 6.6% Ge with a thickness of 6  $\mu\text{m}$  on a  $[1\ 0\ 0]$  oriented Si wafer with 6 degree off-cut towards the  $[1\ 1\ 1]$  plane was used for this work. Details of the sample fabrication and characterization can be found in previous work [130].

### 4.3.2 Results

All measurements of the  $\text{Si}_{93.4}\text{Ge}_{6.6}$  sample were conducted at room temperature. Figure 4-5a shows two examples of raw TTG data along with the fits obtained from using Eq. 4.7. These fits yield an effective thermal conductivity as shown in Figure 4-5b alongside the prediction from the variational solution using properties obtained from first principle calculations following Section 4.2. We have used an optical penetration depth of 1500 nm, according to [129]. The effect of uncertainty in the penetration depth is presented in Appendix B. There is good agreement between theory and experiment, which persists for a range of grating periods, from  $\sim 13.5$  to  $1\ \mu\text{m}$ .

## 4.4 Discussion and Outlook

To review, we calculated the first principles phonon properties to match the exact composition of the sample studied experimentally. We then used these properties and

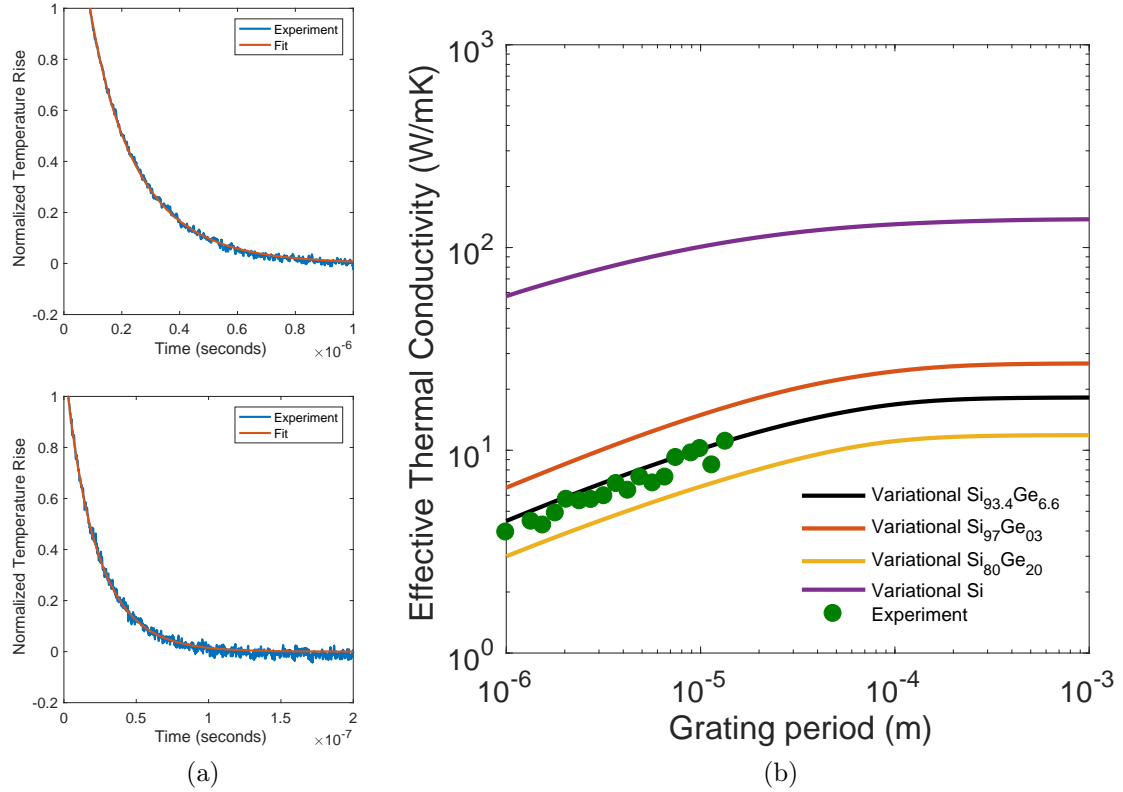


Figure 4-5: (a) Raw experimental data for 6.6  $\mu\text{m}$  (top) and 1.8  $\mu\text{m}$  (bottom) grating periods with the fit obtained from Eq. 4.7. (b) Green circles correspond to measured TTG data for a range of grating periods, from 13.5 to 1  $\mu\text{m}$ . The black line is the prediction from the variational solution with DFT properties as input, while the orange line (yellow line, purple line) corresponds to the variational prediction for Si<sub>97</sub>Ge<sub>3</sub> (Si<sub>80</sub>Ge<sub>20</sub>, Si). Reproduced from [1] with permission from the American Physical Society.

the variational solution to the RTA-BTE to predict (without any fitting parameters) the recorded observable of TTG experiments, the temperature decay. In doing so, we report excellent agreement between the observables and effective thermal conductivities of theory and experiment. In this section, we draw on past interpretations to provide some context for this work.

As mentioned earlier, one of the first explanations of size effects in SiGe grew out of the observation of frequency dependence in TDTR measurements [112]. This explanation relied on the application of thermal penetration depth,  $L_{tpd} \sim \sqrt{\frac{\alpha_{bulk}}{\omega}}$ , as a heuristic approximation to estimate the magnitude of the deviation from a bulk thermal conductivity. For  $\text{Si}_{93.4}\text{Ge}_{6.6}$ ,  $\alpha_{bulk} = 1.2358\text{E-}5 \text{ m}^2/\text{s}$ , with 10 MHz, yields a  $L_{tpd} \sim 1 \mu\text{m}$ . Under this approximation, we can take the MFP thermal conductivity accumulation function at  $1 \mu\text{m}$ , yielding  $0.4k_{bulk} = 7.3 \text{ W/mK}$ <sup>1</sup>. If we apply the same reasoning to our TTG measurements we arrive at a clear inconsistency:  $\lambda = 1 \mu\text{m}$  yields  $0.25k_{bulk} = 4.5 \text{ W/mK}$ , indicating that the MFP thermal conductivity accumulation function alone is insufficient to estimate the deviation from bulk. The next natural step in the interpretation of deviations from bulk required theory to go beyond the Heaviside cutoff of the thermal penetration depth and obtain a gray suppression function,  $S_{gray}(\eta_\omega)$ , from solving the gray BTE [135, 136, 20]

$$S_{gray}(\eta_\omega) = \frac{3}{\eta_\omega^2} \left(1 - \frac{\arctan(\eta_\omega)}{\eta_\omega}\right) \left(\frac{\eta_\omega}{\arctan(\eta_\omega)}\right). \quad (4.24)$$

This function is then used as a kernel in the effective thermal conductivity integral, i.e.,  $k_{eff,gray} = \frac{1}{3} \int_0^{\omega_m} C_\omega v_\omega \Lambda_\omega S_{gray}(\eta_\omega) d\omega$ . This picture has also turned out to be an oversimplification, since the fully spectral solution to the BTE has no suppression function due to the presence of the denominator term in Eq. 4.20. The presence of this term is a general feature of effective thermal conductivity expressions that is not

---

<sup>1</sup>By this same argument, frequency dependence should also be observed in silicon with  $\alpha_{bulk} = 8.8\text{E-}5 \text{ m}^2/\text{s}$ , which at 10 MHz, yields a  $L_{tpd} \sim 3 \mu\text{m}$  and  $\sim 0.7k_{bulk} = 98 \text{ W/mK}$  from the MFP accumulation function [17], but  $k_{exp} > 120 \text{ W/mK}$  for the same frequency range is often reported [117, 131]. The reason for this discrepancy remains an open question in the TDTR literature [132, 133, 116, 117, 134]. For example, the results of Hua et al. [116] and Wilson et al. [117] suggest that the reported thermal conductivity obtained from a TDTR measurement is dependent upon the interface conductance, indicating that this thermal conductivity can no longer be interpreted as an intrinsic property of the material.

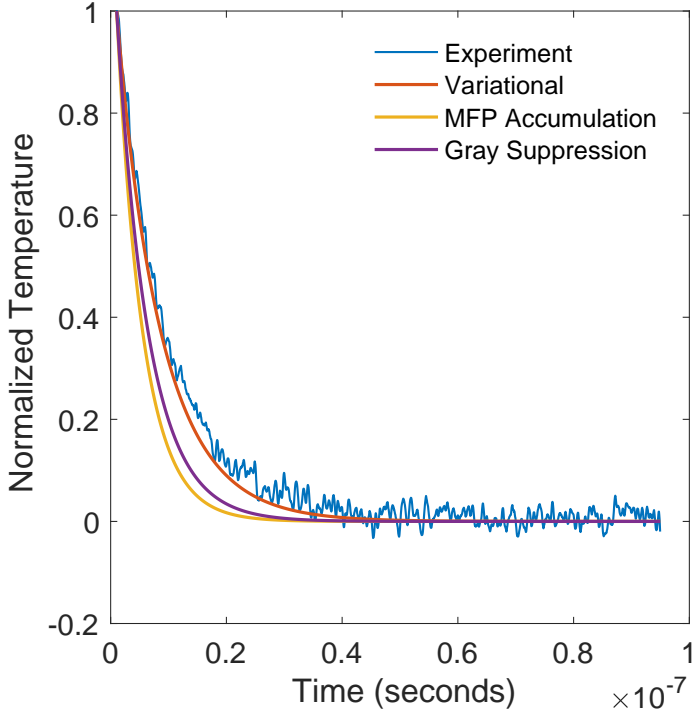


Figure 4-6: Comparison between the predictions from the variational approach to using the MFP accumulation function or the gray suppression function for one-dimensional TTG (Eq. 4.24) [3] to estimate the effective thermal conductivity at  $1.00 \mu\text{m}$  grating period. Reproduced from [1] with permission from the American Physical Society.

specific to the reflection mode TTG geometry [13, 3]. Our work confirms this fact by demonstrating that a fully spectral solution to the BTE is required to characterize experimental observables. The progression from thermal penetration depth to gray suppression to fully spectral interpretations in the context of reflection TTG is shown in Figure 4-6. While the gray BTE solution has been used to provide suppression functions for the MFP reconstruction problem [135, 56], we demonstrate that this assumption is invalid. Extending the MFP reconstruction problem to allow for fully spectral solutions is the subject of future work.

In contrast to the interpretation of thermal penetration depth of TDTR, the length scales in TTG do not depend on the intrinsic value of a material's transport coefficient, and are therefore physically well-defined independent variables. Although the information concerning the optical penetration depth is required, this is well within

current characterization technology [137]. Given that the variational solutions to the 1D and surface heating TTG geometries predict approximately the same effective thermal conductivity dependence on grating period, we have obtained estimates for the regimes in which the experiment is expected to match theory (i.e., when  $q/\beta$  is not much less than 1). In doing so, we have presented a theoretical framework that is testable, given that experimental deviations from theory can be understood as departures from the approximations used in this work: the VCA, the RTA-BTE and the specific trial solution for the temperature profile used in the variational method. These approximations can be lifted and are left for future work. With the methodology presented here, the TTG can be used to study in-plane transport in opaque thin films that require a supporting substrate.

While TDTR measurements are sensitive to the cross-plane transport, the TTG provides a complementary tool for measuring in-plane transport. The variational method can be extended to more complicated geometries, such as layered systems with interfaces, ideally suited for providing insight into the interpretations of TDTR and TTG measurements. Such an extension would provide a path towards unifying the interpretations of the measurements from TDTR and TTG.

## 4.5 Conclusion

Our TTG experimental results augmented with DFT-based modeling and the variational BTE solution indicate that this experimental geometry is capable of meeting the predictive criteria necessary for studying size effects on thermal transport in complex materials, such as the SiGe alloy studied here. Interesting questions can now be asked, such as in what systems or at what length scales can we expect to find a breakdown of the VCA? Moreover, this geometry will prove useful in the study of systems where the relaxation time approximation fails, such as graphene, graphite and diamond as will be shown in Chapter 5. The TTG platform provides a path towards tabletop studies of the microscopic properties of thermal transport.

# Chapter 5

## The Full Scattering Matrix BTE and Phonon Hydrodynamics

### 5.1 Introduction

In Chaper 3, we relied on the validity of Fourier's law to describe transport in the TDTR geometry and in Chapter 4, the RTA-BTE was used to describe transport in SiGe in the TTG geometry. Here, we go beyond these pictures. The RTA has an inherent flaw in that it is not energy conserving, and is best suited to describe materials with low Debye temperatures where the distinction between Normal and Umklapp process can be ignored [16, 11]. However, at low temperatures, interactions between phonons can be dominated by Normal processes (i.e.: processes that do not directly contribute to the dissipation of heat flux) because of the relatively high population of small wavevector modes, leading to a conceptual inadequacy of the RTA description in which all scattering events are treated as dissipative. In order to rigorously account for these normal scattering processes, the exact solution of LBTE [29] is required. The conventional approach to numerically solving the LBTE relies on an iterative strategy [138, 43], which has so far been limited to the case of diffusive transport in single crystal but in theory could be extended to include boundaries. As of this writing, the boundary effect is typically addressed via a phenomenological model which treats the boundary scattering probability as independent of a given mode's distance from

the boundary [139]. More recently, modern computational capabilities have made it possible to solve the LBTE directly using matrix algebra [139], as opposed relying on an iterative numerical procedure. Through direct diagonalization of the collision operator (also referred to as the scattering matrix), a “relaxon” description of transport was used to characterize transport beyond the RTA [140]. In a follow-up work, Cepelotti et al. [141] used the “relaxon” description to study in-plane thermal transport, where they assumed thermal equilibrium at the boundary which is not generally the case [142], and cross-plane thermal transport, where they assumed a diffusive temperature profile which fails to capture the temperature jump at the wall, a well-known effect in non-diffusive transport [143]. As such, the effect of heating source pattern on thermal transport has yet to be adequately considered in the exact solution to LBTE. The analysis considered here aims to address this missing piece by solving the LBTE with non-stationary and non-uniform heating profiles and provide a framework for the study of nondiffusive heat transport beyond the RTA. Here, we seek solutions for the LBTE with the complete collision operator, which contains the full details of the intrinsic phonon scattering processes obtained from first principles calculations. We obtain the temperature distribution for a material with no boundaries and with a general space and time dependent volumetric heat generation rate. Our solution provides a framework from which any heating configuration can be constructed.

As a concrete example, we provide predictions for the simple configuration of a steady state thermal grating (SSTG) in one dimension to demonstrate the difference between the thermal transport predicted by using the full scattering matrix compared to the RTA for graphene. Furthermore, we will demonstrate that this formalism is capable of capturing hydrodynamic phenomena [144], such as second sound, enabling the prediction of hydrodynamic observables in current and practical experimental configurations and thereby opening the door for systematic experimental work.

## 5.2 Theory

In Section 2.1.1, a derivation of the bulk LBTE was presented. Like the size effect study under the RTA-BTE presented in Chapter 3, we will extend the LBTE to include a source term  $Q_n$

$$\frac{\partial g_n}{\partial t} + \vec{v}_n \cdot \nabla g_n = \sum_{n'} \tilde{\Omega}_{n,n'} (g_{n'}^0 - g_{n'}) + Q_n. \quad (5.1)$$

Eq. 5.1 is now further linearized so that not only are deviations of the nonequilibrium distribution from the equilibrium distribution at the local temperature small, but also the deviations of the equilibrium distribution from the background constant temperature distribution are also small

$$f_n^0 \approx f_{BE}\left(\frac{\hbar\omega_n}{k_B T_0}\right) + \frac{\hbar\omega_n}{Nv} c_n \delta T. \quad (5.2)$$

In doing so, the scattering matrix  $\tilde{\Omega}$  will depend on the background room temperature  $T_0$  but not on the temperature rise  $\delta T$ . Recalling that  $g_n = \frac{\hbar\omega_n}{Nv} \left( f_n - f_{BE}\left(\frac{\hbar\omega_n}{k_B T_0}\right) \right)$  and  $g_0 = \frac{\hbar\omega_n}{Nv} \left( f_n^0 - f_{BE}\left(\frac{\hbar\omega_n}{k_B T_0}\right) \right) = c_n \delta T$  and setting  $\frac{1}{Nv} \sum_n f_{BE}\left(\frac{\hbar\omega_n}{k_B T_0}\right) = \frac{1}{Nv} \sum_n \hbar\omega_n f_n$  gives the temperature rise as the ratio of the nonequilibrium energy density of phonons divided by the heat capacity

$$\delta T = \frac{1}{C} \sum_n g_n. \quad (5.3)$$

Inserting  $g_n^0 = c_n \delta T$  into Eq. 5.1 gives

$$\frac{\partial g_n}{\partial t} + \vec{v}_n \cdot \nabla g_n = \sum_{n'} \tilde{\Omega}_{n,n'} (c_{n'} \delta T - g_{n'}) + Q_n. \quad (5.4)$$

To solve for the phonon distribution for a system with no boundaries, we take the spatial and temporal Fourier transform of Eq. 5.4 to convert the differential equation into an algebraic matrix equation

$$(i\omega + i\vec{q} \cdot \vec{v}) \tilde{\vec{g}} = \tilde{\Omega}(\delta \tilde{T} \vec{c} - \tilde{\vec{g}}) + \tilde{Q} \vec{p} \quad (5.5)$$

where  $\tilde{\cdot}$  denotes the Fourier transformed variable. Rearranging for the Fourier transform of the deviational non-equilibrium distribution function yields

$$\tilde{g} = \tilde{Q}\Omega^{-1}\vec{p} + \delta\tilde{T}(I - i\Omega^{-1}D\vec{c}) \quad (5.6)$$

where  $\vec{p} = \vec{c}/C$  and we utilize the following notation to define the vectors and matrices in this work

$$D_{n,n'} = (\omega + \vec{q} \cdot \vec{v}_n)\delta_{n,n'} \quad (5.7)$$

$$\Omega_{n,n'} = \tilde{\Omega}_{n,n'} + (\omega + \vec{q} \cdot \vec{v}_n)i\delta_{n,n'}. \quad (5.8)$$

We note that  $\omega$  represents the frequency from the Fourier transform, so as not to be confused with the frequency of a particular phonon mode,  $\omega_n$ . A similar Fourier transform strategy was used by Hua and Minnich for the RTA-BTE [126]. We solve for  $\delta\tilde{T}$  after inserting Eq. 5.6 into Eq. 5.3

$$\delta\tilde{T} = \tilde{Q} \frac{\text{sum}[\Omega^{-1}\vec{p}]}{\text{sum}[i\Omega^{-1}D\vec{c}]} \quad (5.9)$$

where we define the sum operation of a vector to add up the values of its elements, i.e.:  $\text{sum}[a] = \sum_n a_n$ . Eq. 5.9 is the essence of the contribution of this work. This provides the general temperature response from the BTE for a configuration with no boundaries, but with an arbitrary heating profile  $\tilde{Q}$ , with the full scattering matrix under the linear temperature response assumption. Given the scattering matrix  $\tilde{\Omega}$  of a crystal, and the heating profile  $Q$ , the temperature rise in the Fourier transformed domain can be calculated and then inverse Fourier transformed to yield the temperature rise as a function of space and time. The computational difficulty lies in inverting the matrix  $\Omega$ , which involves the full scattering matrix  $\tilde{\Omega}$ , which scales as  $O(Nb)$  where  $N$  is the number of discretized  $q$  points in the BZ and  $b$  is the number of branches.

Taking the solution of Eq. 5.9 and inserting into Eq. 5.6 yields the nonequilibrium

phonon energy density distribution

$$\tilde{\vec{g}} = \tilde{Q} \left( \Omega^{-1} \vec{p} + \frac{\text{sum}[\Omega^{-1} \vec{p}]}{\text{sum}[i\Omega^{-1} D \vec{c}]} (I - i\Omega^{-1} D \vec{c}) \right). \quad (5.10)$$

Using the phonon distribution function, one can calculate not only the temperature response, but also the dynamics of individual phonon modes. This formalism and the solution provided by Eq. 5.9 enables the study of thermal transport in the absence of boundaries in the nondiffusive regime.

## 5.3 Numerical studies

### 5.3.1 Steady state TG

As a preliminary example, we study the one dimensional steady state thermal grating (SSTG), in which the heating in the system is given by a sinusoid. A steady state sinusoidal thermal grating is given by  $Q = \bar{Q} e^{iqr}$  in complex number notation. This is a grating in one dimension along the direction of the vector  $q$  in the 3D volume with a grating period  $\lambda = 2\pi/q$ . The elegance of this geometry is that the temperature distribution predicted by the Fourier heat conduction equation and by the BTE are identical: both are sinusoids of the same spatial wavevector  $q$  as the volumetric heating profile. The temperature profile from the Fourier heat conduction equation is given by

$$\delta T = \bar{Q} \frac{e^{iqr}}{q^2 k_q} \quad (5.11)$$

where  $k_q = q^T K q$  is the element of the thermal conductivity tensor in the direction of the thermal grating. By matching the Fourier temperature profile to the solution of the BTE for the case of a SSTG from Eq. 5.9, an effective thermal conductivity is derived which depends on the grating spacing  $\lambda$  and has a similar structure to the previous effective thermal conductivities derived using the variational method [3, 127]<sup>1</sup>

---

<sup>1</sup>In this geometry, a nondiffusive effective thermal conductivity can be exactly calculated with no approximation by matching the Fourier temperature profile to the BTE temperature profile, unlike

$$k_q = \frac{1}{q^2} \frac{\text{sum}[i\Omega^{-1}Dc]}{\text{sum}[\Omega^{-1}p]} \quad (5.12)$$

where the matrix  $\Omega$  is given by Eq. 5.7 like before, but the matrix  $D$  simplifies to the steady form (zero frequency) given by  $D_{n,n'} = (\vec{q} \cdot \vec{v}_n)\delta_{n,n'}$ . Visually, the appearance of the complex number  $i$  is not an issue as the inversion symmetry of the crystal will guarantee that the effective thermal conductivity will be a purely real quantity. This effective conductivity is valid for  $d$ -dimensional material in the absence of boundaries or when the scattering at boundaries does not have a strong effect on the thermal transport. The effective conductivity obtained for the steady state configuration is exactly the conductivity that would be obtained from a variational solution with the energy conservation condition considering a control volume over all time [3]. Therefore, for the one dimensional *transient* thermal grating decay, the conductivity from Eq. 5.12 can be understood as the parameter that matches the area under the decay curve from the exact solution to the approximate variational solution.

We explore the comparison between predictions obtained using the full scattering matrix and the RTA for graphene to illustrate the need for the previously described theoretical framework. Figure 5-1 shows the effective thermal conductivity as a function of the grating period for the case of a thermal distribution. This represents the first effective thermal conductivity derived for a material with the full scattering matrix in a nondiffusive heat transfer configuration without boundary scattering.

---

more complicated geometries.

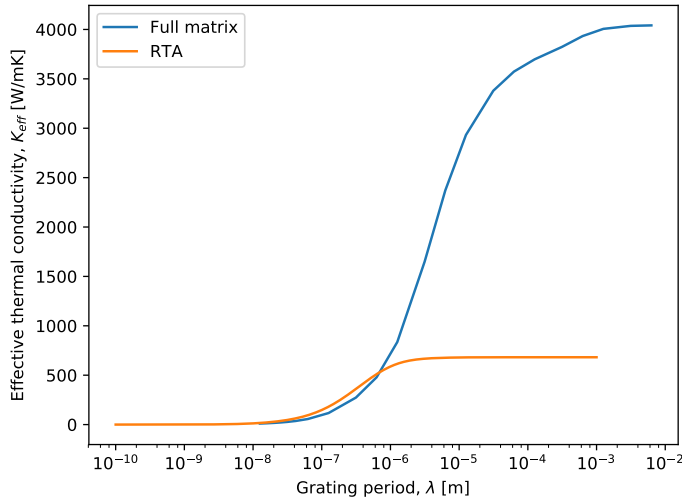


Figure 5-1: Effective thermal conductivity of graphene at room temperature as a function of the grating period for the steady state thermal grating geometry.

All DFT calculations for graphene were done with the quantum-ESPRESSO package [125] using the C.pz-vbc.UPF pseudopotential. Graphene was simulated using a hexagonal unit cell with 2 carbon atoms at the relative coordinates of  $[0,0,0]$  and  $[\frac{1}{3}, \frac{2}{3}, 0]$  and lattice parameters  $a = 4.61$  Bohr and  $c/a = 10.2$  Bohr. For the DFPT portion, a  $32 \times 32 \times 1$  Monkhorst-Pack  $k$  mesh with a kinetic energy cutoff of 100 Ry and a convergence criteria of 1E-12 Ry was used. These DFPT calculations were performed on an  $8 \times 8 \times 1$   $q$  mesh. An  $8 \times 8 \times 1$  supercell such that interactions up to the fifth nearest neighbor could be captured was used for extraction of the third order force constants (only electronic wavefunctions at the Gamma point were considered for the sake of computational efficiency) [139]. The full scattering matrix was constructed using the D3Q module [139]. The matrix was constructed by interpolating to  $64 \times 64 \times 1$   $q$  mesh with a Gaussian smearing parameter of  $20 \text{ cm}^{-1}$  for the Kronecker delta approximation to yield convergence of the thermal conductivity. The direct inversion of  $\Omega$  in Eq. 5.12 was performed using the NUMPY library [145] on a cluster consisting of Intel CPU cores operating at 2.8 GHz with access to 128 Gb of memory.

As reported elsewhere [146, 147], the bulk value of the thermal conductivity de-

pends on the chosen BTE scattering kernel. We are able to further demonstrate that the grating period at which size effects become observable also depends on the scattering kernel. Figure 5-1 captures the prediction that size effects in graphene in a SSTG geometry can be observed for grating periods of around  $100 \mu\text{m}$  at room temperature. RTA, on the other hand, predicts the onset of size effects occurs at grating periods of only a few micron.

### 5.3.2 Hydrodynamic regime

The SSTG provides theoretically elegant system to study because of the exact matching between the Fourier and BTE profiles, thereby ensuring a well-defined effective thermal conductivity. However, there are thermal transport regimes where an effective thermal conductivity will fail to adequately capture the dynamics of thermalization, of which two are of interest: the ballistic and the hydrodynamic regimes. The ballistic limit was discussed in Chapter 2. Phonon hydrodynamics has a long history; of which a short retelling will be giving here.

#### Second sound and phonon hydrodynamics history

As theoretical attempts at understanding the exotic properties of liquid helium II were put forward, the possibility of observing a phenomenon that eventually became known as second sound emerged. Tisza, building upon the ideas of London, proposed a description of the superfluid phase where a portion of the atoms composed a degenerate ground state while the remaining atoms existed in excited states [148]. By assuming the interaction between these two phases to be negligible, a hydrodynamic description, often referred to as a "two-fluid model", of the composite system revealed the existence of wave propagation of temperature differences. Landau independently arrived at a similar prediction, with a detailed description of the excited phase [149], composed of both phonons and rotons.

Experimental confirmation of the existence of second sound in helium II below the lambda point (2.18 K) was first provided by Peshkov [150] and later by Lane et al.

[151]. The slow velocity of the second sound speed (10-20 m/s) made the detection accessible to the rudimentary instruments available at the time.

Peshkov [152] and later Ward and Wilks [153] pointed out that the same hydrodynamical concepts apply to a phonon gas in crystalline materials under conditions in which phonons momentum-conserving processes dominate over Umklapp processes. This prediction was experimentally confirmed first in solid Helium by Ackerman et al. at temperatures below 0.7 K [154]. Direct observations of second sound in other solids include He<sup>3</sup> in a temperature range of 0.42 to 0.58 K [155], NaF in a temperature range of 11 to 14.5 K [156, 157] and Bi in a temperature range of 1.2 to 4 K [158].

Theoretical developments of the description of second sound in crystalline solids were led by Guyer and Krumhansl, who applied the Callaway collision kernel to the phonon BTE to derive a set of hydrodynamical equations for the conservation of energy and momentum [159]. Hardy solved the full collision matrix BTE [160] in terms of the eigenvectors of the collision matrix, but lacked the necessary data to explicitly construct the collision matrix. In parallel, Gotze and Michel adopted a phonon Green's function description to demonstrate the existence of hydrodynamic singularities [161]. By carefully calculating the contributions to these singularities, the authors were able to derive a similar two-fluid description to the one initially proposed by Tisza, where the equations of motion of the elastic deformation and the phonon gas are weakly coupled.

With these theoretical ideas, it became clear that there existed other hydrodynamic signatures beyond second sound. Sussman and Thellung [162] and, independently, Gurzi [163] showed that, under the same conditions that give rise to second sound, a steady state temperature difference geometry can bring about a drift motion of the phonon gas. Given the similarity to flow of a fluid under the steady state application of a pressure difference, this motion is referred to as a Poiseuille flow of phonons. Guyer and Krumhansl pointed out the possibility of observing this Poiseuille flow by reporting the scaling of thermal conductivity as a function of temperature [164]. This observation coincided with Mezov-Deglin, who experimentally reported the thermal conductivity as a function of temperature for solid He and observed a scaling of  $T^{7-8}$

prior to the maximum [165]. This temperature scaling, shown in Figure 5-2, has been used as indirect evidence for hydrodynamic transport in strontium titanate in a temperature range of  $\sim$  7 to 11 K [166] and black phosphorus in a temperature range of  $\sim$  5 to 12 K [167]. However, this scaling has not been reported in other candidate materials that are predicted to support phonon hydrodynamics, such as graphene [168] and graphite [169], and therefore direct observation of hydrodynamic signatures must be sought.

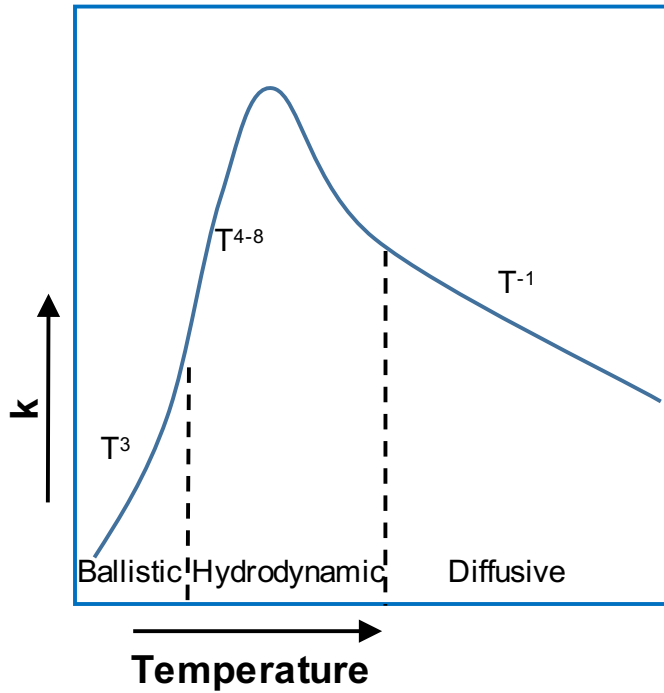


Figure 5-2: Schematic of the hydrodynamic window for a crystalline solid.

There has been a recent resurgence in the interest of observing second sound with the emergence of 2D materials being projected to be good candidates for supporting hydrodynamic phenomena [25, 26]. We make these predictions concrete with the experimental observation of hydrodynamic transport in graphite using the theory developed in Section 5.2.

## A conceptual description of second sound

To provide some physical intuition behind phonon hydrodynamics, we begin by following Prohofsky and Krumhansl [170]. Let us consider a gas composed of hard particles experiencing plane-wave sound propagation in the  $x$  direction. The density is denoted as  $\rho(x, t) = \rho_0 + \rho_1(x, t)$ , with  $\rho_0$  being the equilibrium density and  $\rho_1$  being the change in density due to the sound wave. For a given differential volume, the gas has a velocity  $u_x$  with respect to the lab reference frame.

The conservation of mass is written as

$$\frac{\partial \rho_1}{\partial t} + \frac{\partial}{\partial x}(\rho_0 u_x) = 0. \quad (5.13)$$

The conservation of momentum is written as

$$\frac{\partial \rho_0 u_x}{\partial t} = -\frac{\partial P}{\partial x} + f_x = -\frac{\partial P}{\partial \rho_0} \frac{\partial \rho_1}{\partial x} + \frac{-\rho_0 u_x}{\tau}. \quad (5.14)$$

Combining by taking the  $\frac{\partial}{\partial x}$  of Eq. 5.13 and  $\frac{\partial}{\partial t}$  of Eq. 5.14 yields

$$\frac{\partial^2(\rho_0 u_x)}{\partial t^2} + \frac{1}{\tau} \frac{\partial(\rho_0 u_x)}{\partial t} = \frac{\partial P}{\partial \rho_0} \frac{\partial^2}{\partial x^2}(\rho_0 u_x). \quad (5.15)$$

Eq. 5.15 is the damped wave-equation with solutions of the form:

$$\rho_0 u_x(t) \propto e^{-t/\tau} \sin(\omega t + \phi). \quad (5.16)$$

The difference between the diffusive regime and the hydrodynamic regime can now be stated. When  $\omega\tau \gg 1$ , the wave is underdamped and wave phenomena can be observed. This is the hydrodynamic regime.  $\omega\tau \ll 1$ , the wave is overdamped and the diffusive regime applies. A depiction of the two regimes is shown in Figure 5-3.

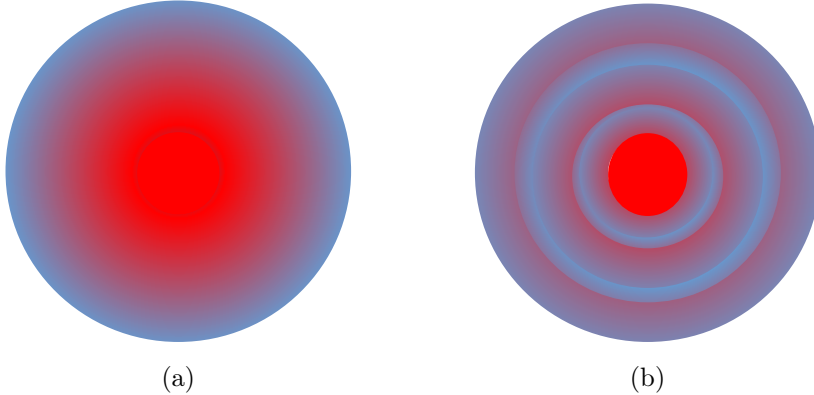


Figure 5-3: Schematic depiction of (a) diffusive and (b) hydrodynamic transport of gas particles.

The extension from a gas of hard particles to the case of a phonon gas traditionally begins with the Callaway approximation to the BTE [160, 171]

$$\frac{\partial f_n}{\partial t} + \vec{v}_n \cdot \nabla f_n = \frac{f_n^0 - f_n}{\tau_{n,Umkapp}} + \frac{f_n^0 - f_n^*}{\tau_{n,Normal}} \quad (5.17)$$

where  $\tau_{Umkapp}$  and  $\tau_{Normal}$  are the Umklapp and Normal scattering rates respectively, which are related to the RTA relaxation times by

$$\frac{1}{\tau_{RTA}} = \frac{1}{\tau_{Umkapp}} + \frac{1}{\tau_{Normal}}. \quad (5.18)$$

$f_n^*$  is referred to as the flowing or displaced distribution and is assumed to take the form

$$f_n^* = \frac{1}{e^{\beta\hbar(\omega_n - \vec{q} \cdot \vec{u})} - 1} \quad (5.19)$$

where  $q$  is the phonon wavevector and  $u$  is a “drift velocity”. When Normal processes are assumed to dominate and momentum is conserved <sup>2</sup>, the out-of-equilibrium dis-

---

<sup>2</sup>Confusion often arises over this point. Quasi- or crystal-momentum is not real momentum. Consider the following thought experiment. A neutron with an observable momentum impacts a crystal, interacts, and scatters. The momentum of the scattered neutron is reduced by an amount  $k$ , corresponding to the excitation of a phonon of  $k$ . If we stop here, it would seem that quasi and real momentum are equivalent. However, we are always free to add a reciprocal lattice vector without violating conservation of quasi-momentum, so  $k \rightarrow k + G$ . This freedom confirms the observation that the real momentum of the neutron is transferred to the bulk translation of the center of mass of

tribution is subsequently set to the displaced distribution

$$f_n \approx f_n^* \approx f_n^0 + \beta \hbar f_n^0 (f_n^0 + 1) q \cdot u. \quad (5.20)$$

Without loss of generality, an isotropic crystal with transport along a single dimension is considered. Eq. 5.13 is converted from conservation of mass to conservation of energy by multiplying by  $\hbar\omega_n$  and summing over  $n$

$$\frac{\partial \sum_n \hbar\omega_n f_n}{\partial t} + \sum_n \hbar\omega_n v_n \nabla f_n = 0 \quad (5.21)$$

setting  $E = \sum_n \hbar\omega_n f_n$  and  $Q = \sum_n v_n \hbar\omega_n f_n$  gives<sup>3</sup>

$$\frac{\partial E}{\partial t} + \nabla Q = 0 \quad (5.22)$$

where we have assumed that the collision term satisfies energy conservation. Like the RTA, the Callaway kernel doesn't satisfy energy conservation unless all modes have an identical  $\tau$ . Nevertheless, this detail doesn't appear to obscure the essential physics. To obtain a relation for heat flux, Eq. 5.17 is multiplied by  $v_n \hbar\omega_n$  and again summing over  $n$

$$\frac{\partial \sum_n v_n \hbar\omega_n f_n}{\partial t} + \sum_n v_n \hbar\omega_n v_n \nabla f_n = \sum_n \frac{v_n \hbar\omega_n f_n}{\tau_{n,Umkapp}}. \quad (5.23)$$

Noting that the  $f_n^0 (f_n^0 + 1) q \cdot u$  is odd in  $q$  and setting  $\nabla f_n = \frac{\partial f_n^0}{\partial T}|_{T_0} \nabla T$  and  $K = \sum_n v_n^2 \hbar\omega_n \frac{\partial f_n^0}{\partial T}|_{T_0}$ , we find

$$\frac{\partial Q}{\partial t} + K \nabla T + \frac{Q}{\tau_{II}} = 0. \quad (5.24)$$

Combining by taking  $\frac{\partial}{\partial t}$  of Eq. 5.22 and  $\nabla$  of Eq. 5.24 and using the proportionality between  $E$  and  $T$ , we arrive at a damped wave equation for temperature

---

the crystal. Alternatively, one can ask: does heat transport imply real momentum transport? Any molecular dynamics simulation answers in the negative. This point becomes overlooked once a BTE framework is adopted and the real crystal has been abstracted away.

<sup>3</sup>The unit cell volume prefactor cancels out.

$$\frac{\partial^2 T}{\partial t^2} + \frac{1}{\tau_{II}} \frac{\partial T}{\partial t} = v_{II} \nabla^2 T \quad (5.25)$$

where the speed of second sound is defined as

$$v_{II}^2 = \frac{\sum_n c_n v_n \cdot v_n}{\sum_n c_n} \quad (5.26)$$

and the decay constant is

$$\frac{1}{\tau_{II}} = \frac{\sum_n f_n^0 (f_n^0 + 1) \hbar \omega_n v_n q_n \frac{1}{\tau_{n,Umkapp}}}{\sum_n f_n^0 (f_n^0 + 1) \hbar \omega_n v_n q_n}. \quad (5.27)$$

Now, we have a concrete expectation of what we are looking for: wave-like solutions to the temperature equation. However, in arriving at this equation, we assumed knowledge of the form for the  $f_n$  term<sup>4</sup> and sacrificed energy conservation. Furthermore, since a heating source term was neglected and boundaries were ignored, Eq. 5.25 must be considered to be a bulk description. The shortcomings of the above description of phonon hydrodynamics can be surmounted by adopting the LBTE framework developed in Section 5.2.

Using this LBTE theory, we can avoid invoking the displaced distribution ansatz while simultaneously capturing deviations from bulk transport and satisfying energy conservation by explicitly calculating the temperature response obtained from directly solving the LBTE for a given geometry, given by Eq. 5.9. The simplest geometry is constructed by setting  $\tilde{Q}$  (i.e.:  $Q(r, t) = \bar{Q} e^{iqr} \delta(t)$ ) in Eq. 5.9 to a scalar quantity which corresponds to the temperature response for the 1D-TTG. Unlike the calculation of effective thermal conductivity of the SSTG using Eq. 5.12, Eq. 5.9 requires the inversion of  $\Omega$  for not only each grating  $q$ , but also for each frequency  $\omega$ . Since  $\delta T(\omega, q)$  is an uncoupled equation for  $\omega$  and  $q$ , the calculation is amenable to a trivial parallelization methodology where tuples of  $(\omega, q)$  can be processed simultaneously on different CPU cores. The matrices in this work are on the order of 25000 by 25000, which takes about 30 minutes to directly invert on a 2.8 GHz core. Using this par-

---

<sup>4</sup>If the expansion of Eq. 5.20 is taken to the second order, a non-linear term for heat flux is obtained and the heat flux equation, Eq. 5.24 becomes analogous to the Navier-Stokes equation [172].

allelization scheme, the time to calculate the temperature response in the frequency domain is on the order of a single day (depending on the number of cores available).

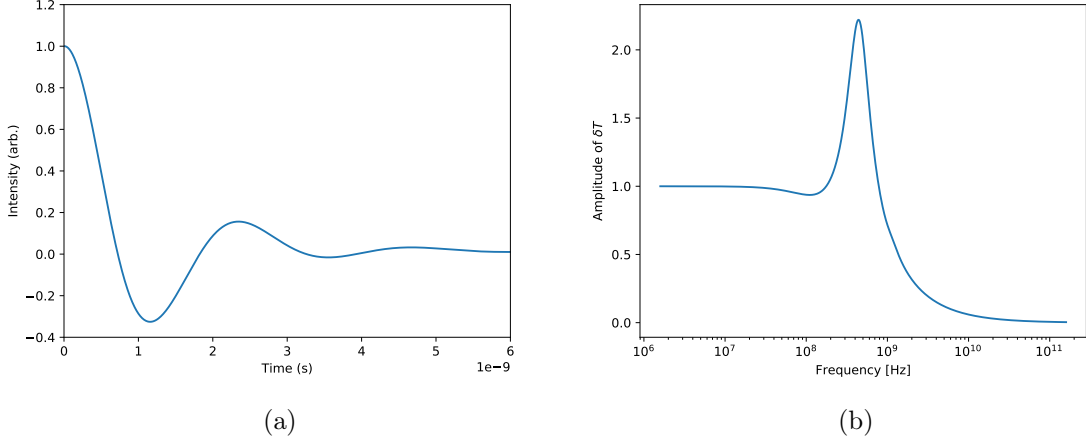


Figure 5-4: (a) Time-domain and (b) frequency-domain representation of the temperature response for isotopically-pure graphite at 100 K in the 1D-TTG geometry.

Figure 5-4 is an example of one such calculation for isotopically pure graphite at 100 K for a  $10 \mu\text{m}$  grating. We use the second- and third-order force constants calculated by Zhiwei Ding [173] to construct  $\tilde{\Omega}$  on a  $16 \times 16 \times 8 q$  mesh with a Gaussian smearing parameter of  $20 \text{ cm}^{-1}$  for the Kronecker delta approximation is used. The size of  $\tilde{\Omega}$  is presently limited by memory resources because direct inversion requires, at a minimum, both the original and inverted matrix to be stored in memory<sup>5</sup>. A strong resonance is observed in the frequency domain and the corresponding sign flip of  $\delta T$  is observed in the time domain. This change in sign corresponds to the shifting of the original temperature maximum by one half of a grating period, which we attribute to be a signature of hydrodynamic phonon transport since the hot and cold regions of the initial heating profile have become reversed while maintaining the original symmetry of the initial heating profile. Using the resonance frequency and grating period as time and length scales, the second sound speed is estimated to be  $v_{II} = 4100 \text{ m/s}$ . The damping time constant,  $\tau_{II}$ , can be extracted by fitting a Lorentzian, which is the Fourier transform of Eq. 5.16, to the resonance. Therefore, the

---

<sup>5</sup>A larger mesh was used in [173] under the Callaway approximation, but meshes comparable to the one used here have been used in the past [174] to study the LBTE.

relevant macroscopic observables can be obtained from LBTE framework presented in Chapter 2.

Our task is now clear. Given a material at a reference background temperature, we simply sweep through the temporal and spatial Fourier transform variables that are input into Eq. 5.9 in search of resonant features in the temperature response. In other words, rather than following the usual strategy and looking for materials that meet the condition  $\tau_{Normal} \gg \tau_{Umklapp}$  [26, 173], we seek materials and geometries that contain poles<sup>6</sup> in Eq. 5.9. Using the same D3Q codebase that was previously used to calculate the effective thermal conductivity in graphene, we have generated collision matrices for graphene and graphite under a range of temperatures and defect concentrations. By sweeping through grating periods, we can construct a hydrodynamic dispersion relation (i.e.: the dependence of  $\omega$  on  $q$ ) and in doing so determine the so-called hydrodynamic window.

---

<sup>6</sup>The poles here are reminiscent of the poles of a single particle Green's function that become associated with quasiparticles [175].

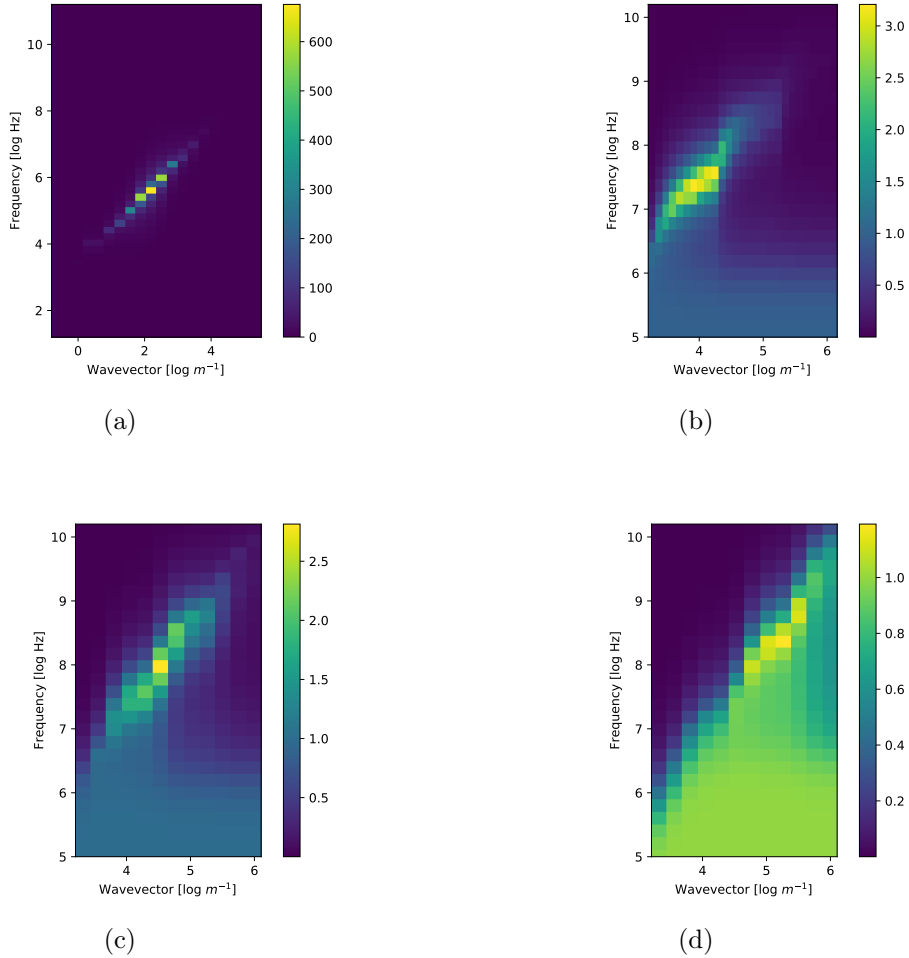


Figure 5-5: Hydrodynamic dispersion relations via grating period versus frequency ( $\omega$ ) plots for graphene (a) at 50 K with no isotopes, (b) at 50 K with isotopes, (c) at 100 K with isotopes and (d) at 300 K with isotopes. The intensity of corresponds to the ratio of the amplitude of  $\delta T(\omega, q)$  to the amplitude of  $\delta T(0, q)$ .

Hydrodynamic dispersion relations for graphene are shown Figure 5-5, where the intensity of the colormap corresponds to the ratio of the amplitude of  $\delta T(\omega, q)$  to the amplitude of  $\delta T(0, q)$ . The resonant frequency approximately scales linearly with wavevector. Two observations can be made. The first is that with increasing temperature, the hydrodynamic window shifts to higher frequencies and smaller gratings, while the intensity of the resonances decreases with temperature. This can be understood as a consequence of the higher energy phonon modes, that become activated with increasing temperature, playing the role of opening momentum relaxation chan-

nels that destroy the modes that preserve the direction of heat flux necessary for the emergence and propagation of a temperature wave. The second observation is that isotope scattering has a strong effect on the intensity of the resonance. This effect is similar to that of increasing temperature; isotope scattering is a momentum relaxing process. The hydrodynamic window for isotopic graphene, constructed by taking the maximum value of the derivative of  $\delta T(\omega, q)$  with respect to  $\omega$  for each grating period<sup>7</sup>, is shown in Figure 5-6.

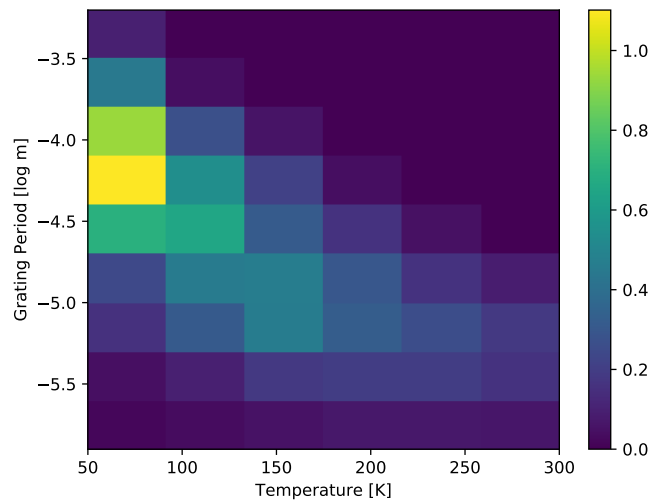


Figure 5-6: The hydrodynamic window of isotopic graphene.

---

<sup>7</sup>Recall that an ideal resonance will have a positive infinite derivative and in the absence of a resonance, the maximum derivative will be zero.

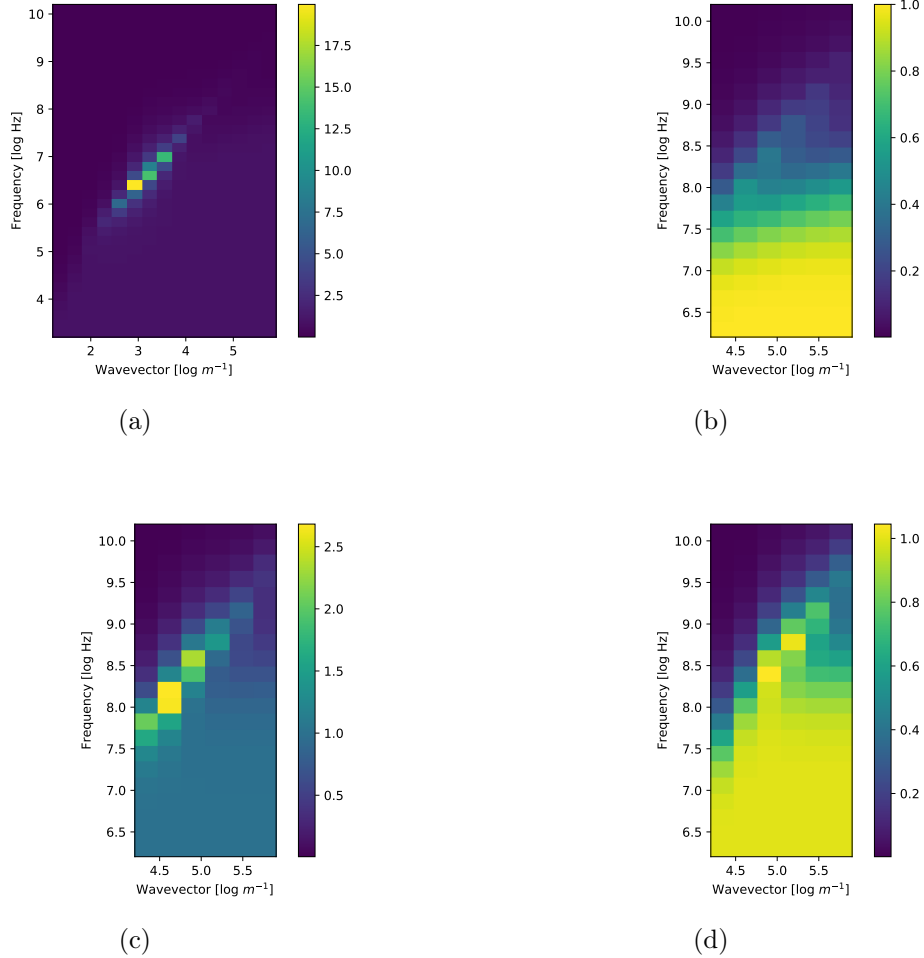


Figure 5-7: Hydrodynamic dispersion relations via grating period versus frequency ( $\omega$ ) plots for graphite (a) at 50 K with no isotopes, (b) at 50 K with isotopes, (c) at 100 K with no isotopes and (d) at 100 K with isotopes.

Hydrodynamic dispersion relations for graphite are shown in Figure 5-7. In contrast to graphene, the hydrodynamic window is narrower and the intensities of the resonances are reduced. As shown in Figure 5-7b, at low enough temperatures, the isotope scattering processes dominate the intrinsic phonon-phonon processes, thereby closing the hydrodynamic window (shown in Figure 5-8 and constructed in an identical manner to that of graphene). Nevertheless, as predicted in [173], a distinct hydrodynamic regime exists, under a natural abundance of carbon isotopes, and is accessible to experimental inquiry, which is the subject of the following section.

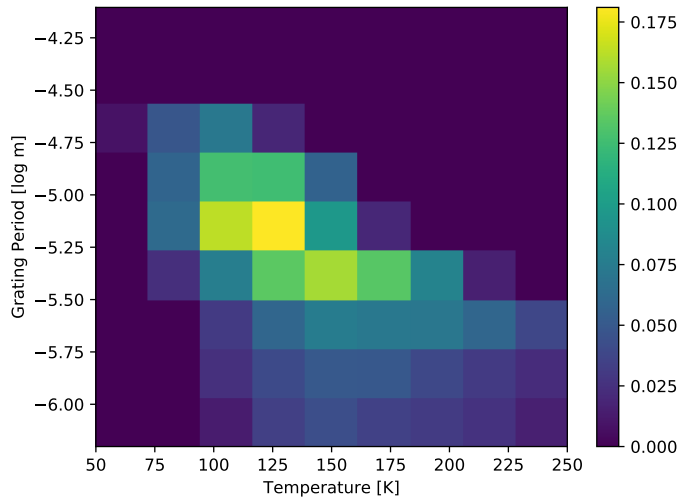


Figure 5-8: The hydrodynamic window of isotopic graphite.

## 5.4 Experiments

### 5.4.1 Graphite

Like diamond and graphene, graphite is a suitable candidate for testing the LBTE theory because of its high thermal conductivity and high Debye temperature. However, unlike diamond, graphite is crystallographically anisotropic, with layers of  $sp^2$  bonded graphene stacked with weak Van der Waals interactions.

We use commercially available highly-oriented pyrolytic graphite samples purchased from SPI. XRD analysis on a representative sample reveals that the expected A-B-A-B orientation between layers is lacking. Future work with higher quality samples is expected to yield better agreement between theory and experiment.

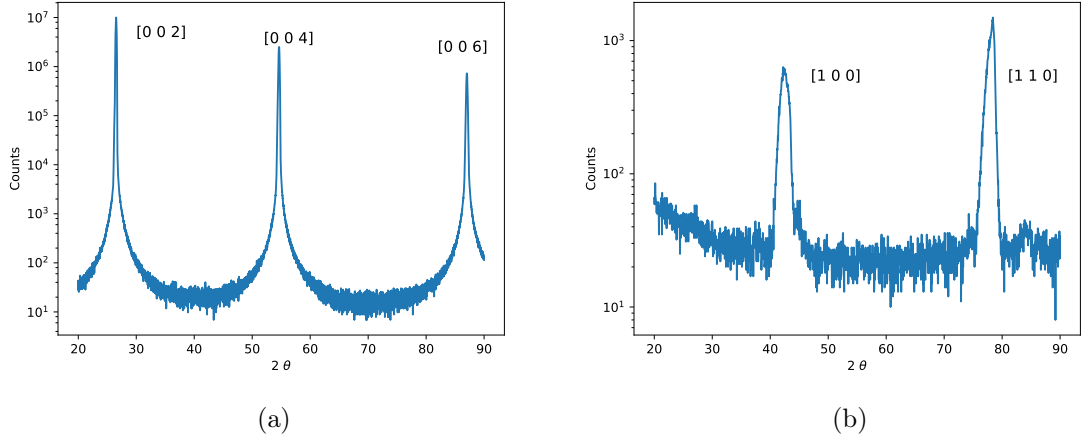


Figure 5-9: (a) Out-of-plane XRD and (b) in-plane XRD on HOPG.

### Room temperature measurements

Room temperature measurements on HOPG were performed by Ryan Duncan using the same TTG setup as described in Section 2.2.2. Due to the strong thermal conductivity anisotropy ( $k_{ab} = 1800 - 2000$  W/m-K and  $k_c = 6 - 10$  W/m-K [169]), the thermal transport is one-dimensional in the  $ab$  plane, which is confirmed by the pure exponential behavior of the experimental temperature decays.

The effective thermal conductivity of graphite is calculated using Eq. 5.12. The result is plotted in Figure 5-10. General agreement between the full scattering matrix theoretical predictions and the experimental TG measurements is obtained. While the bulk theoretical and experimental measurements of the HOPG are  $\sim 2000$  and  $\sim 1850$  W/m-K respectively, the normalized trend in effective thermal conductivities agree. This suggests that only a single parameter rescaling is needed to go from the theoretical prediction to the experimental measurement. The Callaway model [173], on the other hand, is unable to recover the experimental trend.

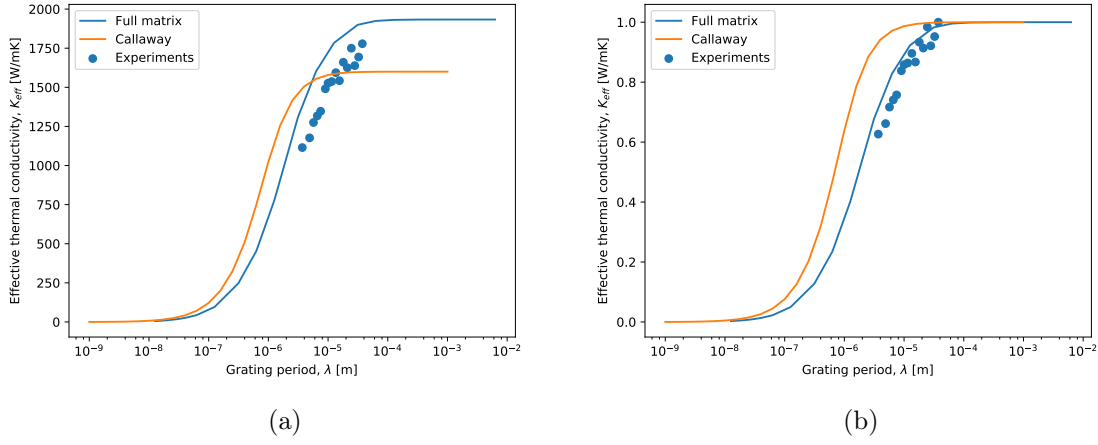


Figure 5-10: Theoretical predictions of the (a) absolute and (b) normalized effective thermal conductivity alongside TTG measurements of graphite at room temperature.

### Low temperature measurements

Liquid nitrogen temperature ( $\sim 85$  K) TTG measurements were performed under vacuum. The graphite sample was mounted directly to the cold finger of the cryostat. To reduce the anticipated temperature rise (calculated using the pump spot size, optical penetration depth, pulse energy and sample heat capacity) so as to remain within the theoretically predicted hydrodynamic window, the pump power was set to 20 nJ (typical TTG measurements on silicon are conducted with pump powers on the order of 0.2  $\mu$ J [176]). At this pump power, the estimated peak temperature rise is  $\sim 60$  K. However, this consequently reduced the signal-to-noise ratio, thereby requiring the collection of more traces to average over. For the data reported here, each individual grating measurement required 24 to 48 hours to collect 1000 to 2000 traces. Effects of the pump and probe power were investigated and are reported in the Appendix C. For graphite, since the dominant contribution to the thermal signal is the displacement due to thermal expansion, measurements were conducted in the phase grating mode of TTG operation. This was confirmed by performing an amplitude grating measurement for a single grating (not shown). The absence of SAW contributions to the phase grating signal is attributed to the lack of in-plane displacement generated during the excitation due to the unique anisotropy of the

thermal expansion coefficients [177].

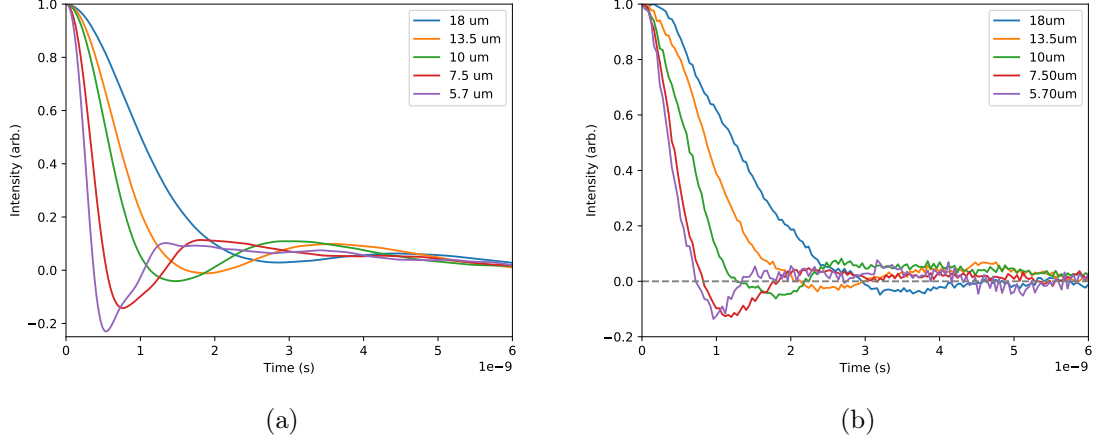


Figure 5-11: (a) Theoretical prediction of the temperature decay in graphite at 80 K as function of grating period in the 1D-TTG geometry. (b) Experimental TTG traces on HOPG at  $\sim 85$  K as a function of grating period.

Figure 5-11 summarizes the theoretical predictions and the experimental measurements of the temperature response in 1D-TTG for HOPG. A clear flipping of  $\delta T$  is observed, indicating that transport occurs within the hydrodynamic regime. As was done to estimate the second sound speed from the theoretical predictions, the extracted experimental second speed for graphite at liquid nitrogen temperature is  $\sim 3400$  m/s. A plausible explanation for the discrepancy between theory and experiment is the lack of orientation between the graphene layers of the actual sample as compared with the A-B-A-B stacking that is necessarily assumed in the DFT calculations in order to obtain the force constants.

The damping time constant,  $\tau_{II}$ , can be extracted by fitting an exponential envelop to the  $\delta T$  signal. However, like the decay times that were observed in the size effect study presented in Chapter 4,  $\tau_{II}$  is non-trivial function of the grating period. For a grating period of  $7.5 \mu\text{m}$ , fitting yields a  $\tau_{II} \sim 0.7$  ns and the propagation length of the temperature wave is then  $v_{II}\tau_{II} \sim 2.5 \mu\text{m}$ .

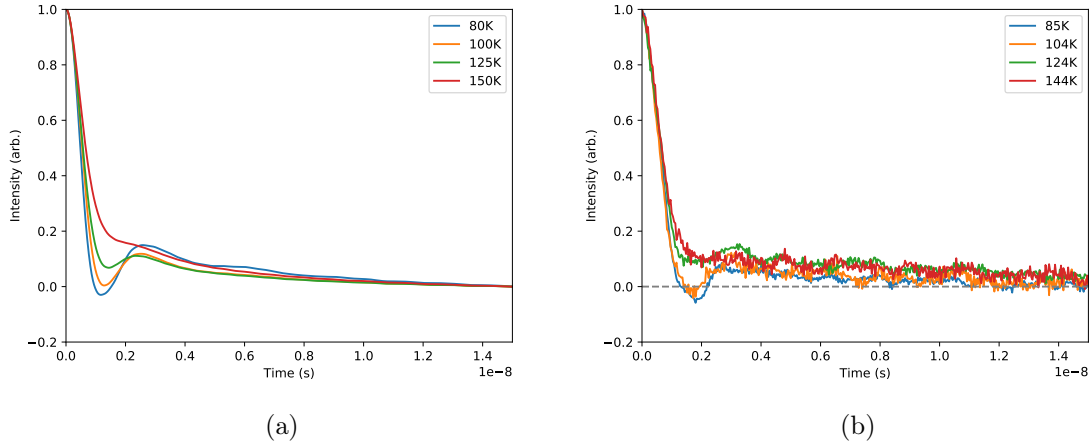


Figure 5-12: (a) Theoretical prediction of the temperature decay in graphite as function of temperature in the 1D-TTG geometry for a  $10.0 \mu\text{m}$  grating period. (b) Experimental TTG traces on HOPG for a  $10.0 \mu\text{m}$  grating period at  $\sim 85 \text{ K}$ , at  $\sim 104 \text{ K}$ , at  $\sim 124 \text{ K}$  and at  $\sim 144 \text{ K}$ .

To provide further empirical evidence for observation of hydrodynamic transport in graphite, preliminary temperature dependent measurements were performed so as to, when combined with the grating dependent traces, fully characterize the hydrodynamic window. Figure 5-12a shows theoretical traces for graphite as a function temperature for a fixed grating. Figure 5-12b is the experimental equivalent of Figure 5-12a, where promising agreement with theory is observed. Future experiments on different graphite samples will be necessary in order to explain the quantitative differences between theory and experiment.

### 5.4.2 Conclusion

In conclusion, we have developed a framework to predict the temperature solution to the LBTE in the linear temperature rise regime using a full collision matrix constructed from ab-initio calculations for any heating profile geometry where boundaries are neglected. This exact solution can serve as a benchmark to study the validity of the RTA or Callaway kernels for a variety of materials not only for bulk transport, but also in the nondiffusive and hydrodynamic thermal transport regimes. For instance, recent work has relied heavily on the Callaway kernel [171, 173] to simulate phonon

Poiseuille flow. The LBTE framework presented here can naturally be incorporated into multiscale BTE solvers where boundaries are accounted for, enabling the study of phonon Poiseuille flow [178].

Using this framework, we calculated the windows of the phonon hydrodynamic regime for graphene and graphite. We validated the theory with experimental measurements on HOPG at liquid nitrogen temperatures where clear signatures of hydrodynamic transport were observed. While quantitative differences between observables calculated from theory and measured in experiment are found, the theory proved extremely useful in guiding experiment. Future measurements on other materials are necessary to illuminate the precise reasons for these differences.



# Chapter 6

## Conclusions and outlook

The three major contributions of this thesis are:

- The experimental demonstration of reversible bi-directional tuning of thermal conductivity at room temperature in an oxide system (see Chapter 3).
- The unification of theory and experiment to enable the use of reflection mode TTG as a platform for studying size effects on thermal transport (see Chapter 4).
- The development of a theoretical framework that enables the study of non-diffusive and hydrodynamic thermal transport in systems where the RTA fails. Using this theory as a guide, the experimental observation of hydrodynamic transport in graphite was reported (see Chapter 5).

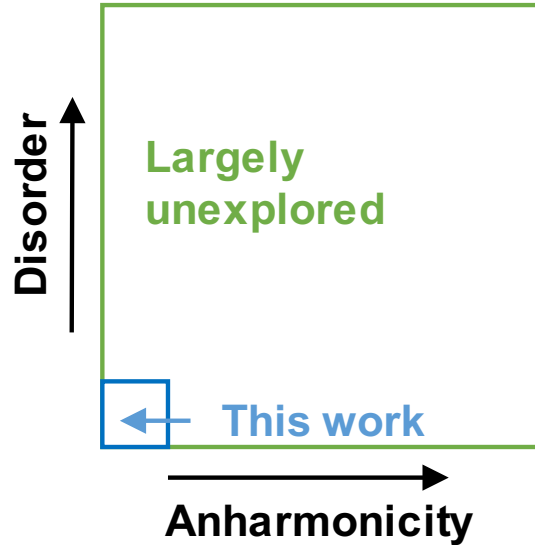


Figure 6-1: The unexplored region.

These achievements are put in perspective in Figure 6-1 and should be considered as incremental steps along the path to answering some of the following questions.

- What is the upper bound on the dynamic range of the tuning of thermal conductivity?
- What is lower bound on the thermal diffusivity of a solid? Recent work from Hartnoll studied the lower bound on electron diffusivity in “incoherent metals”, which are characterized by the breakdown of the quasiparticle picture of transport. In essence, the single electron carrying charge and energy no longer applies. Recent work has shown the breakdown of the phonon and electron picture to describe thermal transport in single crystal  $YBa_2Cu_3O_{6+\delta}$ , and alternatively, the transport is better described by an “incoherent electron-phonon soup” [179]. Past work has demonstrated the breakdown of the phonon picture in crystalline  $Bi_2Sr_2YCu_2O_8$  [180]. Hartnoll proposed the use of the following bound to assess the incoherent regime [27]:

$$D \geq v_s^2 \tau_p \geq v_s^2 \frac{\hbar}{k_B T} \quad (6.1)$$

where  $v_s$  is the speed of sound and  $\tau_p$  is the “Planckian time”, which can be thought of the minimum time that obeys the uncertainty principle for a given thermal energy. If we convert our H-SCO thermal conductivity to thermal diffusivity and use the speed of sound  $\sim 3.76$  km/s [181], we find that H-SCO falls below this bound by  $\sim 50\%$  at room temperature. Does Hartnoll’s conjecture apply to thermal carriers?

- Can hydrodynamic signatures be observed in amorphous solids? Can a “two-fluid” model be used to describe the relationship between the propagating and localized modes?
- Given the recent emergence of work studying electron hydrodynamics [182, 183, 184], it is natural to ask what is the simplest Hamiltonian that can support hydrodynamic transport?
- There has been work using fluids [185, 186, 187] and Bose-Einstein condensates [188] to study Hawking radiation. Can geometries be devised so as to create black hole analogues for the phonon hydrodynamic regime?
- How far does the fluid analogy go? Can a crossover from laminar-like to turbulent-like flow be observed in the phonon hydrodynamic regime? An analogous Reynolds number can be defined as

$$Re = \frac{v_{II}L}{v_g \Lambda_{MFP}} \quad (6.2)$$

where  $v_{II}$  is the speed of second sound,  $L$  is a device length scale, like a grating period or propagation length,  $v_g$  is an average phonon group velocity and  $\Lambda_{MFP}$  an average phonon mean free path. Using properties of graphene at room temperature, we find a  $Re \sim 1$  so it would seem that some fine tuning would be necessary for the observation of turbulence.



# Appendix A

## A.1 TDTR reference data

Table A.1: Thermal properties at 300 K of materials that are used as inputs into the thermal model of the TDTR measurements.

Material	Thermal Conductivity [W/m-K]	Heat Capacity [J/m <sup>3</sup> K]
Al	236.9181	2.4969e+06
Al <sub>2</sub> O <sub>3</sub>	35 (30.3 - 41.7)	3.0995e+06
Si	142	1.6531e+06
SrTiO <sub>3</sub>	11.8	2.7109e+06
SrRuO <sub>3</sub>	2.5 (1.3-5.6)	2.3544e+06
La <sub>0.66</sub> Sr <sub>0.33</sub> MnO <sub>3</sub>	1.6	3.7488e+06
LaAlO <sub>3</sub>	14.5	2.8204e+06
BiFeO <sub>3</sub>	1.2(R), 0.7(T)	2.9340e+06
CoFeO <sub>3</sub>	5	3.3164e+06
YSZ	1.8	2.7000e+06
SrCoO <sub>x</sub>	0.44-6.58	2.8600e+06



# Appendix B

## B.1 SiGe study supplementary material

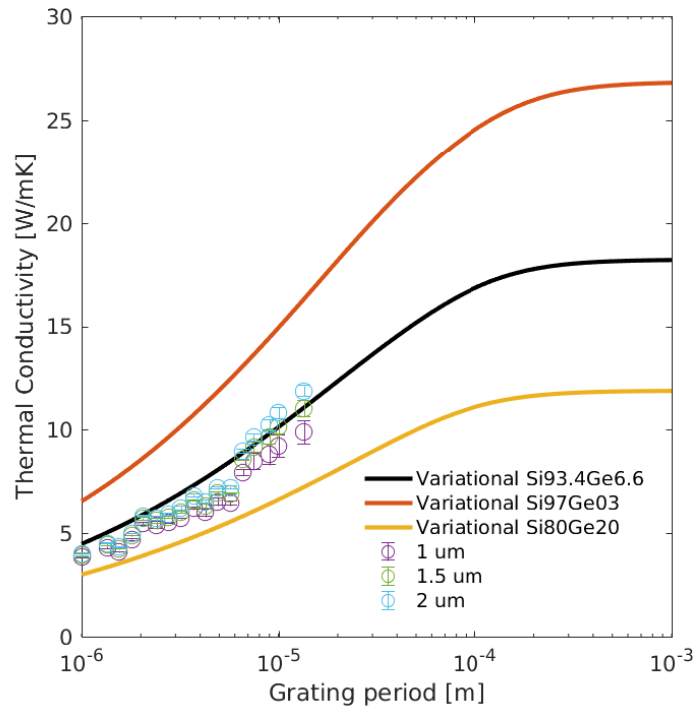


Figure B-1: Effect of uncertainty in the optical penetration depth ( $1, 1.5$  and  $2 \mu\text{m}$ ) on the measurement of effective thermal conductivity with TTG. The error is larger for larger grating periods, as the transport transitions into the  $q/\beta \ll 1$  regime.

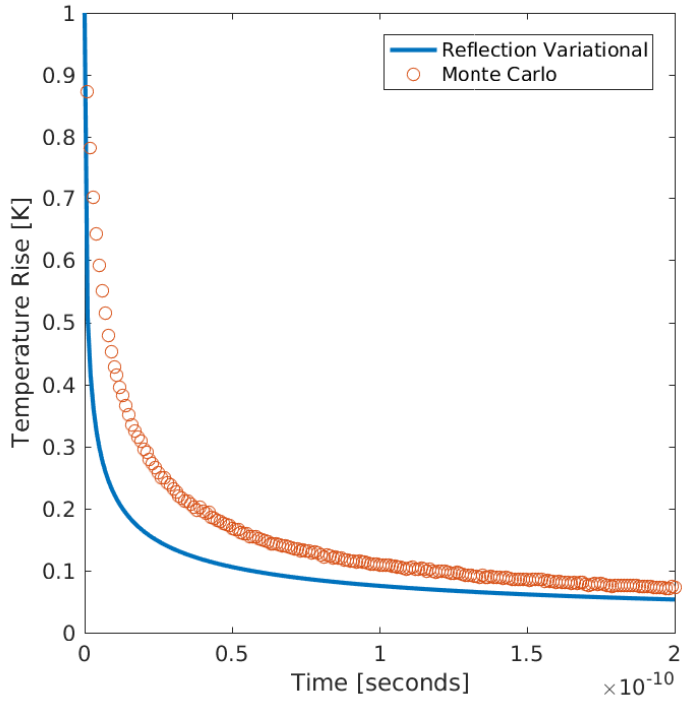


Figure B-2: Monte Carlo simulation of reflection TTG geometry for Si with grating period of 10 um and optical penetration depth of 10 nm. This example demonstrates the limitations of a modified Fourier treatment, independent of the variational framework. No theory based upon a Fourier model will capture this behavior because a time-dependent thermal conductivity is required to do so and the interpretation of such a quantity can only be phenomenologically understood. However, the variational approach can provide a quantitative measure of the extent of this failure. For instance, one could substitute the variational temperature decay back into the BTE (Eq. 15 in the main text) and calculate the difference between the left and right hand side of the equation as a proxy for the error. Another possible avenue is to test the performance of the ballistic solution for the geometry as the trial solution.

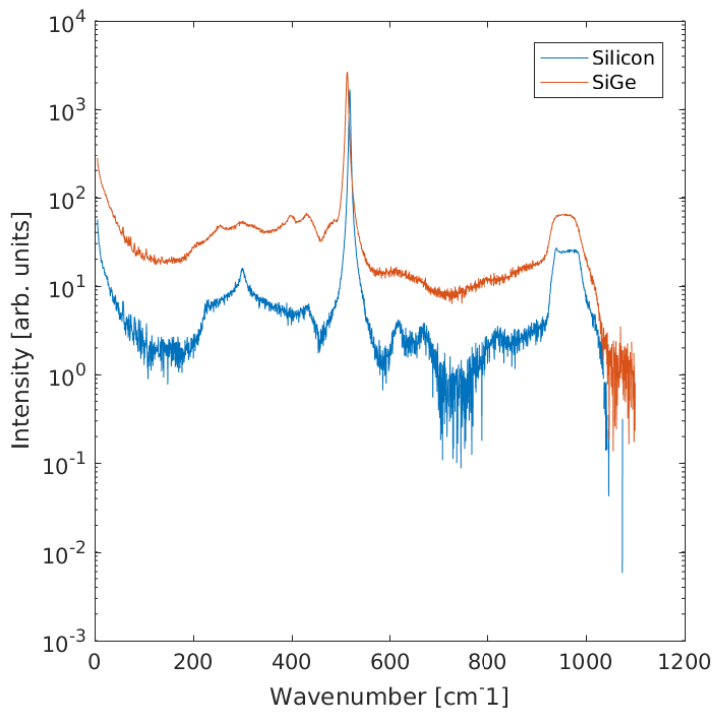


Figure B-3: Raman spectra for Si and  $\text{Si}_{93.4}\text{Ge}_{6.6}$ . A dominant peak is found at  $520 \text{ cm}^{-1}$  for Si and at  $513 \text{ cm}^{-1}$  for  $\text{Si}_{93.4}\text{Ge}_{6.6}$ . As noted in the main text, the DFT-based virtual crystal approximation predicts a single peak at  $488 \text{ cm}^{-1}$  for  $\text{Si}_{93.4}\text{Ge}_{6.6}$ , but not is capable of capturing the peaks near  $400 \text{ cm}^{-1}$ .

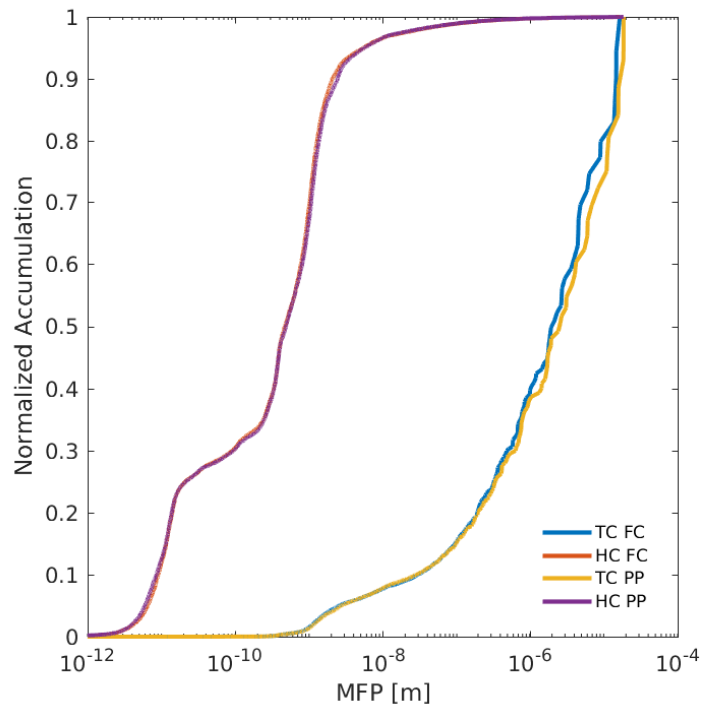


Figure B-4: DFT comparison between averaging force constants, using the (Si,Ge).pz-bhs.UPF set of pseudopotentials (denoted by FC), and averaging pseudopotentials (denoted by PP) through the virtual.x program, using the (Si,Ge).pz-n-nc.UPF set of pseudopotentials. TC denotes the thermal conductivity accumulation function and HC denotes the heat capacity accumulation function.

# Appendix C

## C.1 Hydrodynamic study supplementary material

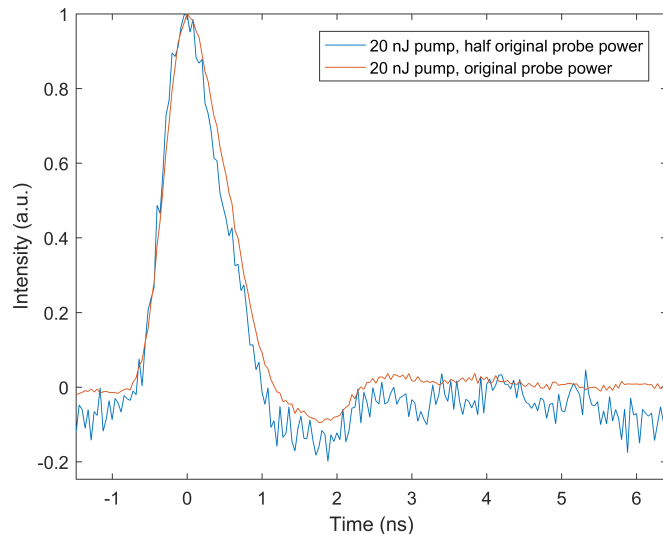


Figure C-1: Effect of probe power in low temperature graphite TTG measurements.

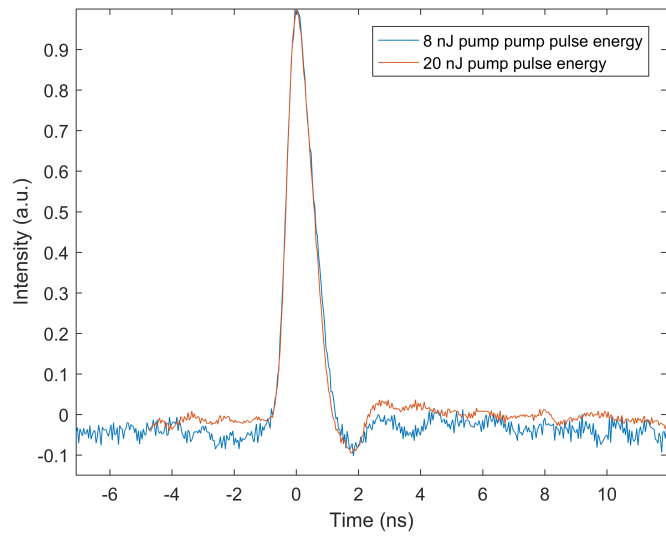


Figure C-2: Effect of pump power in low temperature graphite TTG measurements.

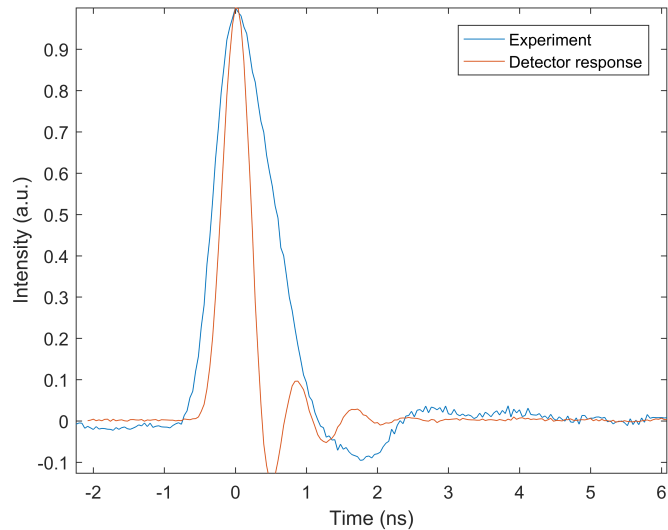


Figure C-3: Comparison between the detector response and a representative low temperature graphite TTG measurements.

# Bibliography

- [1] Samuel Huberman, Vazrik Chiloyan, Ryan A Duncan, Lingping Zeng, Roger Jia, Alexei A Maznev, Eugene A Fitzgerald, Keith A Nelson, and Gang Chen. Unifying first-principles theoretical predictions and experimental measurements of size effects in thermal transport in sige alloys. *Physical Review Materials*, 1(5):054601, 2017.
- [2] Shuai Ning, Samuel C Huberman, Chen Zhang, Zhengjun Zhang, Gang Chen, and Caroline A Ross. Dependence of the thermal conductivity of bifeo 3 thin films on polarization and structure. *Physical Review Applied*, 8(5):054049, 2017.
- [3] Vazrik Chiloyan, Lingping Zeng, Samuel Huberman, Alexei A Maznev, Keith A Nelson, and Gang Chen. Variational approach to extracting the phonon mean free path distribution from the spectral boltzmann transport equation. *Physical Review B*, 93(15):155201, 2016.
- [4] Rudolf Peierls. Zur kinetischen theorie der wärmeleitung in kristallen. *Annalen der Physik*, 395(8):1055–1101, 1929.
- [5] PG Klemens. The thermal conductivity of dielectric solids at low temperatures (theoretical). *Proc. R. Soc. Lond. A*, 208(1092):108–133, 1951.
- [6] Joseph Callaway. Model for lattice thermal conductivity at low temperatures. *Physical Review*, 113(4):1046, 1959.
- [7] HBG Casimir. Note on the conduction of heat in crystals. *Physica*, 5(6):495–500, 1938.
- [8] ASME Majumdar. Microscale heat conduction in dielectric thin films. *Journal of Heat Transfer*, 115(1):7–16, 1993.
- [9] Gang Chen. Ballistic-diffusive heat-conduction equations. *Physical Review Letters*, 86(11):2297, 2001.
- [10] Eric T Swartz and Robert O Pohl. Thermal boundary resistance. *Reviews of modern physics*, 61(3):605, 1989.
- [11] David G Cahill, Wayne K Ford, Kenneth E Goodson, Gerald D Mahan, Arun Majumdar, Humphrey J Maris, Roberto Merlin, and Simon R Phillpot. Nanoscale thermal transport. *Journal of applied physics*, 93(2):793–818, 2003.

- [12] Alexei A Maznev, Jeremy A Johnson, and Keith A Nelson. Onset of nondiffusive phonon transport in transient thermal grating decay. *Physical Review B*, 84(19):195206, 2011.
- [13] Kimberlee C Collins, Alexei A Maznev, Zhitong Tian, Keivan Esfarjani, Keith A Nelson, and Gang Chen. Non-diffusive relaxation of a transient thermal grating analyzed with the boltzmann transport equation. *Journal of Applied Physics*, 114(10):104302, 2013.
- [14] Sebastian G Volz and Gang Chen. Molecular dynamics simulation of thermal conductivity of silicon nanowires. *Applied Physics Letters*, 75(14):2056–2058, 1999.
- [15] PK Schelling, SR Phillpot, and P Kebinski. Phonon wave-packet dynamics at semiconductor interfaces by molecular-dynamics simulation. *Applied Physics Letters*, 80(14):2484–2486, 2002.
- [16] DA Broido, Michael Malorny, Gerd Birner, Natalio Mingo, and DA Stewart. Intrinsic lattice thermal conductivity of semiconductors from first principles. *Applied Physics Letters*, 91(23):231922, 2007.
- [17] Keivan Esfarjani, Gang Chen, and Harold T Stokes. Heat transport in silicon from first-principles calculations. *Physical Review B*, 84(8):085204, 2011.
- [18] David G Cahill, Kenneth Goodson, and Arunava Majumdar. Thermometry and thermal transport in micro/nanoscale solid-state devices and structures. *Journal of Heat Transfer*, 124(2):223–241, 2002.
- [19] OW Käding, H Skurk, AA Maznev, and E Matthias. Transient thermal gratings at surfaces for thermal characterization of bulk materials and thin films. *Applied Physics A*, 61(3):253–261, 1995.
- [20] Lingping Zeng, Kimberlee C Collins, Yongjie Hu, Maria N Luckyanova, Alexei A Maznev, Samuel Huberman, Vazrik Chiloyan, Jiawei Zhou, Xiaopeng Huang, Keith A Nelson, et al. Measuring phonon mean free path distributions by probing quasiballistic phonon transport in grating nanostructures. *Scientific reports*, 5:17131–17131, 2014.
- [21] F Bencivenga, R Cucini, Flavio Capotondi, A Battistoni, R Mincigrucci, E Giangrisostomi, A Gessini, M Manfredda, IP Nikolov, E Pedersoli, et al. Four-wave mixing experiments with extreme ultraviolet transient gratings. *Nature*, 520(7546):205, 2015.
- [22] David G Cahill and Robert O Pohl. Thermal conductivity of amorphous solids above the plateau. *Physical review B*, 35(8):4067, 1987.
- [23] Sajal Dhara, Hari S Solanki, Vibhor Singh, Shamashis Sengupta, BA Chalke, Abhishek Dhar, Mahesh Gokhale, Arnab Bhattacharya, Mandar M Deshmukh,

et al. Tunable thermal conductivity in defect engineered nanowires at low temperatures. *Physical Review B*, 84(12):121307, 2011.

- [24] Tae-Youl Choi, Dimos Poulikakos, Joy Tharian, and Urs Sennhauser. Measurement of the thermal conductivity of individual carbon nanotubes by the four-point three- $\omega$  method. *Nano letters*, 6(8):1589–1593, 2006.
- [25] Andrea Cepellotti, Giorgia Fugallo, Lorenzo Paulatto, Michele Lazzeri, Francesco Mauri, and Nicola Marzari. Phonon hydrodynamics in two-dimensional materials. *Nature communications*, 6:6400, 2015.
- [26] Sangyeop Lee, David Broido, Keivan Esfarjani, and Gang Chen. Hydrodynamic phonon transport in suspended graphene. *Nature communications*, 6:6290, 2015.
- [27] Sean A Hartnoll. Theory of universal incoherent metallic transport. *Nature Physics*, 11(1):54, 2015.
- [28] Terumasa Tadano and Shinji Tsuneyuki. First-principles lattice dynamics method for strongly anharmonic crystals. *Journal of the Physical Society of Japan*, 87(4):041015, 2018.
- [29] John M Ziman. *Electrons and phonons: the theory of transport phenomena in solids*. Oxford university press, 1960.
- [30] Gyaneshwar P Srivastava. *The physics of phonons*. CRC press, 1990.
- [31] Herbert Spohn. The phonon boltzmann equation, properties and link to weakly anharmonic lattice dynamics. *Journal of statistical physics*, 124(2-4):1041–1104, 2006.
- [32] Aleksei Viktorovich Bolsinov and Anatolij Timofeevič Fomenko. *Integrable Hamiltonian systems: geometry, topology, classification*. CRC Press, 2004.
- [33] Tomaž Prosen and David K Campbell. Momentum conservation implies anomalous energy transport in 1d classical lattices. *Physical review letters*, 84(13):2857, 2000.
- [34] Bambi Hu, Baowen Li, and Hong Zhao. Heat conduction in one-dimensional nonintegrable systems. *Physical Review E*, 61(4):3828, 2000.
- [35] RL Dobrushin, A Pellegrinotti, Yu M Suhov, and L Triolo. One-dimensional harmonic lattice caricature of hydrodynamics. *Journal of statistical physics*, 43(3-4):571–607, 1986.
- [36] Christian B Mendl, Jianfeng Lu, and Jani Lukkarinen. Thermalization of oscillator chains with onsite anharmonicity and comparison with kinetic theory. *Physical Review E*, 94(6):062104, 2016.

- [37] Federico Bonetto, Joel L Lebowitz, and Luc Rey-Bellet. Fourier's law: a challenge to theorists. In *Mathematical physics 2000*, pages 128–150. World Scientific, 2000.
- [38] Joseph Ford. The fermi-pasta-ulam problem: paradox turns discovery. *Physics Reports*, 213(5):271–310, 1992.
- [39] Raffaele Guido Della Valle and Piero Procacci. Equation of motion for the greenâs function in anharmonic solids. *Physical Review B*, 46(10):6141, 1992.
- [40] KH Michel, P Scuracchio, and FM Peeters. Sound waves and flexural mode dynamics in two-dimensional crystals. *Physical Review B*, 96(9):094302, 2017.
- [41] Alan McGaughey and Jason M Larkin. Predicting phonon properties from equilibrium molecular dynamics simulations. *Ann. Rev. Heat Transfer*, 17:49–87, 2014.
- [42] JE Turney, ES Landry, AJH McGaughey, and CH Amon. Predicting phonon properties and thermal conductivity from anharmonic lattice dynamics calculations and molecular dynamics simulations. *Physical Review B*, 79(6):064301, 2009.
- [43] Wu Li, Jesús Carrete, Nabil A Katcho, and Natalio Mingo. Shengbte: A solver of the boltzmann transport equation for phonons. *Computer Physics Communications*, 185(6):1747–1758, 2014.
- [44] Atsushi Togo and Isao Tanaka. First principles phonon calculations in materials science. *Scripta Materialia*, 108:1–5, 2015.
- [45] Joel L Lebowitz. Statistical mechanics: A selective review of two central issues. In *More Things in Heaven and Earth*, pages 581–600. Springer, 1999.
- [46] Rahul Nandkishore and David A Huse. Many-body localization and thermalization in quantum statistical mechanics. *Annu. Rev. Condens. Matter Phys.*, 6(1):15–38, 2015.
- [47] Qing Hao, Gang Chen, and Ming-Shan Jeng. Frequency-dependent monte carlo simulations of phonon transport in two-dimensional porous silicon with aligned pores. *Journal of Applied Physics*, 106(11):114321, 2009.
- [48] AA Maznev and OB Wright. Demystifying umklapp vs normal scattering in lattice thermal conductivity. *American journal of physics*, 82(11):1062–1066, 2014.
- [49] Michael Polyak. Feynman diagrams for pedestrians and mathematicians. *Graphs and patterns in mathematics and theoretical physics*, 73:15–42, 2005.
- [50] Laurent Chaput, Atsushi Togo, Isao Tanaka, and Gilles Hug. Phonon-phonon interactions in transition metals. *Physical Review B*, 84(9):094302, 2011.

- [51] Kedar Damle and Subir Sachdev. Nonzero-temperature transport near quantum critical points. *Physical Review B*, 56(14):8714, 1997.
- [52] W Götze and KH Michel. First and second sound in crystals. *Physical Review*, 156(3):963, 1967.
- [53] Jean-Philippe M Péraud and Nicolas G Hadjiconstantinou. Efficient simulation of multidimensional phonon transport using energy-based variance-reduced monte carlo formulations. *Physical Review B*, 84(20):205331, 2011.
- [54] Jean-Philippe M Péraud and Nicolas G Hadjiconstantinou. An alternative approach to efficient simulation of micro/nanoscale phonon transport. *Applied Physics Letters*, 101(15):153114, 2012.
- [55] Aaron J Schmidt, Xiaoyuan Chen, and Gang Chen. Pulse accumulation, radial heat conduction, and anisotropic thermal conductivity in pump-probe transient thermoreflectance. *Review of Scientific Instruments*, 79(11):114902, 2008.
- [56] Yongjie Hu, Lingping Zeng, Austin J Minnich, Mildred S Dresselhaus, and Gang Chen. Spectral mapping of thermal conductivity through nanoscale ballistic transport. *Nature nanotechnology*, 10(8):701–706, 2015.
- [57] AA Maznev, KA Nelson, and JA Rogers. Optical heterodyne detection of laser-induced gratings. *Optics letters*, 23(16):1319–1321, 1998.
- [58] Jeremy A Johnson, Alexei A Maznev, Mayank T Bulsara, Eugene A Fitzgerald, TC Harman, S Calawa, CJ Vineis, G Turner, and Keith A Nelson. Phase-controlled, heterodyne laser-induced transient grating measurements of thermal transport properties in opaque material. *Journal of Applied Physics*, 111(2):023503, 2012.
- [59] A Vega-Flick, JK Eliason, AA Maznev, A Khanolkar, M Abi Ghanem, N Boehler, JJ Alvarado-Gil, and KA Nelson. Laser-induced transient grating setup with continuously tunable period. *Review of Scientific Instruments*, 86(12):123101, 2015.
- [60] B Abeles. Lattice thermal conductivity of disordered semiconductor alloys at high temperatures. *Physical Review*, 131(5):1906, 1963.
- [61] PG Klemens. Thermal resistance due to point defects at high temperatures. *Physical review*, 119(2):507, 1960.
- [62] Joseph Callaway and Hans C von Baeyer. Effect of point imperfections on lattice thermal conductivity. *Physical Review*, 120(4):1149, 1960.
- [63] Shin-ichiro Tamura. Isotope scattering of dispersive phonons in ge. *Physical Review B*, 27(2):858, 1983.

- [64] XW Wang, H Lee, YC Lan, GH Zhu, G Joshi, DZ Wang, J Yang, AJ Muto, MY Tang, J Klatsky, et al. Enhanced thermoelectric figure of merit in nanostructured n-type silicon germanium bulk alloy. *Applied Physics Letters*, 93(19):193121, 2008.
- [65] Jaime Andres Perez-Taborda, Miguel Muñoz Rojo, Jon Maiz, Neophytos Neophytou, and Marisol Martin-Gonzalez. Ultra-low thermal conductivities in large-area si-ge nanomeshes for thermoelectric applications. *Scientific reports*, 6:32778, 2016.
- [66] Xin Qian, Xiaokun Gu, Mildred S Dresselhaus, and Ronggui Yang. Anisotropic tuning of graphite thermal conductivity by lithium intercalation. *The journal of physical chemistry letters*, 7(22):4744–4750, 2016.
- [67] Gaohua Zhu, Jun Liu, Qiye Zheng, Ruigang Zhang, Dongyao Li, Debasish Banerjee, and David G Cahill. Tuning thermal conductivity in molybdenum disulfide by electrochemical intercalation. *Nature communications*, 7:13211, 2016.
- [68] Jung Cho, Mark D Losego, Hui Gang Zhang, Honggyu Kim, Jianmin Zuo, Ivan Petrov, David G Cahill, and Paul V Braun. Electrochemically tunable thermal conductivity of lithium cobalt oxide. *Nature communications*, 5:4035, 2014.
- [69] Xuewang Wu, Jeff Walter, Tianli Feng, Jie Zhu, Hong Zheng, John F Mitchell, Neven Biškup, Maria Varela, Xiulin Ruan, Chris Leighton, et al. Glass-like through-plane thermal conductivity induced by oxygen vacancies in nanoscale epitaxial  $\text{La}_{0.5}\text{Sr}_{0.5}\text{CoO}_3-\delta$ . *Advanced Functional Materials*, 27(47), 2017.
- [70] Maria N Luckyanova, Di Chen, Wen Ma, Harry L Tuller, Gang Chen, and Bilge Yildiz. Thermal conductivity control by oxygen defect concentration modification in reducible oxides: The case of  $\text{Pr}_{0.1}\text{Ce}_{0.9}\text{O}_{2-\delta}$  thin films. *Applied Physics Letters*, 104(6):061911, 2014.
- [71] Kevin D Parrish, Ankit Jain, Jason M Larkin, Wissam A Saidi, and Alan JH McGaughey. Origins of thermal conductivity changes in strained crystals. *Physical Review B*, 90(23):235201, 2014.
- [72] Hinako Kizuka, Takashi Yagi, Junjun Jia, Yuichiro Yamashita, Shinichi Nakamura, Naoyuki Taketoshi, and Yuzo Shigesato. Temperature dependence of thermal conductivity of  $\text{VO}_2$  thin films across metal–insulator transition. *Japanese Journal of Applied Physics*, 54(5):053201, 2015.
- [73] Jon F Ihlefeld, Brian M Foley, David A Scrymgeour, Joseph R Michael, Bonnie B McKenzie, Douglas L Medlin, Margeaux Wallace, Susan Trolier-McKinstry, and Patrick E Hopkins. Room-temperature voltage tunable phonon thermal conductivity via reconfigurable interfaces in ferroelectric thin films. *Nano letters*, 15(3):1791–1795, 2015.

- [74] Juan Antonio Seijas-Bellido, Carlos Escorihuela-Sayalero, Miquel Royo, Mathias P Ljungberg, Jacek C Wojdeł, Jorge Íñiguez, and Riccardo Ruralli. A phononic switch based on ferroelectric domain walls. *Physical Review B*, 96(14):140101, 2017.
- [75] T Zhao, A Scholl, F Zavaliche, K Lee, M Barry, A Doran, MP Cruz, YH Chu, C Ederer, NA Spaldin, et al. Electrical control of antiferromagnetic domains in multiferroic bifeo 3 films at room temperature. *Nature materials*, 5(10):823, 2006.
- [76] Gustau Catalan and James F Scott. Physics and applications of bismuth ferrite. *Advanced Materials*, 21(24):2463–2485, 2009.
- [77] Y-H Chu, Maria P Cruz, C-H Yang, Lane W Martin, P-L Yang, J-X Zhang, Kilho Lee, Pu Yu, L-Q Chen, and Ramamoorthy Ramesh. Domain control in multiferroic bifeo<sub>3</sub> through substrate vicinality. *Advanced materials*, 19(18):2662–2666, 2007.
- [78] Ying-Hao Chu, Qing He, Chan-Ho Yang, Pu Yu, Lane W Martin, Padraic Shafer, and R Ramesh. Nanoscale control of domain architectures in bifeo<sub>3</sub> thin films. *Nano letters*, 9(4):1726–1730, 2009.
- [79] Morgan Trassin, Gabriele De Luca, Sebastian Manz, and Manfred Fiebig. Probing ferroelectric domain engineering in bifeo<sub>3</sub> thin films by second harmonic generation. *Advanced Materials*, 27(33):4871–4876, 2015.
- [80] RJ Zeches, MD Rossell, JX Zhang, AJ Hatt, Q He, C-H Yang, A Kumar, CH Wang, A Melville, C Adamo, et al. A strain-driven morphotropic phase boundary in bifeo<sub>3</sub>. *science*, 326(5955):977–980, 2009.
- [81] Hans M Christen, Joong Hee Nam, Hyun Sik Kim, Alison J Hatt, and Nicola A Spaldin. Stress-induced r- m a- m c- t symmetry changes in bifeo 3 films. *Physical Review B*, 83(14):144107, 2011.
- [82] MN Iliev, MV Abrashev, D Mazumdar, V Shelke, and A Gupta. Polarized raman spectroscopy of nearly tetragonal bifeo 3 thin films. *Physical Review B*, 82(1):014107, 2010.
- [83] Christianne Beekman, Wolter Siemons, Thomas Z Ward, Miaofang Chi, J Howe, Michael D Biegalski, Nina Balke, Petro Maksymovych, AK Farrar, JB Romero, et al. Phase transitions, phase coexistence, and piezoelectric switching behavior in highly strained bifeo<sub>3</sub> films. *Advanced Materials*, 25(39):5561–5567, 2013.
- [84] Chung-Hua Chiu, Wen-I Liang, Chun-Wei Huang, Jui-Yuan Chen, Yun-Ya Liu, Jiang-Yu Li, Cheng-Lun Hsin, Ying-Hao Chu, and Wen-Wei Wu. Atomic visualization of the phase transition in highly strained bifeo<sub>3</sub> thin films with excellent pyroelectric response. *Nano Energy*, 17:72–81, 2015.

- [85] Alison J Hatt, Nicola A Spaldin, and Claude Ederer. Strain-induced isosymmetric phase transition in bifeo 3. *Physical Review B*, 81(5):054109, 2010.
- [86] JX Zhang, Q He, M Trassin, W Luo, D Yi, MD Rossell, P Yu, L You, CH Wang, CY Kuo, et al. Microscopic origin of the giant ferroelectric polarization in tetragonal-like bifeo 3. *Physical review letters*, 107(14):147602, 2011.
- [87] Bryan C Gundrum, David G Cahill, and Robert S Averback. Thermal conductance of metal-metal interfaces. *Physical Review B*, 72(24):245426, 2005.
- [88] MJ Highland, TT Fister, DD Fong, PH Fuoss, Carol Thompson, JA Eastman, SK Streiffer, and GB Stephenson. Equilibrium polarization of ultrathin pbtio 3 with surface compensation controlled by oxygen partial pressure. *Physical review letters*, 107(18):187602, 2011.
- [89] RV Wang, DD Fong, F Jiang, MJ Highland, PH Fuoss, Carol Thompson, AM Kolpak, JA Eastman, SK Streiffer, AM Rappe, et al. Reversible chemical switching of a ferroelectric film. *Physical review letters*, 102(4):047601, 2009.
- [90] Matthew J Highland, Timothy T Fister, Marie-Ingrid Richard, Dillon D Fong, Paul H Fuoss, Carol Thompson, Jeffrey A Eastman, Stephen K Streiffer, and G Brian Stephenson. Polarization switching without domain formation at the intrinsic coercive field in ultrathin ferroelectric pbtio 3. *Physical review letters*, 105(16):167601, 2010.
- [91] Dipanjan Mazumdar, Vilas Shelke, Milko Iliev, Stephen Jesse, Amit Kumar, Sergei V Kalinin, Arthur P Baddorf, and Arunava Gupta. Nanoscale switching characteristics of nearly tetragonal bifeo3 thin films. *Nano letters*, 10(7):2555–2561, 2010.
- [92] Heng-Jui Liu, Yu-Hao Du, Peng Gao, Yen-Chin Huang, Hsiao-Wen Chen, Yi-Chun Chen, Hsiang-Lin Liu, Qing He, Yuichi Ikuhara, and Ying-Hao Chu. Tetragonal bifeo3 on yttria-stabilized zirconia. *APL Materials*, 3(11):116104, 2015.
- [93] Joseph Desmarais, Jon F Ihlefeld, Tassilo Heeg, Jürgen Schubert, Darrell G Schlom, and Bryan D Huey. Mapping and statistics of ferroelectric domain boundary angles and types. *Applied physics letters*, 99(16):162902, 2011.
- [94] Patrick E Hopkins, Carolina Adamo, Linghan Ye, Bryan D Huey, Stephen R Lee, Darrell G Schlom, and Jon F Ihlefeld. Effects of coherent ferroelastic domain walls on the thermal conductivity and kapitza conductance in bismuth ferrite. *Applied Physics Letters*, 102(12):121903, 2013.
- [95] SH Baek, HW Jang, CM Folkman, YL Li, B Winchester, JX Zhang, Q He, YH Chu, CT Nelson, MS Rzchowski, et al. Ferroelastic switching for nanoscale non-volatile magnetoelectric devices. *Nature materials*, 9(4):309, 2010.

- [96] Florin Zavaliche, P Shafer, R Ramesh, MP Cruz, RR Das, DM Kim, and CB Eom. Polarization switching in epitaxial bi fe o 3 films. *Applied physics letters*, 87(25):252902, 2005.
- [97] MP Cruz, YH Chu, JX Zhang, PL Yang, F Zavaliche, Q He, P Shafer, LQ Chen, and R Ramesh. Strain control of domain-wall stability in epitaxial bifeo 3 (110) films. *Physical review letters*, 99(21):217601, 2007.
- [98] Qiyang Lu, Yan Chen, Hendrik Bluhm, and Bilge Yildiz. Electronic structure evolution of srcoo x during electrochemically driven phase transition probed by in situ x-ray spectroscopy. *The Journal of Physical Chemistry C*, 120(42):24148–24157, 2016.
- [99] Qiyang Lu and Bilge Yildiz. Voltage-controlled topotactic phase transition in thin-film srcoo x monitored by in situ x-ray diffraction. *Nano letters*, 16(2):1186–1193, 2016.
- [100] Hyoungjeen Jeen, Woo Seok Choi, Michael D Biegalski, Chad M Folkman, I-Cheng Tung, Dillon D Fong, John W Freeland, Dongwon Shin, Hiromichi Ohta, Matthew F Chisholm, et al. Reversible redox reactions in an epitaxially stabilized srcoo x oxygen sponge. *Nature materials*, 12(11):1057, 2013.
- [101] Nianpeng Lu, Pengfei Zhang, Qinghua Zhang, Ruimin Qiao, Qing He, Hao-Bo Li, Yujia Wang, Jingwen Guo, Ding Zhang, Zheng Duan, et al. Electric-field control of tri-state phase transformation with a selective dual-ion switch. *Nature*, 546(7656):124, 2017.
- [102] Woo Seok Choi, Hyoungjeen Jeen, Jun Hee Lee, SS Ambrose Seo, Valentino R Cooper, Karin M Rabe, and Ho Nyung Lee. Reversal of the lattice structure in srcoo x epitaxial thin films studied by real-time optical spectroscopy and first-principles calculations. *Physical review letters*, 111(9):097401, 2013.
- [103] Keun Hyung Lee, Moon Sung Kang, Sipei Zhang, Yuanyan Gu, Timothy P Lodge, and C Daniel Frisbie. ácut and stickâ rubbery ion gels as high capacitance gate dielectrics. *Advanced Materials*, 24(32):4457–4462, 2012.
- [104] Ambroise van Roekeghem, Jesús Carrete, Corey Osse, Stefano Curtarolo, and Natalio Mingo. High-throughput computation of thermal conductivity of high-temperature solid phases: the case of oxide and fluoride perovskites. *Physical Review X*, 6(4):041061, 2016.
- [105] Eric S Toberer, Lauryn L Baranowski, and Chris Dames. Advances in thermal conductivity. *Annual Review of Materials Research*, 42:179–209, 2012.
- [106] Guofa Cai, Jiangxin Wang, and Pooi See Lee. Next-generation multifunctional electrochromic devices. *Accounts of chemical research*, 49(8):1469–1476, 2016.

- [107] John Cuffe, Jeffrey K Eliason, Alexei A Maznev, Kimberlee C Collins, Jeremy A Johnson, Andrey Shchepetov, Mika Prunnila, Jouni Ahopelto, Clivia M Sotomayor Torres, Gang Chen, et al. Reconstructing phonon mean-free-path contributions to thermal conductivity using nanoscale membranes. *Physical Review B*, 91(24):245423, 2015.
- [108] Jeremy A Johnson, Jeffrey K Eliason, Alexei A Maznev, Tengfei Luo, and Keith A Nelson. Non-diffusive thermal transport in gaas at micron length scales. *Journal of Applied Physics*, 118(15):155104, 2015.
- [109] H Stohr and W Klemm. On two-component systems with germanium i germanium/aluminium, germanium/tin and germanium/silicon. *Z. Anorg. Chem.*, 241:305, 1939.
- [110] Arnold M Toxen. Lattice thermal conductivity of germanium-silicon alloy single crystals at low temperatures. *Physical Review*, 122(2):450, 1961.
- [111] B Abeles, DS Beers, G Dr Cody, and JP Dismukes. Thermal conductivity of ge-si alloys at high temperatures. *Physical review*, 125(1):44, 1962.
- [112] Yee Kan Koh and David G Cahill. Frequency dependence of the thermal conductivity of semiconductor alloys. *Physical Review B*, 76(7):075207, 2007.
- [113] Carolina Abs da Cruz, Wu Li, Nabil A Katcho, and Natalio Mingo. Role of phonon anharmonicity in time-domain thermoreflectance measurements. *Applied Physics Letters*, 101(8):083108, 2012.
- [114] Bjorn Vermeersch, Jesus Carrete, Natalio Mingo, and Ali Shakouri. Superdiffusive heat conduction in semiconductor alloys. i. theoretical foundations. *Physical Review B*, 91(8):085202, 2015.
- [115] Bjorn Vermeersch, Amr MS Mohammed, Gilles Pernot, Yee Rui Koh, and Ali Shakouri. Superdiffusive heat conduction in semiconductor alloys. ii. truncated lévy formalism for experimental analysis. *Physical Review B*, 91(8):085203, 2015.
- [116] Chengyun Hua, Xiangwen Chen, Navaneetha K Ravichandran, and Austin J Minnich. Experimental metrology to obtain thermal phonon transmission coefficients at solid interfaces. *arXiv preprint arXiv:1612.08401*, 2016.
- [117] RB Wilson and David G Cahill. Anisotropic failure of fourier theory in time-domain thermoreflectance experiments. *Nature communications*, 5, 2014.
- [118] DA Broido, A Ward, and N Mingo. Lattice thermal conductivity of silicon from empirical interatomic potentials. *Physical Review B*, 72(1):014308, 2005.
- [119] Lorenzo Paulatto, Francesco Mauri, and Michele Lazzeri. Anharmonic properties from a generalized third-order ab initio approach: Theory and applications to graphite and graphene. *Physical Review B*, 87(21):214303, 2013.

- [120] Jivtesh Garg, Nicola Bonini, Boris Kozinsky, and Nicola Marzari. Role of disorder and anharmonicity in the thermal conductivity of silicon-germanium alloys: A first-principles study. *Physical review letters*, 106(4):045901, 2011.
- [121] Gabriel Antonius and Steven G Louie. Temperature-induced topological phase transitions: Promoted versus suppressed nontrivial topology. *Physical Review Letters*, 117(24):246401, 2016.
- [122] Tianli Feng, Bo Qiu, and Xiulin Ruan. Coupling between phonon-phonon and phonon-impurity scattering: A critical revisit of the spectral matthiessen's rule. *Physical Review B*, 92(23):235206, 2015.
- [123] DW Feldman, M Ashkin, and James H Parker Jr. Raman scattering by local modes in germanium-rich silicon-germanium alloys. *Physical Review Letters*, 17(24):1209, 1966.
- [124] Zhifeng Sui, Hubert H Burke, and Irving P Herman. Raman scattering in germanium-silicon alloys under hydrostatic pressure. *Physical Review B*, 48(4):2162, 1993.
- [125] Paolo Giannozzi, Stefano Baroni, Nicola Bonini, Matteo Calandra, Roberto Car, Carlo Cavazzoni, Davide Ceresoli, Guido L Chiarotti, Matteo Cococcioni, Ismaila Dabo, et al. Quantum espresso: a modular and open-source software project for quantum simulations of materials. *Journal of physics: Condensed matter*, 21(39):395502, 2009.
- [126] Chengyun Hua and Austin J Minnich. Analytical green's function of the multi-dimensional frequency-dependent phonon boltzmann equation. *Physical Review B*, 90(21):214306, 2014.
- [127] Vazrik Chiloyan, Lingping Zeng, Samuel Huberman, Alexei A Maznev, Keith A Nelson, and Gang Chen. Variational approach to solving the spectral boltzmann transport equation in transient thermal grating for thin films. *Journal of Applied Physics*, 120(2):025103, 2016.
- [128] Fan Yang and Chris Dames. Mean free path spectra as a tool to understand thermal conductivity in bulk and nanostructures. *Physical Review B*, 87(3):035437, 2013.
- [129] Rubin Braunstein, Arnold R Moore, and Frank Herman. Intrinsic optical absorption in germanium-silicon alloys. *Physical Review*, 109(3):695, 1958.
- [130] MT Currie, SB Samavedam, TA Langdo, CW Leitz, and EA Fitzgerald. Controlling threading dislocation densities in ge on si using graded sige layers and chemical-mechanical polishing. *Applied Physics Letters*, 72(14):1718–1720, 1998.
- [131] RB Wilson and David G Cahill. Limits to fourier theory in high thermal conductivity single crystals. *Applied Physics Letters*, 107(20):203112, 2015.

- [132] Ding Ding, Xiangwen Chen, and AJ Minnich. Radial quasiballistic transport in time-domain thermoreflectance studied using monte carlo simulations. *Applied Physics Letters*, 104(14):143104, 2014.
- [133] Bjorn Vermeersch and Ali Shakouri. Limitations of generalised grey phonon models for quasiballistic thermal transport in time-periodic regimes. *arXiv preprint arXiv:1602.05387*, 2016.
- [134] Jeffrey L Braun and Patrick E Hopkins. Upper limit to the thermal penetration depth during modulated heating of multilayer thin films with pulsed and continuous wave lasers: A numerical study. *Journal of Applied Physics*, 121(17):175107, 2017.
- [135] Austin J Minnich. Determining phonon mean free paths from observations of quasiballistic thermal transport. *Physical review letters*, 109(20):205901, 2012.
- [136] KT Regner, Alan JH McGaughey, and Jonathan A Malen. Analytical interpretation of nondiffusive phonon transport in thermoreflectance thermal conductivity measurements. *Physical Review B*, 90(6):064302, 2014.
- [137] Takashi Fuyuki, Hayato Kondo, Tsutomu Yamazaki, Yu Takahashi, and Yukiharu Uraoka. Photographic surveying of minority carrier diffusion length in polycrystalline silicon solar cells by electroluminescence. *Applied Physics Letters*, 86(26):262108, 2005.
- [138] M Omini and A Sparavigna. An iterative approach to the phonon boltzmann equation in the theory of thermal conductivity. *Physica B: Condensed Matter*, 212(2):101–112, 1995.
- [139] Giorgia Fugallo, Michele Lazzeri, Lorenzo Paulatto, and Francesco Mauri. Ab initio variational approach for evaluating lattice thermal conductivity. *Physical Review B*, 88(4):045430, 2013.
- [140] Andrea Cepellotti and Nicola Marzari. Thermal transport in crystals as a kinetic theory of relaxons. *Physical Review X*, 6(4):041013, 2016.
- [141] Andrea Cepellotti and Nicola Marzari. Boltzmann transport in nanostructures as a friction effect. *Nano letters*, 17(8):4675–4682, 2017.
- [142] Lingping Zeng, Vazrik Chiloyan, Samuel Huberman, Alex A Maznev, Jean-Philippe M Peraud, Nicolas G Hadjiconstantinou, Keith A Nelson, and Gang Chen. Monte carlo study of non-diffusive relaxation of a transient thermal grating in thin membranes. *Applied Physics Letters*, 108(6):063107, 2016.
- [143] Gang Chen. *Nanoscale energy transport and conversion: a parallel treatment of electrons, molecules, phonons, and photons*. Oxford University Press, 2005.
- [144] Robert Alan Guyer and JA Krumhansl. Solution of the linearized phonon boltzmann equation. *Physical Review*, 148(2):766, 1966.

- [145] Travis E Oliphant. *A guide to NumPy*, volume 1. Trelgol Publishing USA, 2006.
- [146] L Lindsay, DA Broido, and Natalio Mingo. Flexural phonons and thermal transport in graphene. *Physical Review B*, 82(11):115427, 2010.
- [147] Giorgia Fugallo, Andrea Cepellotti, Lorenzo Paulatto, Michele Lazzeri, Nicola Marzari, and Francesco Mauri. Thermal conductivity of graphene and graphite: collective excitations and mean free paths. *Nano letters*, 14(11):6109–6114, 2014.
- [148] L Tisza. J. de phys. et rad., 1, 165, 350,(1940). *J. de Phys. et rad.*, 1:165, 1950.
- [149] LD Landau. Ld landau, j. phys.(ussr) 5, 71 (1941). *J. Phys.(USSR)*, 5:71, 1941.
- [150] V Peshkov. Vp peshkov, j. phys. ussr 8, 131 (1944). *J. Phys. USSR*, 8:131, 1944.
- [151] CT Lane, Henry A Fairbank, and William M Fairbank. Second sound in liquid helium ii. *Physical Review*, 71(9):600, 1947.
- [152] V Peshkov. Report of the cambridge low temperature conference. 1947.
- [153] JC Ward and J Wilks. The velocity of second sound in liquid helium near the absolute zero. *The London, Edinburgh, and Dublin Philosophical Magazine and Journal of Science*, 42(326):314–316, 1951.
- [154] Clinton Craig Ackerman, B Bertman, Hi A Fairbank, and RA Guyer. Second sound in solid helium. *Physical Review Letters*, 16(18):789, 1966.
- [155] CC Ackerman and WC Overton Jr. Second sound in solid helium-3. *Physical Review Letters*, 22(15):764, 1969.
- [156] Howard E Jackson, Charles T Walker, and Thomas F McNelly. Second sound in naf. *Physical Review Letters*, 25(1):26, 1970.
- [157] TF McNelly. *Second Sound and Anharmonic Processes in Isotopically Pure Alkali-Halides*. 1974. PhD thesis, Ph. D. Thesis, Cornell University.
- [158] V Narayananamurti and RC Dynes. Observation of second sound in bismuth. *Physical Review Letters*, 28(22):1461, 1972.
- [159] RA Guyer and JA Krumhansl. Dispersion relation for second sound in solids. *Physical Review*, 133(5A):A1411, 1964.
- [160] Robert J Hardy. Phonon boltzmann equation and second sound in solids. *Physical Review B*, 2(4):1193, 1970.
- [161] W Götze and KH Michel. Two-fluid transport equations for lattices. *Physical Review*, 157(3):738, 1967.

- [162] JA Sussman. Ja sussmann and a. thellung, proc. phys. soc. london 81, 1122 (1963). In *Proc. Phys. Soc.(London)*, volume 81, page 1122, 1963.
- [163] RN Gurzhi. Thermal conductivity of dielectrics and ferrodielectrics at low temperatures. *SOVIET PHYSICS JETP*, 19(2), 1964.
- [164] RA Guyer and JA Krumhansl. Thermal conductivity, second sound, and phonon hydrodynamic phenomena in nonmetallic crystals. *Physical Review*, 148(2):778, 1966.
- [165] LP Mezhov-Deglin. Lp mezhov-deglin, zh. eksperim. i teor. fiz., 49, 66 (1965). *Zh. Eksperim. i Teor. Fiz.*, 49:66, 1965.
- [166] Valentina Martelli, Julio Larrea Jiménez, Mucio Continentino, Elisa Baggio-Saitovitch, and Kamran Behnia. Thermal transport and phonon hydrodynamics in strontium titanate. *Physical review letters*, 120(12):125901, 2018.
- [167] Yo Machida, Alaska Subedi, Kazuto Akiba, Atsushi Miyake, Masashi Tokunaga, Yuichi Akahama, Koichi Izawa, and Kamran Behnia. Observation of poiseuille flow of phonons in black phosphorus. *arXiv preprint arXiv:1802.05867*, 2018.
- [168] Eric Pop, Vikas Varshney, and Ajit K Roy. Thermal properties of graphene: Fundamentals and applications. *MRS bulletin*, 37(12):1273–1281, 2012.
- [169] Cho Yen Ho, Reginald W Powell, and Peter E Liley. Thermal conductivity of the elements. *Journal of Physical and Chemical Reference Data*, 1(2):279–421, 1972.
- [170] EW Prohofsky and JA Krumhansl. Second-sound propagation in dielectric solids. *Physical Review*, 133(5A):A1403, 1964.
- [171] Man-Yu Shang and Jing-Tao Lü. Nonlocal hydrodynamic phonon transport in two-dimensional materials. *arXiv preprint arXiv:1803.08372*, 2018.
- [172] Yuan Dong, Bing-Yang Cao, and Zeng-Yuan Guo. Generalized heat conduction laws based on thermomass theory and phonon hydrodynamics. *Journal of Applied Physics*, 110(6):063504, 2011.
- [173] Zhiwei Ding, Jiawei Zhou, Bai Song, Vazrik Chiloyan, Mingda Li, Te-Huan Liu, and Gang Chen. Phonon hydrodynamic heat conduction and knudsen minimum in graphite. *Nano letters*, 2017.
- [174] Laurent Chaput. Direct solution to the linearized phonon boltzmann equation. *Physical review letters*, 110(26):265506, 2013.
- [175] Philip C Kwok and Paul C Martin. Unified approach to interacting phonon problems. *Physical Review*, 142(2):495, 1966.

- [176] Alejandro Vega-Flick, Ryan A Duncan, Jeffrey K Eliason, John Cuffe, Jeremy A Johnson, J-PM Peraud, Lingping Zeng, Zhengmao Lu, Alexei A Maznev, Evelyn N Wang, et al. Thermal transport in suspended silicon membranes measured by laser-induced transient gratings. *AIP Advances*, 6(12):121903, 2016.
- [177] DKL Tsang, BJ Marsden, SL Fok, and G Hall. Graphite thermal expansion relationship for different temperature ranges. *Carbon*, 43(14):2902–2906, 2005.
- [178] Giuseppe Romano and Jeffrey C Grossman. Heat conduction in nanostructured materials predicted by phonon bulk mean free path distribution. *Journal of Heat Transfer*, 137(7):071302, 2015.
- [179] Jiecheng Zhang, Eli M Levenson-Falk, BJ Ramshaw, DA Bonn, Ruixing Liang, WN Hardy, Sean A Hartnoll, and Aharon Kapitulnik. Anomalous thermal diffusivity in underdoped  $yba_{2}cu_{3}o_{6+x}$ . *Proceedings of the National Academy of Sciences*, page 201703416, 2017.
- [180] Philip B Allen, Xiaoqun Du, Laszlo Mihaly, and Laszlo Forro. Thermal conductivity of insulating  $bi_2sr_2ycu_2o_8$  and superconducting  $bi_2sr_2cacu_2o_8$ : Failure of the phonon-gas picture. *Physical Review B*, 49(13):9073, 1994.
- [181] Bingbing Zhang, Jiali Zhao, Huixia Fu, Haidan Wen, Can Yu, Yujia Wang, Nianpeng Lu, Yuelin Li, Sheng Meng, Haizhong Guo, et al. Giant photoinduced lattice distortion in oxygen-vacancy ordered  $srcoo_2.5$  thin films. *arXiv preprint arXiv:1803.06780*, 2018.
- [182] Leonid Levitov and Gregory Falkovich. Electron viscosity, current vortices and negative nonlocal resistance in graphene. *Nature Physics*, 12(7):672, 2016.
- [183] Andrew Lucas and Sankar Das Sarma. Electronic hydrodynamics and the breakdown of the wiedemann-franz and mott laws in interacting metals. *arXiv preprint arXiv:1804.00665*, 2018.
- [184] Andrew Lucas and Sankar Das Sarma. Electronic sound modes and plasmons in hydrodynamic two-dimensional metals. *arXiv preprint arXiv:1801.01495*, 2018.
- [185] William George Unruh. Experimental black-hole evaporation? *Physical Review Letters*, 46(21):1351, 1981.
- [186] William G Unruh. Sonic analogue of black holes and the effects of high frequencies on black hole evaporation. *Physical Review D*, 51(6):2827, 1995.
- [187] Silke Weinfurtner, Edmund W Tedford, Matthew CJ Penrice, William G Unruh, and Gregory A Lawrence. Measurement of stimulated hawking emission in an analogue system. *Physical review letters*, 106(2):021302, 2011.
- [188] Jeff Steinhauer. Observation of self-amplifying hawking radiation in an analogue black-hole laser. *Nature Physics*, 10(11):864, 2014.